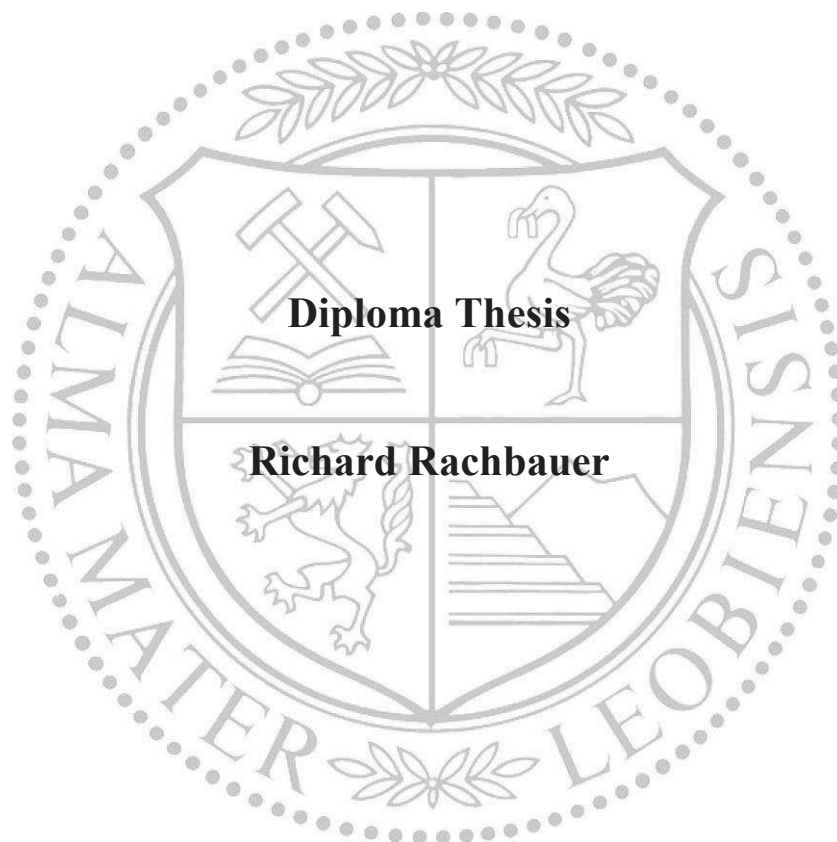University of Leoben

Comparative microstructural investigations of Ti-Al-N thin films alloyed with Y or Nb

Diploma Thesis

Richard Rachbauer

Leoben, 10th June 2008

Affidavit

I declare in lieu of oath, that I wrote this thesis and performed the associated research by myself, using only literature cited in this volume.

Leoben, 10th June 2008

Acknowledgements

First of all, I want to express my gratitude to Paul Mayrhofer for his scientific guidance and helpful hints. Moreover, I want to gratefully express my thanks for his confidence and his efforts to arrange a scientific stay within the INNOVATIAL-project in the Thin Films Physics Division at the Linköping University, Sweden.

In equal measure, I want to thank Martin Moser for his docile and efficient mentoring throughout the last months of his PhD-studies, where he managed to supervise and encourage me with my work, even within his limited time.

My sincerest gratitude is to Lars Hultman, head of the Thin Films Physics Division at the Linköping University, for enabling an unforgettable residence in his group and his support throughout the entire time in Sweden.

Special thanks to Martina Lattemann, my personal goddess of TEM, for introducing me to some secrets of the transmission electron microscope and her patience from early in the morning to late at night. Similarly, I want to thank Manfred Beckers for the interesting discussions and the constant attempt to make me believe, that thinking in reciprocal space would make things easier.

My personal appreciation is to my beloved girlfriend Astrid Wernisch, who endured endless discussions about the interesting world of thin films but still continued in encouragement and support in any task of daily matter. Furthermore, I would like to express my gratitude to Lukas Hädicke for his friendship and eternal discussions concerning the work-party-balance and the proper-beer-in-the-proper-moment-problem.

Especially, I want to thank my family and all friends, who spent a lot of time for talks and discussions and provided companionship for a beer or two. Finally, grateful thanks to all breweries, which supplied the fuel for my studies and supported numberless discussions.

Table of contents

Figure index

1 Introduction

Up to the 18th century human mobility and transportation were restricted to horses, coaches and ships. The introduction of the steam engine indicates the beginning of the industrial revolution, which permitted for the first time heavy load transportation and shipping. The limited efficiency of the steam devices was subsequently enhanced by the combustion engine, which fundamentally changed the meaning of the phrase "Life is motion".

Nowadays, global industry, economy and tourism strongly depend on efficient ways of mobility and transportation. The reduction of fuel consummation is considered as a cornerstone in future transportation, and goes along with cost reduction and the need for an environmentally harmless traffic. In times of constantly increasing numbers of passengers and transportation of goods, especially in aviation, the development of new technologies is necessary. Hence, to improve established concepts, with respect to the above given requirements two possibilities seem most promising for efficiency increase and pollution reduction: weight reduction of structural parts and higher combustion temperatures.

In aircraft turbines, components made of heavy Ni-base alloys can be replaced by Titanium-Aluminides. However their limited oxidation resistance at temperatures above 750 °C impedes a broad utilization.

$Ti_{1-x}Al_xN$-coatings are successfully applied for the protection of dies, molds or as wear and temperature resistant coatings in tooling applications [1]. Consequently, the $Ti_{1-x}Al_xN$-system was chosen as protective coating for Ti-Al alloys. $Ti_{1-x}Al_xN$-coatings can act as oxidation barrier for Ti-Al-components, or to outbalance the thermal mismatch of later to be applied thermal barrier coatings (TBC).

With this approach, the task of further reducing the exhaust emissions, combined with a higher efficiency factor, of engines and turbines, could be fulfilled. Further, the addition of a forth alloying element to $Ti_{1-x}Al_xN$ [2], gives rise to the possibility of further improving the oxidation resistance, thermal stability and mechanical properties.

Yttrium and niobium, with melting points of 1800 °C and 2750 °C, respectively, represent two transition metals, slightly larger in atomic size than titanium, which form stable oxides at elevated temperatures. Thus, both elements are established for TiAl-based alloys [1, 3] to improve their oxidation behaviour. Yttrium is known to block outward cation transport at scale grain boundaries and improves scale adhesion in TiAl-base alloys, whereas Nb acts as a low-diffusivity element in Titanium-Aluminides and impedes transport processes at the oxide interfaces.

As a first step, in this thesis, the structure, evolution and thermal stability of $Ti_{0.42}Al_{0.58}N$, and the influence of the alloying elements Y and Nb, are investigated. The amount of Y and Nb in the powder metallurgically prepared targets were 2, 4 and 8 at.%, respectively. Using state of the art investigation methods, such as x-ray diffraction, transmission electron microscopy, nanoindentation and thermal analyses, the impact of the alloying species and their amount on microstructure, mechanical properties and thermal stability of the respective thin films is evaluated.

2 Deposition of coatings

2.1 General

In thin film technology a wide range of processing routes exist, which allow the modification of surfaces and the development of coatings, tailor made for their respective applications. Depending on the process utilized, coatings or surface modifications are achieved which provide enhanced wear or thermal resistance, or increase optic or magnetic properties for the subjacent material. In general one can differ between several routes of producing the coating or overlay [4]:

- ✓ Mechanical: The protective layer is applied by cladding, bonding or explosive cladding.
- ✓ Thermal: Applies a protective layer by remelting the surface region, sintering, build-up welding or hot-dipping.
- ✓ Chemical: Surface treatment using currentless phosphating-, chromating-, or nickel-plating processes.
- ✓ Thermo-mechanical: Application of a coating by plasma-, flame-, or explosion gunning.
- ✓ Electro-chemical: Cathodic or anodic deposition through electrolyses (e.g. nickel, chromium or zinc).
- ✓ Vapour deposition:
  - ○ CVD (chemical vapour deposition): Chemical reactions, activated by e.g. heat, plasma or ultraviolet light, lead to thin coatings on the component [5].
  - ○ PVD (physical vapour deposition): Physical reactions, e.g. thermal evaporation/sublimation, sputtering or arc-sputtering, create vapour particles which deposit on the tool component [6].

In comparison to CVD or electro-chemical processes, PVD offers the advantage of improved environmental compatibility, by avoiding hazardous gases or electrolytes, in combination with an extremely versatile process which allows the deposition of metals, ceramics or organic materials [7].

PVD processes can be divided into two categories:

✓ Thermal evaporation/sublimation: Through energy input by resistance heating, induction, electron beam, arc or laser, target atoms are evaporated in a vacuum chamber and condense from the vapor phase onto a substrate.

✓ Sputtering: In sputtering, atoms or atomic clusters are ejected from the target by elastic collisions with gas ions, generated in a plasma and accelerated to the target. Sputtering is used as deposition method in this thesis and is described in more detail in section 2.3.

The above mentioned ways of freeing atoms from a target surface represent basic kinds of physical vapor deposition. Commonly a vacuum is established to enlarge the mean free length between the collision of atoms before they reach the substrate [8, 9].

Moreover, by ion bombardment a better film bonding to the substrate and improved microstructure is possible. This means that the sputtered or evaporated, particles, which can be atoms or ions, are accelerated by an external electric field and hit the surface of the substrate with a higher energy. While atoms are almost not affected, the external field can have a positive influence on the growth and morphology of the film, in case of ions. In addition, ion etching means that ions are generated from the work gas and accelerated onto the substrate through a high voltage between substrate and cathode. This technique alters the surfaces of the substrate and can be used to remove e.g. oxides by sputtering [10].

2.2 Plasma

Generally a plasma is regarded as a quasineutral gas, consisting of electrons, ions, atoms and molecules, which exhibit a collective behavior and can be influenced by electric and magnetic fields. Due to its behavior and the distinction from solid, liquid, or non-ionized gas, plasmas are treated as a fourth state of matter [11, 12].

2.2.1 Fundamentals of plasma

To create a plasma of a pure substance, required temperatures are ranging from 4000 to 20000 K. Though, low-pressure conditions for plasma creation at room temperature exist, which are far away from thermal equilibrium. For equilibrium conditions the concentration of electrons (n_e) and ions (n_i) per m^3 (n is the plasma density) is assumed to be equal. Thus the electric neutrality of a plasma is explained by the following relation: $n_e = n_i = n$. Moreover we can define the fraction of ionization $f_i = n_e/(n_e+n_0)$, with n_0 as the neutral gas species.

Usually the plasma temperature (T_{pl}) is assumed as one value. However, the temperatures of electrons (T_e), ions (T_i) and non-charged particles (T_n) can differ strongly. They possess different kinetic energies, due to their unequal masses and modes of motion. Therefore, only in thermodynamic equilibrium they are about the same and $T_e = T_i = T_{pl}$ [6, 9].

2.2.2 Characteristic values of plasmas

✓   Debye length (λ_D):

A characteristic scale length which describes the shielding of Coulomb potentials of individually charged particles is called the Debye length (λ_D). Within λ_D, the potential of an ion decreases to 1/e of the original value, and is given by:

$$\lambda_D = \sqrt{\frac{\varepsilon_0 * k_B * T_e}{n_e * e^2}}$$

(2.1)

where, ε_0 is the vacuum permittivity, e the electron charge, T_e the electron temperature, n_e the concentration of electrons and k_B the Boltzmann constant [13].

✓   Plasma frequency:

The response of a plasma to the displacement of electrons from ions is termed plasma frequency. As soon as an electrical field, which causes the displacement, is removed, the electrons are pulled back towards the ions. Due to the high velocity of the electrons they are trapped in an oscillation about the ions with a certain frequency – the plasma frequency (ω_p) [14].

$$\omega_p = \sqrt{\frac{n_e * e^2}{\varepsilon_0 * m_e}}$$

(2.2)

As the mass of an electron m_e is small compared to the mass of ions, frequencies in the range of ~0.9 GHz can be expected, considering a plasma density n_e of 10^{13} m^{-3} [14]. Consequently the velocity of electrons (c_e) is described as:

$$\lambda_D * \omega_p = \sqrt{\frac{\varepsilon_0 * k_B * T_e}{n_e * e^2}} * \sqrt{\frac{n_e * e^2}{\varepsilon_0 * m_e}} = \sqrt{\frac{k_B * T_e}{m_e}} \cong c_e \tag{2.3}$$

✓   Plasma- and Floating-potential:

Within the bulk of a plasma the differences between velocities, densities and temperatures of particles are insignificant. Since electrons have less mass, but much higher velocities compared to ions or neutrals, the charge flux J_e of electrons onto an initially non-charged substrate is higher than the flux of ions J_i . Therefore, the substrate surfaces rapidly charge negative and have a negative potential with respect to the plasma. This leads to a retarding sheath, which repels electrons from and attracts ions to the surrounding of the substrate surface, as shown in Figure 2.1. Consequently, a balance of fluxes is reached at the border of the sheath. Nevertheless the average plasma is still electrically field free [13].

The potential of the isolated substrate is defined as floating potential V_f, the potential in the plasma is called plasma potential V_p. Assuming a plasma, contained by insulating walls, with a zero steady-state net flux, the wall potential and floating potential are related terms. Thus V_f describes the repelling force and V_p the attracting force on electrons, whereas V_f is more negative than V_p [14].

The potential difference of ΔV_p , is described as: $\Delta V_p = V_p$ - V_f. It gives a relation to the force of attraction for ions towards the substrate. The floating potential V_f , measured from ground, is negative with respect to the plasma to retard electrons.
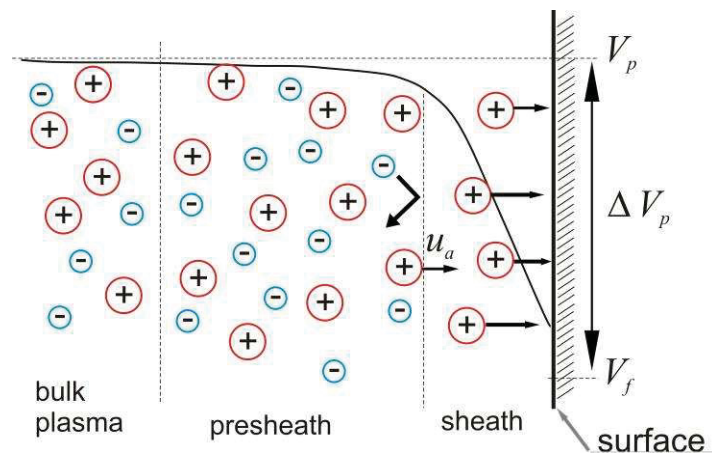
Figure 2.1: Typical charge distribution and voltage profile near a surface, redrawn from [14].

2.2.3 Plasma reactions

Collision processes within the plasma lead to reactions of electrons, ions and neutrals and influence the total plasma behavior.

Particles collide due to thermal fluctuation in two possible ways. In elastic collisions, direction and velocity of the colliding particles change, resulting in an exchange of kinetic energy. In contrast, the inelastic collision is defined by a kinetic energy exchange between particles, which is accompanied by a change in potential energy. Therefore, a change of impulse of particle one, respectively two occurs and the absorbed energy can be used for e.g. ionization, excitation, recombination or dissociation processes. The diversity of reactions is a result of the different reaction partners, such as electrons, ions, atoms and gas molecules [12].

In direct current (DC) magnetron sputtering systems all of the above mentioned processes occur. These reactions can be controlled by external power supply (electric-, magnetic fields), working pressure and temperature.

2.2.4 Glow discharge

Although there exist several ways to generate a cold plasma, like the application of radio frequencies (RF) or microwaves (MW), we consider the case of direct current (DC) [11], as used in this work.

At low gas pressures an external electric field above a threshold value has to be applied, to create an electrically conducting medium, a plasma, out of an insulating gas. The main reaction therein is the ionization of gas atoms, caused by free electrons near the anode target. Due to the electric field the electrons are accelerated towards the anode and collide with more gas particles. As a consequence ions are also accelerated by this field. At low power the number of charge carriers is small. In a voltage to current density plot, as shown in Figure 2.2, this region is called Townsend discharge. Increasing the power in that region will not influence the voltage due to the impedance of the power supply. Above a critical current density, the ionization reaction is avalanche-like and the plasma is self-sustaining. The consequence is a voltage drop and reaching of the normal glow domain. At this stage the ion bombardment is concentrated on edges and irregularities of the cathode (target). With increasing power the

bombardment spreads over the entire cathode surface. This marks the transition region to abnormal discharge, which signifies the operative domain for sputtering (see Figure 2.2). Further increasing the power results in target heating and consequently to thermally emitted electrons and low-voltage arcs, where the region of cathodic arc evaporation starts [12].
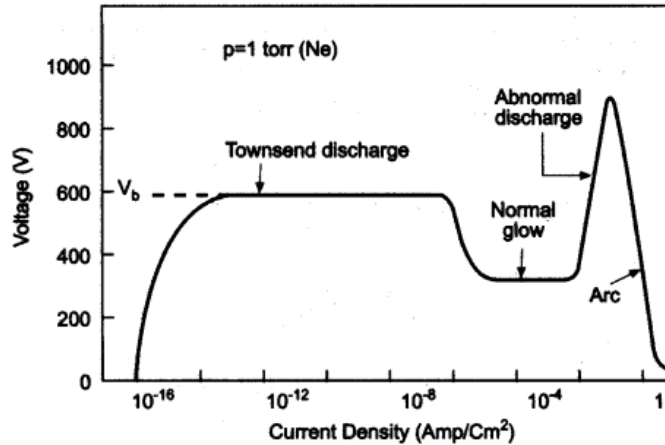
Figure 2.2: Voltage versus current density trace of a discharge processes [15].

2.3   Sputtering

In general, sputtering is a process of ejecting particles from a solid source, called target, by incident ions of a working gas, e.g. Ar^+. The latter are accelerated to the target by an electrical field, generated by a direct current (DC), alternating current (AC) or radio-frequency (RF) modulating source [5].

2.3.1   DC-sputtering

DC-sputtering forms the most prominent coating process in PVD-thin film technology. Usually the electric field is applied between cathode (target) and the substrate containing anode, facing each other in a distance of a few centimeters. In general, it is possible to sputter single metallic, or compound and ceramic targets. When only particles from the target are used for coating formation, the process is called non-reactive. A wide range of compositions can however be synthesized by introducing a reactive gas, e.g. nitrogen, oxygen or synthetic air, to the coating formation process. Accordingly, this is termed reactive sputtering [14].

A schematic of a DC sputtering system is presented in Figure 2.3, the shown reactions are described in chapter 2.2.3.
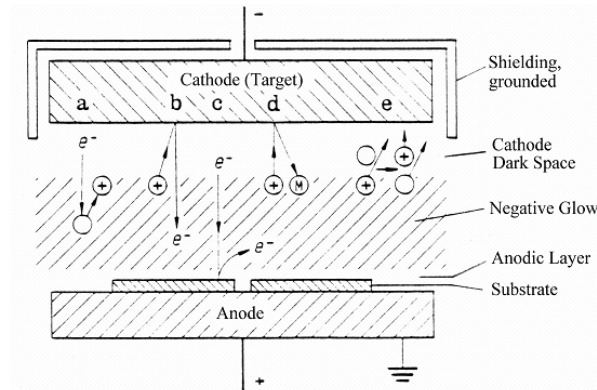
Figure 2.3: Possible particle interactions during sputtering [9]. (a) Ionisation by electron impact, (b) ion induced electron emission from cathode, (c) electron induced emission of secondary electrons from the anode, (d) sputtering caused by ion impact, (e) charge transition process.

On the first view, the most influential parameter within a sputtering process is the pressure. At low pressures, the mean free electron length between two collisions is large, ions are produced far away from the target and easily lost to the walls. The cathode sheath is relatively wide, thus electrons are likely to be caught by the anode and not equally replaced by secondary-electron emission from impacting ions. Therefore, a self-sustaining plasma is not reached easily. With increasing pressure the ionization rate becomes higher due to the decreasing mean free electron path. However, high pressure levels lead to a reduced deposition efficiency, as a result of the increased number of collisionally scattered atoms [12].

Applying a negative potential to the anode (substrate), the bias, commonly between -50 and -300 V, can also be. A bias influences flux and energy of deposited particles, and therefore affects strongly the coating-growth process, -adhesion and -density.

2.3.2 Magnetron sputtering

The magnetron component of a sputtering process is achieved by permanent magnets on the backside of the target. Owing to the magnetic field lines, which leave and reenter the target surface, the electrons are trapped on cycloidal paths. Therefore the plasma activity is most intense in this region, resulting in a circular target erosion zone, as presented in Figure 2.4. Due to this plasma confinement the sputter rate increases up to

factor ten, since only charged particles and not the ejected neutral atoms are influenced by the magnetic field [9].

Depending on the configuration and strength of the centric and outer magnets, two magnetron systems are distinguished. In the balanced systems all magnetic field lines are closed between inner and outer poles trapping the charged particles near the substrate.

In contrast the magnets of inner and outer poles of the unbalanced magnetron (UBM) system have different strengths. Therefore they create magnetic field lines which partly involve the substrate. The UBM systems allow also a higher ionization rate near the substrate, and can thus improve the deposition behavior of films [16, 17]. The principle of UBM sputtering is shown in Figure 2.4.
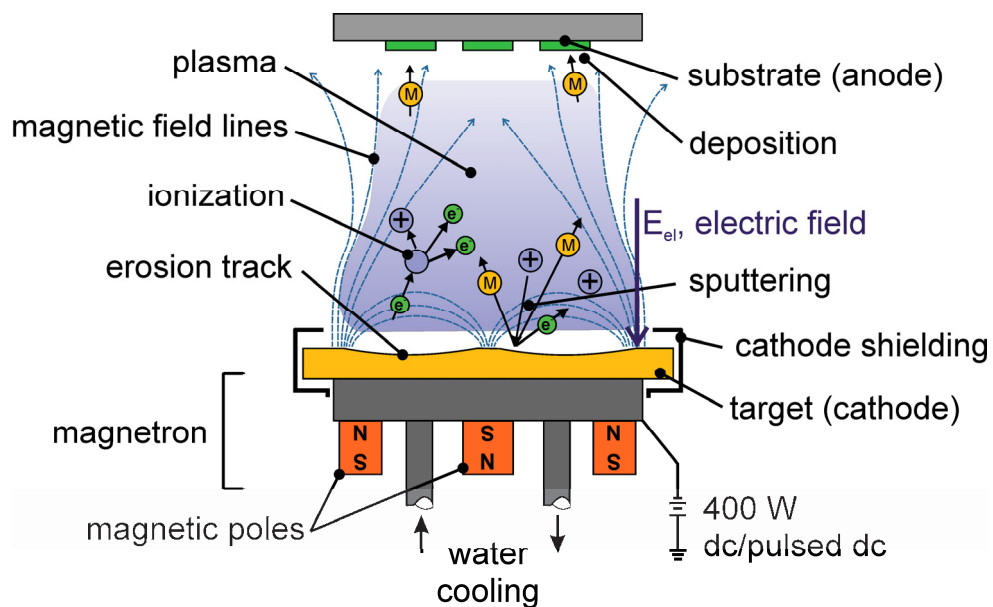
Figure 2.4: Unbalanced magnetron (UBM) configuration [18, 19].

2.4 Morphology of thin films

2.4.1 Nucleation and growth

Physical, chemical and mechanical behavior of thin films strongly depend on the deposition process and the used parameters. The film synthesis takes place far away from thermodynamic equilibrium. Depending on the energy of the impinging particles on the substrate, they are adsorbed or immediately reevaporated. In case of adsorption there exist several reactions, which can occur before the atoms combine to clusters and build nuclei, as illustrated in Figure 2.5. The further arrival of deposition atoms leads to an enlargement of the nuclei and therefore the base for a coherent film. This process is termed growth.
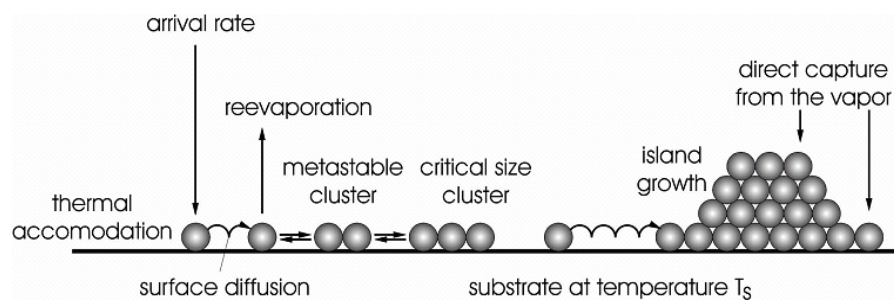
Figure 2.5: Schematic representation of processes leading to three-dimensional nucleation and film growth [18, 20].

The following steps of nucleation and growth shall give a brief overview of film evolution [20]:

a) Formation of adsorbed monomers (deposited atoms or ions).

b) Formation of subcritical nuclei of various sizes.

c) Formation of critically sized nuclei (nucleation step).

d) Growth of these nuclei to supercritical dimensions with the resulting depletion of monomers in the capture zone around them. Concurrently, there will be nucleation of critical clusters in areas, which are not depleted of monomers.

e) Clusters touch and coalesce to form a new island, occupying an area smaller than the sum of the original two, thus exposing fresh substrate surface.

f) Monomers adsorb on these freshly exposed areas, and secondary nucleation occurs.

g) Large islands grow together, leaving channels or holes of exposed substrate.

h) The channels or holes fill via secondary nucleation to give a continuous film.

Depending on the affinity of the film to itself and the substrate, basically three modes of nucleation are defined, the "island" mode (Volmer-Weber), "layer-by-layer" mode (Frank-Van der Merwe), and a mixed mode of the former two, called "Stranski-Krastanov". They are respectively shown in the schematic of Figure 2.6(a-c). Island growth occurs when deposited atoms are stronger bound to each other than to the substrate. Therefore they form 3D-clusters, Figure 2.6(a), which are called islands. Layer-by-layer growth implies that at first the adsorbed atoms create a complete monolayer, before they begin to build up a second layer, Figure 2.6(b). This mode is important for the epitaxial growth of single-crystals like silicon. The last but rather common growth mode, is the layer plus island or Stranski-Krastanov-mode. It resembles an intermediate combination of the first two. At the beginning monolayers form, before the island mode becomes predominant, Figure 2.6(a-c) [12].
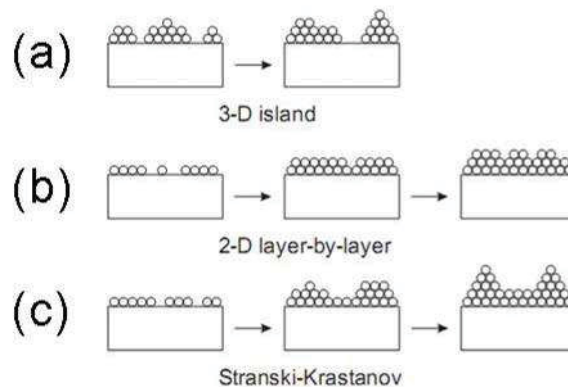
Figure 2.6: Nucleation modes [12].

The next step in film evolution and growth is shown in Figure 2.7. When the initial clusters, presented in Figure 2.7(a,b), get in contact with each other, a reaction, termed as coalescence, occurs, Figure 2.7(c). In this stage nucleation kinetics are fairly affected by the adatom binding energy, temperature, crystal structure of the substrate, lattice defects, surface steps and contamination. The growing together of two nuclei is

governed by strong driving forces, like the reduction of surface energy, and achieved by surface diffusion and grain boundary motion. Coarsening of the grains, Ostwald ripening, results as the island with the lower energy per atom consumes the others, Figure 2.7(d). The development of a continuous structure is therefore enabled, Figure 2.7(e) [17].
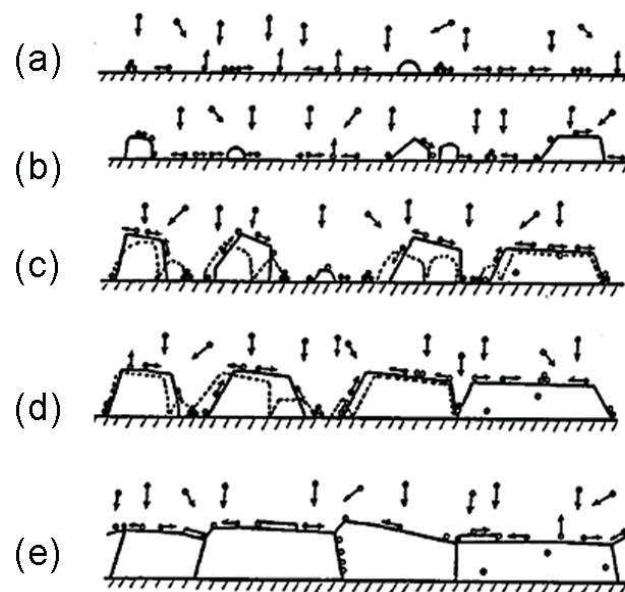
Figure 2.7: Schematic diagram illustrating fundamental growth processes [17]. Controlling microstructural evolution from top to bottom: (a) nucleation, (b) island growth, (c) impingement and coalescence of islands, (d) grain coarsening, formation of polycrystalline islands and channels, (e) development of a continuous structure and film growth.

2.4.2 Structure zone models

As shown above, impinging atoms have several possibilities to arrange and undergo structural changes during growth. In each case the arriving particles diffuse over the substrate surface before they are trapped in low-energy lattice sites. To correlate the resulting microstructure of thin films with deposition parameters and the predominant processes for each case, structure zone models (SZM) were developed [5]. In dependence of the adsorption processes *shadowing*, *surface diffusion*, *bulk diffusion*, and *desorption*, the lowest-energy position of atoms may be the result of a long elastic journey. Shadowing explains the geometric interaction of the arriving deposition atoms and the surface quality of the substrate. The other processes are based on material

constants, like the energies for diffusion and sublimation, which can be assumed as proportional to the melting point T_m [12]. Movchan and Demchisin introduced the first SZM, based on investigations of thin film microstructure. They proposed three main structure zones, depending on the ratio of T_m of the deposited material and the deposition- or substrate temperature T_s [21]. Thus, T_s/T_m or the homologous temperature, signifies the basic variable of any SZM. Thornton added the inert gas pressure in his model as a second axis and defined one additional zone (T-zone). Therefore the decreasing energy of the impinging atoms is related to the increasing working gas pressure due to a higher number of collisions [22].

Detailed explanations for the zones are given in references [21, 22] but in short they are characterized as follows:

- ✓ Zone 1 is the result of shadowing effects and appears in amorphous, as well as in polycrystalline films. Due to limited surface diffusion they exhibit porous, tapered crystallites, which are poorly defined but include a high dislocation density. Voids arise between the dome shaped crystals. Increasing argon pressure extends zone 1, while higher T_s/T_m leads to larger crystals.
- ✓ Zone T has a dense columnar structure with fibrous grains but no voids between the domains. This is a result of the increased homologous temperature. Zone T is regarded as the transition regime from zone 1 to zone 2.
- ✓ Zone 2 exhibits coarser columnar grains, which are dense and formed by restructuring and ripening through grain boundary migration. Surface diffusion is assumed as the predominant process at these elevated temperatures.
- ✓ Zone 3 consists of large equiaxed grains and shows a smooth surface. Grown at high enough temperatures, that even bulk diffusion is possible, a dense recrystallized structure is formed.

Figure 2.8 shows an exploded view of structures grown through *shadowing*, *surface diffusion*, *bulk diffusion* and *desorption* and combines them in the SZM of Thornton into the bottom of the picture.
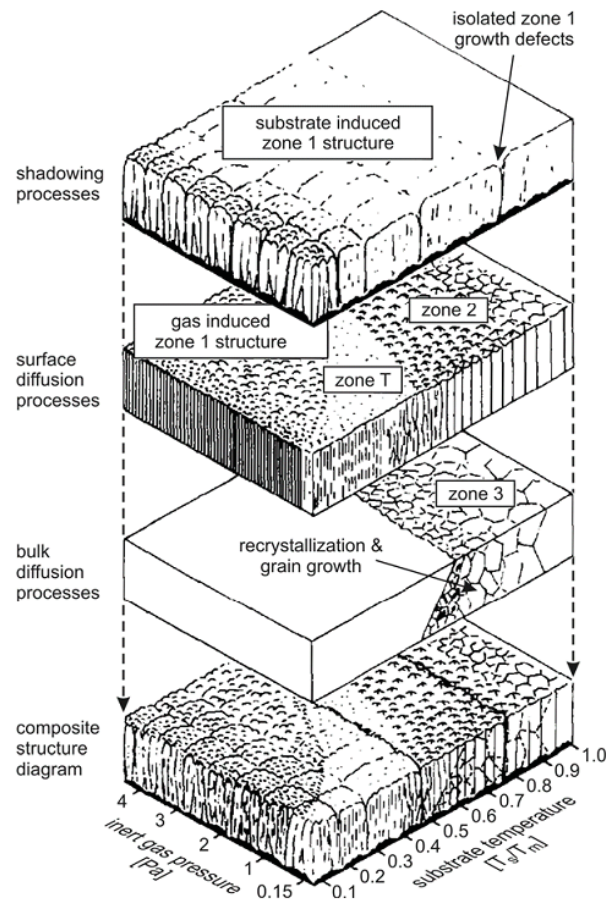
Figure 2.8: Exploded view of the physical processes underlying the Thornton structure zone model (SZM) consisting of the zones 1, T, 2, and 3 [22].

Messier et al. investigated additionally the influence of bias voltage, as presented in Figure 2.9. At higher voltages the Zone T is extended to lower homologous temperatures, because of the increasing deposition particle energy [23].
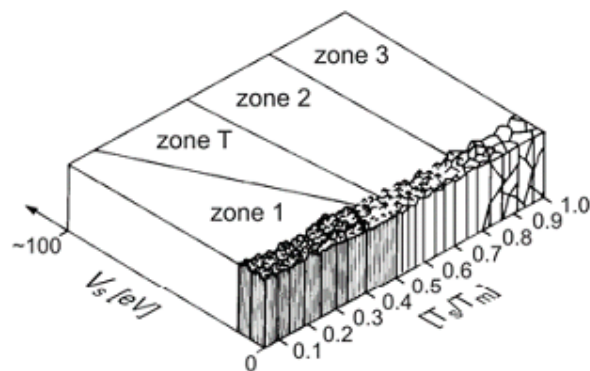
Figure 2.9: SZM according to Messier et al. [23]

Investigations on the morphological influence of impurities were undertaken by Barna and Adamik, as shown in Figure 2.10. For pure deposits the improved SZM resembles an ideal SZM. Increasing content of impurities leads to diminishing zone 2 and zone T. The foreign particles result in decreasing surface mobility and low diffusion processes, respectively. Within the bulk, impurities may lead to a change of the grain boundary mobility at elevated temperatures. Moreover, it is even possible that compounds with the deposited material are built at high impurity levels. Thus, zone 1 shades into zone 3, [24].
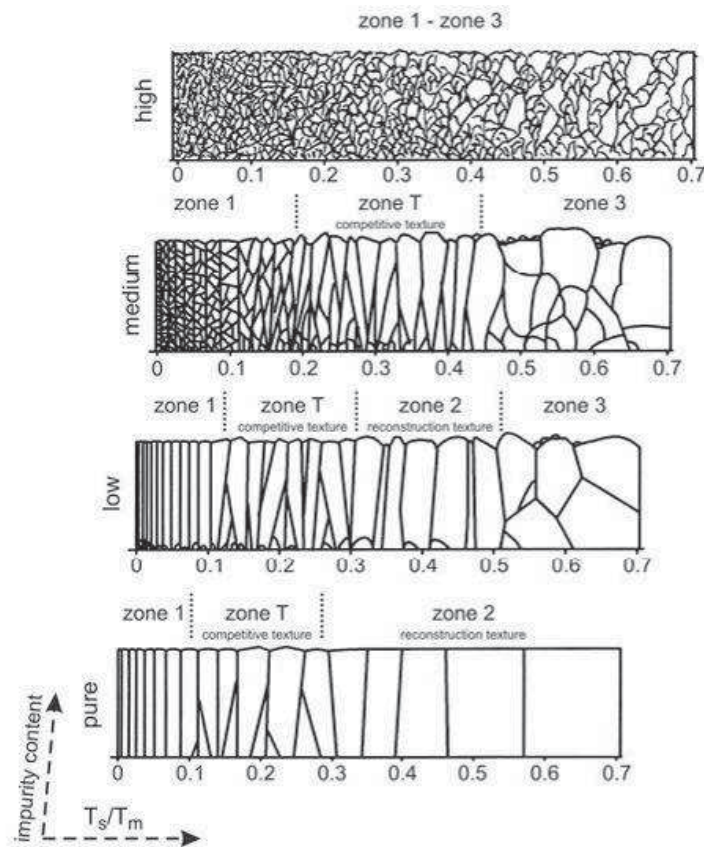
Figure 2.10: Ideal (bottom) and real SZMs with increasing impurity content [24].

In addition to the discussion about SZM`s it should be marked, how various conditions can influence the growth of films. The structure of zone 1 and zone T mainly corresponds to shadowing effects, while zone 2 and zone 3 are mainly the consequence of surface and bulk diffusion, respectively. Figure 2.11 denotes several extreme cases of adatom surface diffusion. In every case, coatings grow from discrete initial nuclei by a sequence of morphological changes in which those nuclei with favorable growth

properties and deposition conditions survive. In case of zero surface diffusion and a unity condensation coefficient (every deposited atom adheres where it lands), Figure 2.11(a), the initial nuclei are spherical since there is no crystal surface discrimination. Affected by normal flux, with some side scattering, the structure is grown in a zone T shape with the orientation of the initial nuclei preserved. Figure 2.11(b) shows the case of zero surface diffusion on crystal surfaces with different surface energies and condensation coefficients. At normal flux, the initial nuclei are assumed to be faceted. The differing condensation rates depend on the orientation of the nuclei and determine the speed of growth. Therefore, the low energy faces grow faster and lead to an open structure with rough surface, corresponding to zone 1. In case of infinite surface diffusion the dependence on the condensation coefficient is compensated at elevated temperatures. Therefore a dense columnar zone 2 structure is formed, where the growth rate is assumed to be the same on all planes, Figure 2.11(c). The periodic nucleation on the surface of the growing crystals signifies the case shown in Figure 2.11(d). A dense but still columnar structure is achieved by infinite surface diffusion [22].
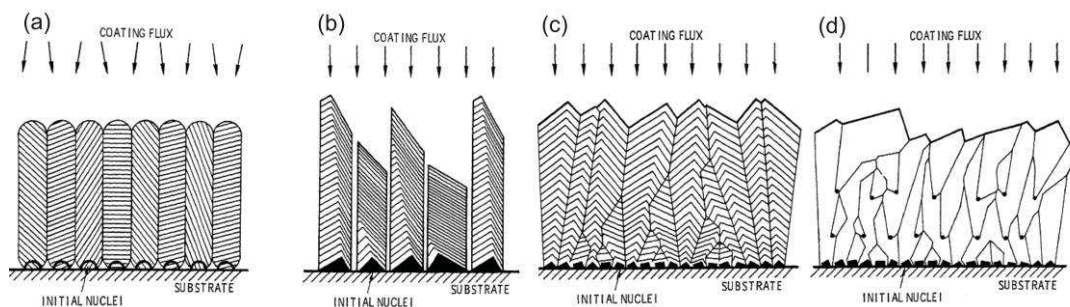
Figure 2.11: Structure development for several cases of adatom surface diffusion [22]. (a) Zero surface diffusion, equal condensation coefficient, (b) zero surface diffusion, condensation coefficient depend on crystallographic surface, (c) infinite surface diffusion and (d) infinite surface diffusion with periodic nucleation.

3 Coating system

With the beginning of the industrial use of hard protective coatings for cutting and forming applications, TiN and TiC films were found to enhance the tool life up to five times. Despite of its chemical stability, low friction coefficients and high hardness, the oxidation stability of TiN in ambient air is limited to 550 °C [25]. However, the demand of higher cutting speeds and enhanced thermal stability lead to a wide range of still ongoing investigations in improving this well known coating systems. Attempts in addition of Al, B, Cr, C, Si or Zr to the binary TiN system expand the property- and application range [25-29].

Incorporating Al into TiN, reached the required properties and can be regarded as the most popular improved TiN-system. The system $Ti_{1-x}Al_xN$ is protected by a dense Al_2O_3-layer up to about 950 °C. Moreover the coating provides a lower friction coefficient, higher hardness and stability at elevated temperatures and is less thermally conductive [30].

3.1 Microstructure

The system TiN, which is characterised by a strong covalent-metallic bonding and therefore a high melting point of about 2950 °C, obtains a face centered cubic (fcc) NaCl type structure, as presented in Figure 3.1(a). In contrast, the thermodynamic stable configuration of mainly covalent bonded AlN is a hexagonal close packed (hcp) ZnS-wurtzite-type structure, Figure 3.1(b), which is thermally stable up to about 2800 °C [30].
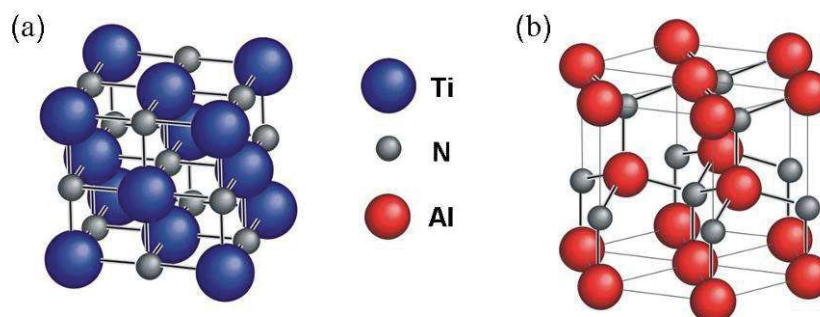
Figure 3.1: (a) Fcc-lattice of TiN and (b) hcp-wurtzite-lattice of AlN.

The solubility of AlN in TiN is extremely limited even at higher temperatures. At 2500 °C it is not more than approximately 5 at.% [25, 28, 31]. The TiN-AlN phase diagram given in Figure 3.2(b), is taken as a quasibinary phase diagram from the ternary system Ti-Al-N in Figure 3.2(a) and shows an eutectic temperature, which can be regarded as the boundary line for the two-phase region, consisting of the metallic hard material fcc-TiN and the covalent hard material hcp-AlN. Therefore any existence of a stable single phase field at elevated temperatures seems not expedient [2].
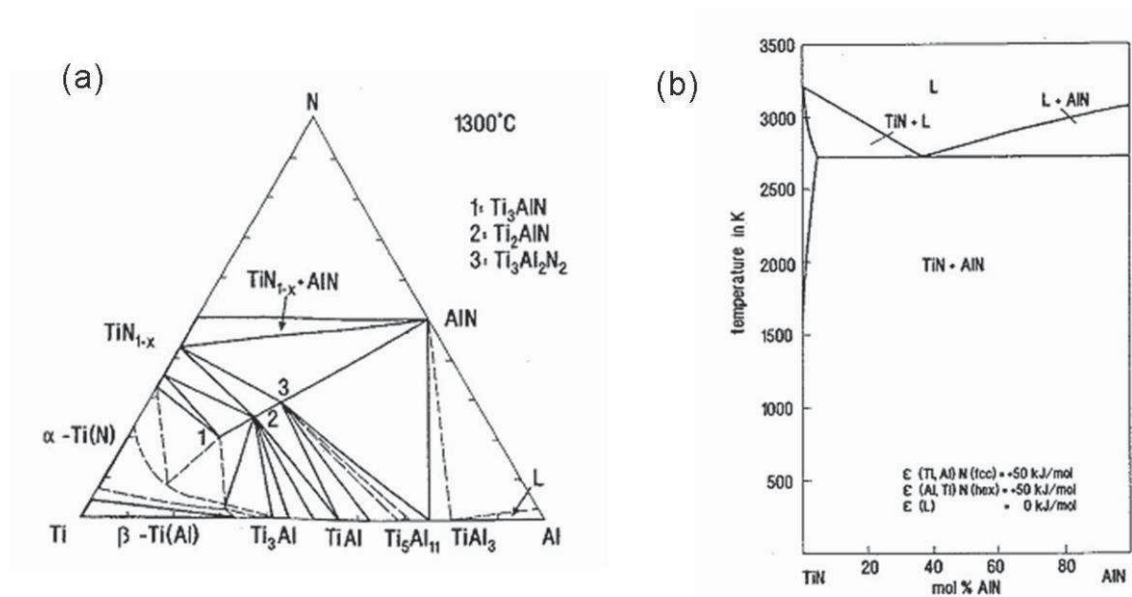
Figure 3.2: (a) Ternary phase diagram of Ti-Al-N and (b) quasi-binary TiN-AlN phase diagram [2].

However, if the $Ti_{1-x}Al_xN$ coatings are prepared by plasma-assisted vacuum deposition at relatively low temperature of about ≤350-550 °C, a supersaturated metastable solid solution can be obtained [28, 31, 32].

The incorporation of Al-atoms into TiN takes place by substitution of Ti-atoms on fcc-lattice positions. The cubic NaCl structure of $Ti_{1-x}Al_xN$ is maintained with increasing Al-content up to a critical composition of x ~0.7, whereas at higher Al-contents the hexagonal ZnS structure is formed. Between the two single phase regimes, a transition region can be found, as shown in Figure 3.3. The maximum solubility for Al under maintenance of cubic structure, varies with different deposition techniques and parameters [2, 25, 28, 33-35].
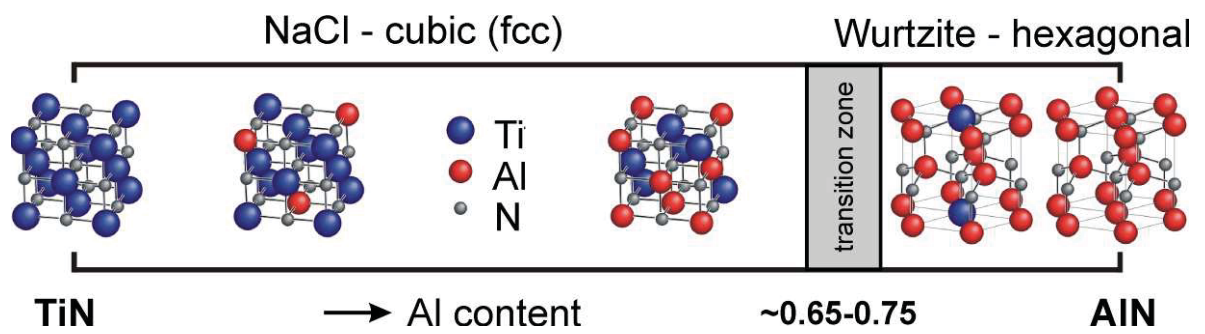
Figure 3.3: Structural changes with increasing Al-content [19, 36].

The observed shrinkage of the cubic lattice parameter of $Ti_{1-x}Al_xN$, from ~4.23 Å for pure TiN to ~4.17 Å at x = 0.6 by Al incorporation, given in Figure 3.4 corresponds to other findings reported in [30, 33, 37, 38], and was confirmed by thermodynamic and ab-initio modeling [39-41]. For the hcp-$Ti_{1-x}Al_xN$, a decreasing a-axis but an enlarged c-axis was found [19].

3.2 Mechanical properties

$Ti_{1-x}Al_xN$ coatings provide a wide range of hardness and elastic modulus, mainly depending on the Al-content, as presented in Figure 3.4(b). The hardness of TiN is approximately 20 GPa (~2000 HV) and develops as a function of incorporated Al into TiN, as shown in Figure 3.4(a). The maximum hardness of $Ti_{1-x}Al_xN$ with 32 GPa (~3200 HV) emerges at about x=0.6, however it strongly depends on the deposition technique and its parameters. Therefore even superhard $Ti_{1-x}Al_xN$ coatings, with a hardness of 47 GPa (~4800 HV) were reported [32]. As a result of the increasing hexagonal phase fraction at higher Al-contents, above the metastable solubility limit the hardness rapidly decreases to 14 GPa (~1400 HV) at x=0.9. The lower hardness of the hexagonal phase corresponds to the bonding characteristics and the much lower packing density [30, 33].
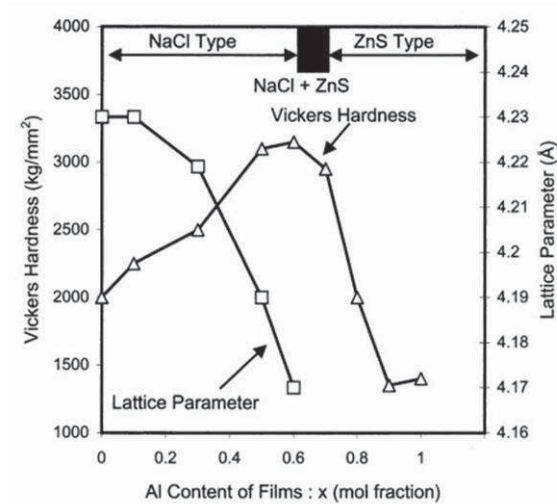
Figure 3.4: Hardness and lattice parameter of $Ti_{1-x}Al_xN$ coatings [30].

3.3 Thermal properties

Observations on fcc-$Ti_{1-x}Al_xN$ showed structural changes, involving the formerly discussed processes, as presented in Figure 3.5. Thermal activation until ~900 °C enables only recovery and therefore internal stress relaxation. Above 900 °C spinodal decomposition of fcc-$Ti_{1-x}Al_xN$ occurs into fcc-Ti(Al)N and fcc-AlN. The fcc-AlN is coherently precipitated in the fcc-$Ti_{1-x}Al_xN$ matrix. Further annealing leads to the separation into the equilibrium phases fcc-TiN and the formation of hcp-AlN [42].
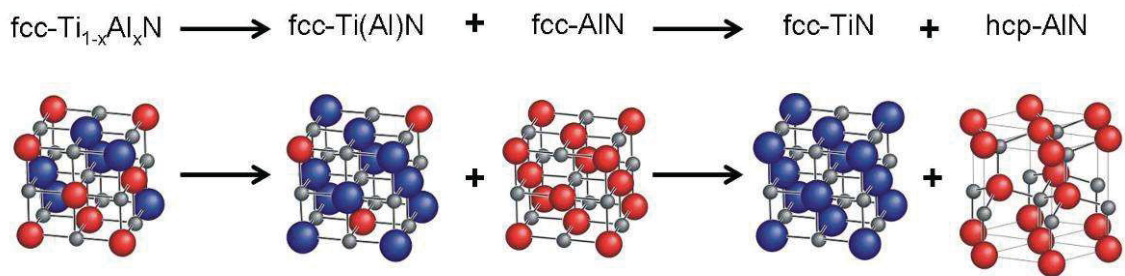
Figure 3.5: Structural changes of fcc-$Ti_{1-x}Al_xN$ with increasing temperature, modified from [36].

4 Thermally induced processes

During a PVD process, numerous point-, line-, planar- or volume-defects are induced by high-energy impacting particles [43], as well as due to the condensation from the vapour phase and therefore the high cooling rates. Vacancies and interstitial atoms are termed point defects, while dislocations are line defects. Stacking faults and twin boundaries are counted as planar defects, and voids or cavities are volume defects [44]. In general, this concentration of defects results in a high amount of internal energy stored and defines the film in the as-deposited state, as far from thermodynamic equilibrium. Moreover, a lot of interfacial boundaries form during the deposition process, or during exposure at elevated temperatures where metastable phases decompose to form nanoscale domains and precipitates, e.g. as in Ti-Al-N investigated in this work.

The application conditions for hard coatings, assuming e.g. metal machining, include strong thermal exposures besides the mechanical wear. A consequence of thermal influence is the rapid change of the defect density and restructuring, occurring in several possible pathways, as described in the following [18].

4.1 General

The atomic movement in solid materials is called diffusion. The basic constant to describe the velocity of diffusion is the diffusion coefficient, according to Fick´s law [45]. For regions with different compositions, the reaction-determining force is the reduction of the Gibbs free energy. For every diffusion process, an activation energy has to be provided, which is strongly dependent on temperature [46].

Diffusion is the elemental process for mass transport in solids, and influenced by the concentration gradient and mode of diffusion (surface, grain-boundary or bulk diffusion). It is governed by two atomistic mechanisms, interstitial and substitutional diffusion. Both processes occur faster with increasing temperature or enough energy is provided by lattice vibrations, resulting in the increasing diffusion coefficient and therefore a reduction of the activation energy term is reached. Thus, higher temperatures make way for diffusion modes, which require higher activation energies, e.g. grain-boundary and bulk diffusion. The processes, presented in Figure 4.1, are shown for the case of self-diffusion, but are also apparent for foreign-atoms in a lattice [37].
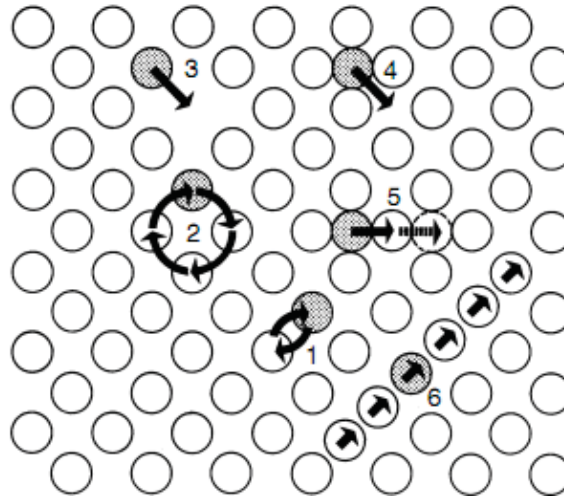
Figure 4.1: Mechanisms of self-diffusion [37]: (1) direct exchange of places, (2) ring-exchange, (3) vacancy mechanism, (4) interstitial mechanism, (5) indirect interstitial mechanism, (6) Crowd-ion.
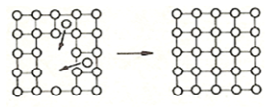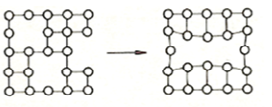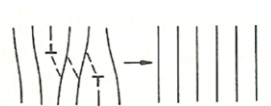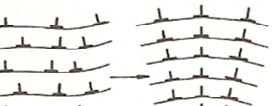
Generally, the interstitial diffusion is a random jump process of an atom, which uses the interstices between the lattice sites of the parent lattice. The interstitial atoms are in solid solution and jump to vacant positions as often as their thermal energy permits, shown in Figure 4.1(4). This process occurs when the solute atoms (e.g. H, C, N) are considerably smaller than the parent lattice atoms. Commonly the miscibility for interstitial solution is very small, which keeps the distortion of the lattice low but a lot of vacant sites for the interstitial atom [47]. The interstitial method of diffusion may also be obtained by parent lattice atoms and is therefore called self-diffusion, as presented in Figure 4.1(4-6).

If the diameter of a solute atom is too large for interstitial lattice sites, the atoms have to occupy substitutional lattice sites. Hence, every motion of a lattice atom is called substitutional diffusion, and occurs mainly by the vacancy mechanism. Although, the direct- or ring-exchange of places, shown in Figure 4.1-(1) and (2), is assumed to be possible, the activation energy is much higher than for vacancy mechanism, Figure 4.1(3). Thus, the main mechanism of atomic motion uses a vacant adjacent lattice site by jumping into the vacancy. The atom moves for one lattice place as the vacancy does, respectively. The vacancy concentration increases rapidly with elevated temperatures, what enhances the possibility for substitutional diffusion [48].

4.2   Recovery

As mentioned before, thin films have a huge concentration of crystal defects, and hence the film is far away from thermodynamic equilibrium. Thermal treatment provides the activation energy to reassemble the crystal defects in several stages. Recovery is a process to reduce the stored internal energy and depends on time and temperature, but as an additional driving force the crystal tries to get closer to the thermodynamic equilibrium [46].

Due to the lowest activation energies, the first step of recovery is the recombination of vacancies and interstitial atoms or their diffusion to boundaries. Moreover, vacancies can rearrange to form voids, as shown in Figure 4.2. At higher temperatures the dislocations are enabled to move and annihilate or arrange in low energy configurations. Both processes can be achieved by glide, climb or cross slip of dislocations. The stacking fault energy, which is strongly affected by solute atoms, droplets or the initial configuration of line defects (e.g. pinning dislocations), determines the occurring rate of dislocation climb or cross slip. While glide of dislocations is already reached at lower temperatures, cross slip and climb needs more activation energy. This results in the formation of regular arrays or low angle grain boundaries (polygonization) [37, 46, 49].

Annihilation		Rearrangement	
	Interstitials fill up vacancies		Vacancies condensate to voids
	Dislocations of opposite sign annihilate		Dislocations build up sub-grain boundaries and rearrange in a low-energy configuration: Polygonization

Figure 4.2: Reactions during recovery, redrawn from [37].

4.3   Recrystallization

Recovery is a relatively homogenous process, which proceeds mainly with time through rearrangement and annihilation of crystal defects, whereas the crystal orientation is not altered. On the other hand recrystallization results in the formation of new strain free crystals, consuming original or already recovered grains. Even after recovery a lot of internal energy is still stored in the microstructure, mainly in form of dislocation arrays

and sub-grain boundaries and this provides the main driving force for recrystallization. It can be assumed, that the higher the impurity content or the density of internal boundaries, the lower the recrystallization temperature [46].

Therefore grain boundaries, but also sub-grain boundaries or regions with a high dislocation density, react as initial nucleation sites. The primary recrystallization requires thermal activation energy and results from nucleation and growth. It can phenomenologically be described by the Johnson-Mehl-Avrami-Kolmogorov relationship [37, 46, 50]. The growth of the recrystallized grains occurs through coalescence of sub-grain boundaries, including especially climb and slip motion of dislocations. Therefore it is even possible that the adjacent sub-grains undergo a rotation, by atomic rearrangement, shown in Figure 4.3(b). Furthermore, recrystallization involves the migration of high-angle grain boundaries. These steps combined, result in a low-energy microstructure with a relatively uniform grain size distribution [37].
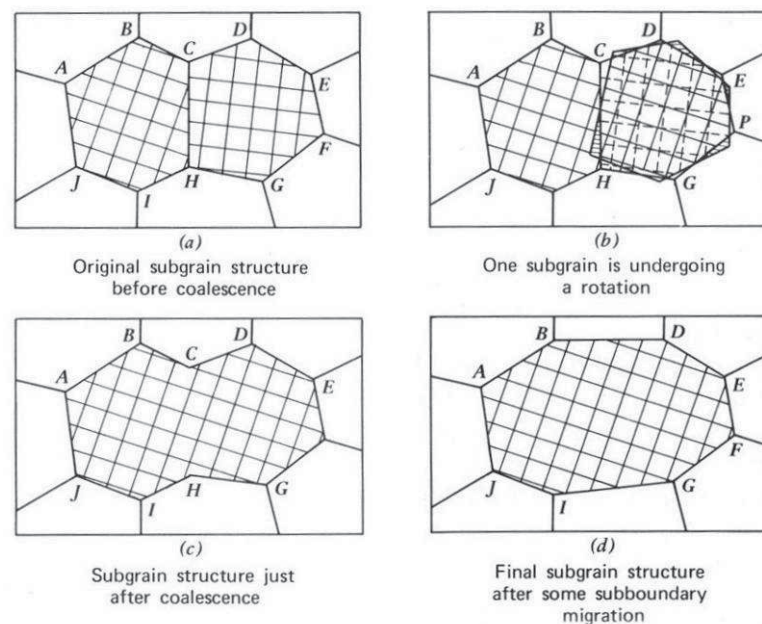
Figure 4.3: Coalescence of subgrains [48].

However subsequent growth of some crystals, which is known as secondary recrystallization or abnormal grain growth, may occur. It is common in coatings with two phases, which are in equilibrium, however the recrystallization occurs autonomously. Second phase particles, solutes or voids practise a pinning force on the

boundaries. Nevertheless, the high temperatures enable the further reduction of grain- and phase boundary energies, which include high angle grain boundary migration. Therefore a bimodal grain size distribution develops when certain crystals enlarge at the expense of primary recrystallized grains [37].

Sputtered coatings exhibit a high defect density and often large levels of compressive stresses, arising from the process. These act as driving forces, and the recrystallization temperature, which is about $0.4*T_m$ in pure materials, can be much lower in PVD-films. Therefore, the recrystallization temperature of thin films depends on the used deposition parameters and the homologous temperature of the coating material [51].

4.4 Decomposition

For the discussion of the temperature influence on a fixed composition of the bulk material, it is inescapable to discuss possible phenomenona in solids. A temperature change from a single-phase regime often results in reaching a thermodynamic regime, where two or more phases are stable. Possible reactions, e.g. precipitation, eutectoid transformations or ordering reactions, are all transformations which usually occur by diffusional nucleation and growth, though there are a few exceptions [46, 47].

Decomposition is mainly driven by the reduction of the total Gibbs free energy of a material. Often metastable structures and phases are created during the deposition process and assumed to be frozen in the as-deposited state. An important part of the internal energy is kept by the bonds between the different atoms of the film. Moreover, a high amount of internal energy is stored in dislocations, grain boundaries, stacking faults, inclusions or free surfaces. Therefore the most efficient way of minimizing the total Gibbs free energy is to reach a minimum in interfacial energy, and a maximum in interatomic bonding energy between the different film atoms. Depending on the strength of the interatomic bonds, an ordering or decomposition of the solid-solution may occur [37].

In case of a resulting total energy gain, thermal activation of the metastable state leads to decomposition. In practice, the formation of nuclei with the smallest total interfacial energy occurs heterogeneously at highly disordered regions. The precipitates X_1 and X_2, with a concentration c_α and c_β respectively, have a different structure and composition than the original composition $X_0^{'}$, with concentration c_0, Figure 4.5(b). The nuclei have

to reach a critical size and preserve the equilibrium composition of the crystal. Growth occurs down-hill diffusion controlled with respect to a minimum energy orientation relationship with the matrix, as shown in Figure 4.4(a).
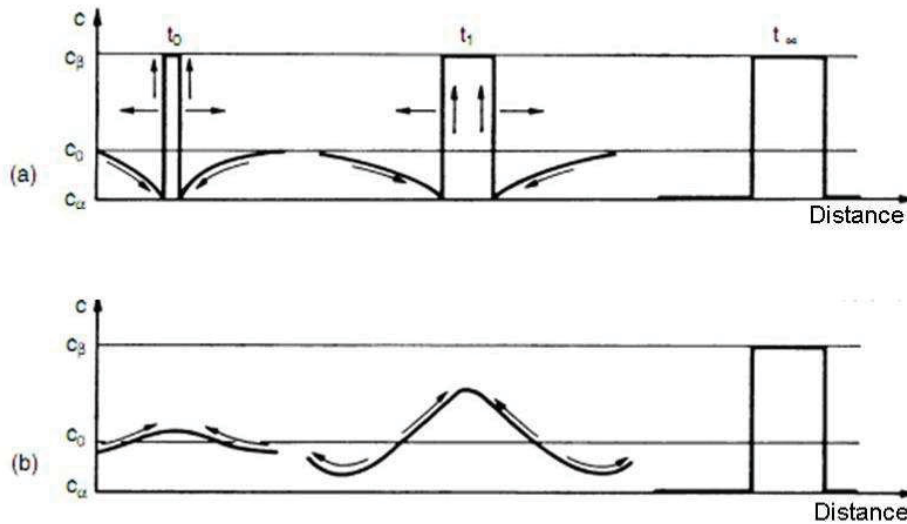
Figure 4.4: Decomposition through (a) nucleation and growth, or (b) spinodal decomposition [37].

In contrast to ordinary decomposition, the spinodal decomposition has no barrier for nucleation. If the alloy concentration c_0 is within the two points of inflection on the free energy curve of a system with a miscibility gap, as given in Figure 4.5(b) for X_0 , thermally induced compositional fluctuations lead to spontaneous decomposition. The created clusters are fully coherent regions with more than one specific atomic compound of the system and tend immediately to grow, therefore without incubation time, to reduce the total free energy. The spinodal decomposition is therefore an up-hill diffusion controlled reaction, as presented in Figure 4.4(b). Nevertheless, to gain a stable configuration nucleation and growth is often necessary [47].
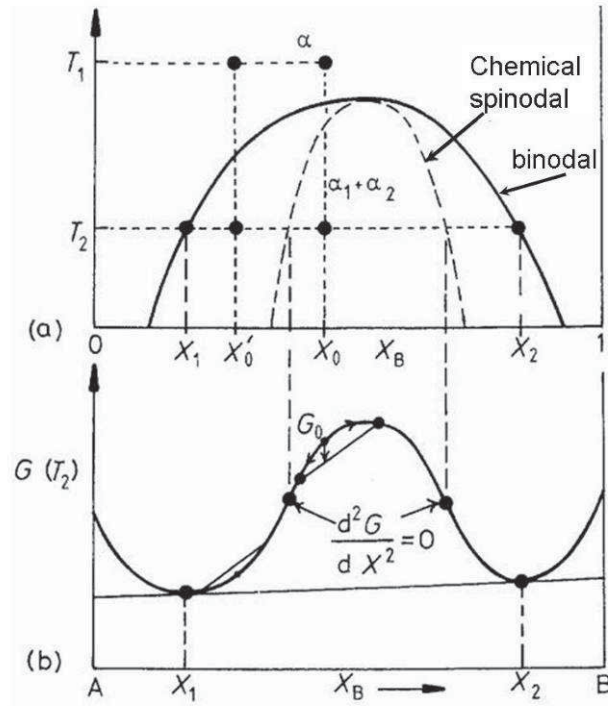
Figure 4.5: (a) Phase diagram with miscibility gap (chemical binodal and spinodal), (b) free energy curve according to (a) [47].

In PVD-coatings decomposition is one of the most important and commonly found processes. However, if a system, as shown above, has a metastable structure due to its deposition process, also spinodal decomposition can occur. An important coating material that exhibits this behaviour is $Ti_{1-x}Al_xN$, which decomposes to TiN and AlN. This reaction is responsible for the high hardness even at elevated temperatures [38] and is treated in chapter 3.3.

5 Experimental

5.1 Deposition

5.1.1 Deposition system

All coatings, investigated in this work, were deposited by DC-reactive magnetron sputtering, employing a modified Leybold-Heraeus A-400 magnetron sputtering unit, as shematically shown in Figure 5.1. Details about this facility are discussed in [52-56]. Argon was used as working gas, whereas Nitrogen served as the reactive gas.
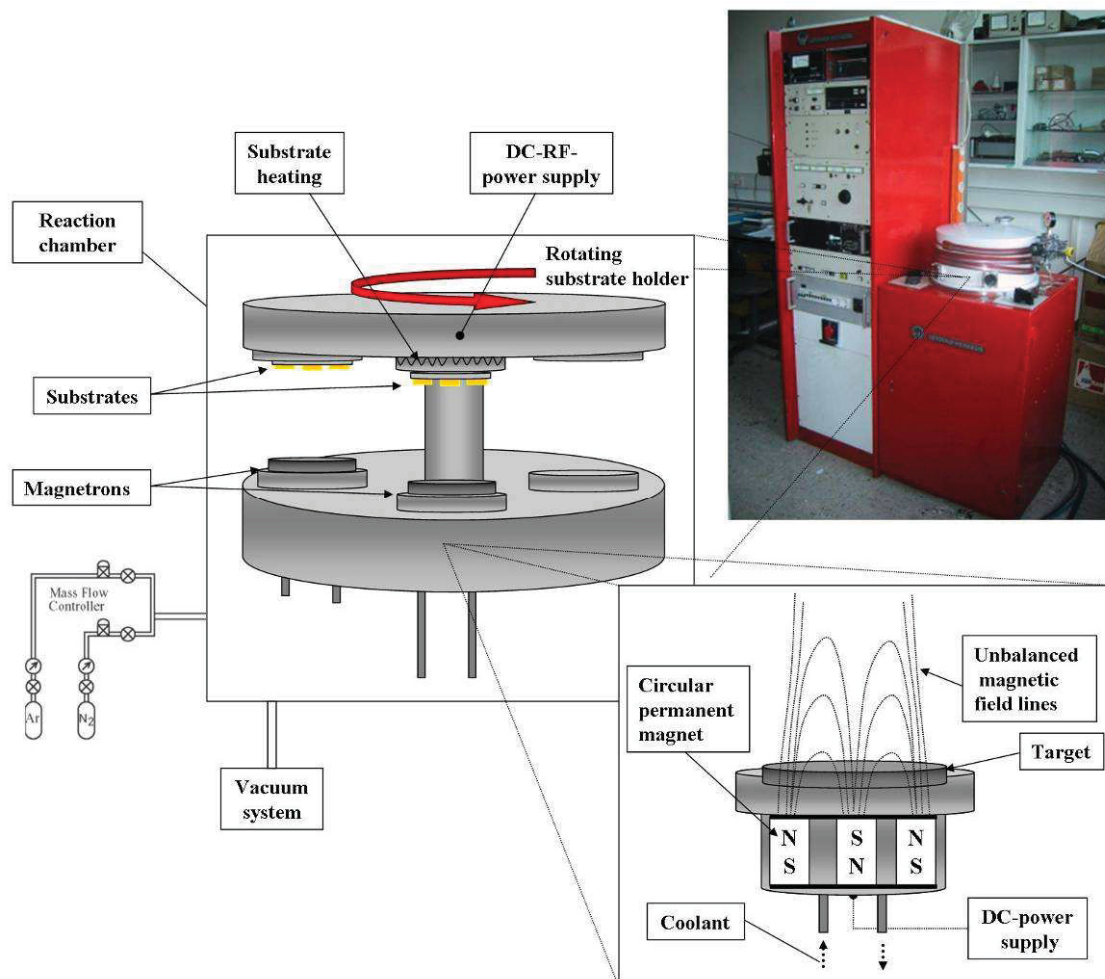
Figure 5.1: Schematic drawing of the modified Leybold-Heraeus sputtering equipment.

Chamber:

The reaction chamber is made of stainless-steel (420*200 mm) and consists of two parts. The upper part forms the top cover, which can be tilted and heated by an external resistance heater. The lower part includes the three feedthroughs for the magnetron targets, where usually two of them are mounted. Additionally it contains the connections to the pumping system and the gas control units, the voltage supply as well as the pressure gauges. Further a rotateable holder is mounted in the chamber, incorporating the substrate holders and places for additional cathodes.

Magnetron-cathodes

The three magnetron cathodes in the bottom of the reaction chamber can house different targets with 76.2 mm (3") in diameter and variable thickness. The targets are bonded with Indium onto the cathode to achieve good thermal and electrical conductivity. DC-Power is supplied by a Leybold-Heraeus DC-generator. The magnetron is a circular cathode, including permanent magnets (Gencoa PK 75), whose backside is water cooled and isolated by a Teflon base plate, shown in Figure 5.1.

Substrate holder

Opposite the target, at a distance of ~6 cm, the substrates can be mounted in different substrate holders, depending on the substrate shape. The substrate holders are fixed on a rotating holder, which can be continuously heated from 80 to 550 °C and/or biased.

Vacuum system

To evacuate the reaction chamber a pre-vacuum pumping system (rotary vane vacuum pump Pfeiffer DUO 20) and a turbomolecular pump (Leybold Turbovac 361) were used. The control and power supply was carried out by a (Leybold Turbotronic NT 20) frequency changer.

Gas- and pressure control system

Applying a gas flow measure- and control-unit (two mass flow controller Tylan RO-7031, controller Tylan RO-7030), the partial pressures of the working gas (argon flow up to 200 sccm) and reactive gas (nitrogen flow up to 50 sccm) have been controlled

independently of each other. The measurement of the total pressure was done by a Leybold Combivac CM 31.

Power supplies

For RF-sputter cleaning prior to deposition, a RF-generator (ENI ACG-6B) was used.

A Leybold-Heraeus DC-sputter generator is integrated in the basic system and enables a continuous DC-power regulation of the plasma from the ignition point to maximum load. The bias voltage during deposition was applied by a DC-bias generator (Sorensen DCR 300-1.5).

5.1.2 Targets and substrates

All targets used in this work are manufactured by Plansee AG and listed in Table 1.

Table 1: Compositions of the targets used.

Target-system	Chemical composition				Purity [%]
	Ti [at.%]	Al [at.%]	Y [at.%]	Nb [at.%]	
$Ti_{0.50}Al_{0.50}$	50	50	-	-	99.9
$Ti_{0.49}Al_{40.49}Y_{0.02}$	49	49	2	-	99.9
$Ti_{0.48}Al_{0.48}Y_{0.04}$	48	48	4	-	99.9
$Ti_{0.46}Al_{0.46}Y_{0.08}$	46	46	8	-	99.9
$Ti_{0.49}Al_{0.49}Nb_{0.02}$	49	49	-	2	99.9
$Ti_{0.48}Al_{0.48}Nb_{0.04}$	48	48	-	4	99.9
$Ti_{0.46}Al_{0.46}Nb_{0.08}$	46	46	-	8	99.9

The different investigation methods required different substrates. Thus, for the main research activities thin films were applied on sapphire substrates with a $(1\bar{1}20)$-orientation, 1*1 cm size and 0.5 mm thickness. Sapphire was chosen because of its high thermal stability, which minimizes the interdiffusion during the annealing experiments. Low-alloyed steel foils (Ø 75*0.05mm) were deposited to produce coating material for powder measurements, mainly in STA, as described in more detail in section 5.2.3.

5.1.3 Deposition procedure

All coatings were deposited as follows:

- ✓ Precleaning of the substrates in an aceton- and ethanol-bath, each for 5 minutes using an ultrasonic cleaner. Drying of the substrates with a fan.

- ✓ Mounting of the substrates and evacuation of the chamber.

- ✓ Activation of the outer heating segment for 45 minutes, pressure Pa, then additional activation of the inner heater at 500 °C for another 15 minutes.

- ✓ After cooling for ~45 min, the residual total pressure is ~$2*10^{-3}$ Pa. Then activation of the inner heater (500 °C) and waiting for 15 minutes.

- ✓ Presputtering of the target to remove impurities on the target surface, applying 45 sccm argon and 400 W for 5 minutes on the DC-sputter generator. To avoid cross-contamination, the substrate is moved away from the position of facing the target.

- ✓ Turning down the DC-sputter generator to 80 W, to sustain the plasma, while etching the substrates with the RF-generator for 10 minutes, to clean the substrate surface prior to deposition. This was conducted with 100 W of the RF-generator at a pressure of ~$1.2*10^{-2}$ Pa.

- ✓ Starting the deposition process after moving the substrate holder to the correct position, directly facing the target. Switching off the RF-generator and raising the power on the DC-sputter generator to 400 W. Lowering the Ar-gas flow to 9 sccm and introducing N-gas flow of 7.9 sccm. Application of bias voltage of -50 V which causes a current of ~55 mA.

- ✓ Deposition time of 180 min for all $(Ti_{1-x}Al_x)_{1-z}M_zN$-films on low-alloy steel sheet, and 60 min for the $(Ti_{1-x}Al_x)_{1-z}Y_zN$-coatings and 45-60 min for the $(Ti_{1-x}Al_x)_{1-z}Nb_zN$-coatings on sapphire.

- ✓ End of deposition by switching off every power supply except cooling and vacuum system.

All samples were produced, using the same above mentioned process parameters, except for the deposition time.

5.2   Characterization

5.2.1   Scanning electron microscopy (SEM)

Sample surfaces and cross-sections were investigated with a Zeiss Evo50 scanning electron microscope (SEM). The coating chemical composition was determined with an attached Oxford Instruments INCA energy-dispersive X-ray analysis device (EDX). Elemental Al, Nb and Y standards and a TiN-thin film were used a standards. The composition of the latter was analysed by Rutherford Backscattering (RBS) as described in [57]. Further the film thickness was measured during cross-sectional SEM investigations.

5.2.2   X-ray diffraction (XRD)

X-ray diffraction is a non-destructive standard investigation method to determine the structure and phase composition of solids. In dependence of wavelength, lattice spacing and lattice periodicity X-rays are scattered, leading to constructive or destructive interference. The basic condition for constructive interference, as a consequence of the periodicity of the lattice, is given by Bragg´s law [58]:

$$n * \lambda = 2 * d_{(hkl)} * \sin \Theta , \qquad\qquad (5.1)$$

where n is the value of order, λ is the wavelength of the X-rays, $d_{(hkl)}$ gives the lattice spacing with miller indices (h, k, l) and Θ is the incident angle.

In this thesis the following experimental setups for diffraction analysis were applied.

- ✓ In Bragg-Brentano alignment, the source rotates the angle Θ, while the detector moves 2Θ, commonly determined as Θ-2Θ configuration. In this geometry, only lattice planes with the plane normal parallel to the beam are measured. As shown in Figure 5.2(a), the scattering vector Q, resulting from the incident wave vector K_0 (source) and the scattered wave vector K (detector), remains always perpendicular to the surface. The wave vector K is calculated as $K=2\pi/\lambda$, and the resulting scattering vector Q as $Q=K-K_0$. Constructive interference only occurs if Q hits a reciprocal space point, which fulfills the Laue condition in reciprocal space and Bragg´s law in normal space [36].

✓ In the grazing incident alignment the source is fixed at an angle α_i, while the detector rotates 2Θ. Due to the fixed source, the incident wave vector remains at the low angle α_i, whereas the scattered wave vector K moves, as shown in Figure 5.2(b). Thus only non-parallel lattice planes lead to a signal in the detector [36]. The scattering vector Q is not perpendicular to the sample surface and furthermore not perpendicular to the single crystal substrate. Thus grazing incidence scans open the possibility to measure the film without substrate influence and were used to confirm the findings of the Θ-2Θ measurements.
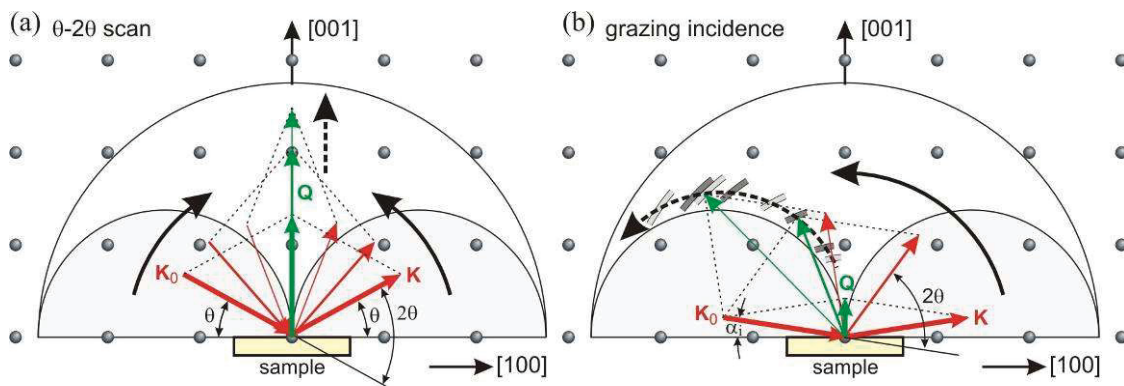
Figure 5.2: Schematic drawing of diffraction techniques (a) Θ-2Θ scan and (b) grazing incidence [36].

For this thesis high temperature and room temperature investigations were done. The in-situ investigations have been applied on a Phillips X´pert MPD Diffractometer, combined with a Bühler HDK 2.4 high-temperature high-vacuum chamber with a Be-window. The room temperature measurements were mainly performed on a Bruker D8 Advance, a Phillips MRD and a Phillips D500 unit.

In case of the high temperature measurements the sample was positioned on the inner Ta-filament, as presented in Figure 5.3, and the chamber was evacuated down to about 10^{-1} Pa. To increase the temperature the sample was simultaneously heated from the bottom and the surrounding by two Ta-filaments. In the HT-XRD only Θ-2Θ scans were possible, due to the construction of the Be-window of the heating chamber, using the parameters given in Table 2.
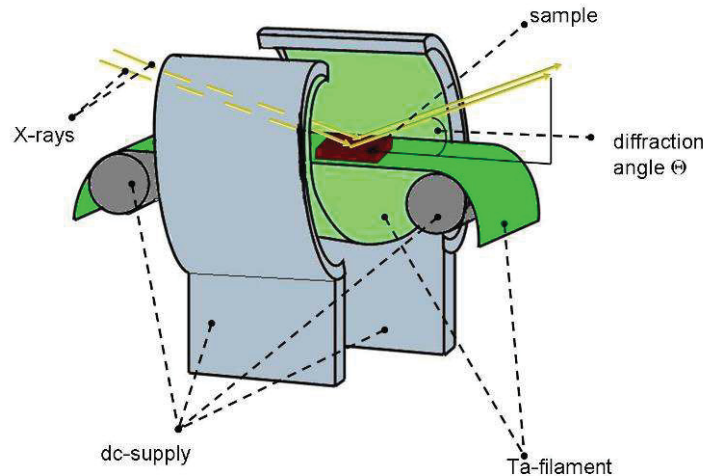
Figure 5.3: Schematic of the high-temperature (HT) filaments in Θ-2Θ alignment.

Table 2: Main XRD-parameters used for the investigations.

XRD-mode	XRD-type	Cu-K$_\alpha$-radiation [Å]	high voltage [kV]	tube current [mA]	time step [s]
high temperature	Phillips X´pert	1.54056	40	40	1.2
room temperature	Bruker D8	1.54056	40	40	0.5

The room temperature measurements were performed on a Phillips MRD and a Bruker D8 Diffractometer, according to the parameters in Table 2. The confirmation of the high-temperature scans was carried out on as-deposited and post-annealed samples in both XRD equipments. In addition to Bragg-Brentano geometry, also grazing incidence mode was used. Within the Phillips MRD, the samples were glued on a glassy object plate and fixed in the goniometer.

The ancillary measurements were done in Bragg-Brentano and grazing incidence mode, using the Bruker D8 XRD. Within this diffractometer it is possible to rotate the samples during the measurement. The sample arrangement is shown in Figure 5.4. Therefore it was possible to gain information of the film without the dependence on the orientation of the microstructure.
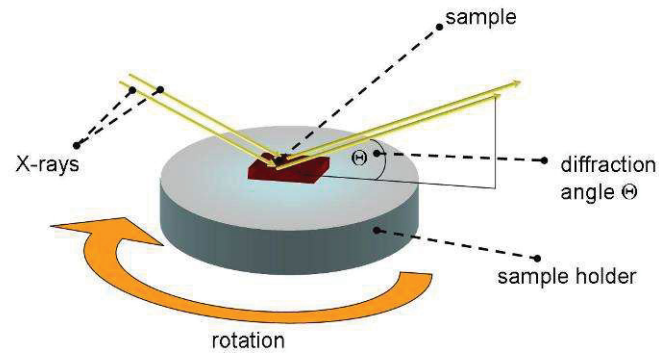
Figure 5.4: Measurement setup in the Bruker D8 Advance.

5.2.3 Simultaneous thermal analysis (STA)

Simultaneous thermal analysis, combining a differential scanning calorimeter (DSC), thermo gravimetric analysis (TGA) and mass spectrometry (MS), was used to investigate thermally activated processes. In general a calorimeter measures the heat flow from or to a sample continuously and compares the occuring heat flow with a known reference material [59]. The used system combines the DSC measurements with an accurate gravimeter, which monitors the total mass development of the sample during the time-temperature program. Moreover a mass spectrometer was utilized to observe the volatile fractions of the film at higher temperatures.

In this work a Netsch STA 409C system, schematically shown in Figure 5.5, and a Setaram STA were utilized. The equipment calibration is explained in detail in Ref. [18].
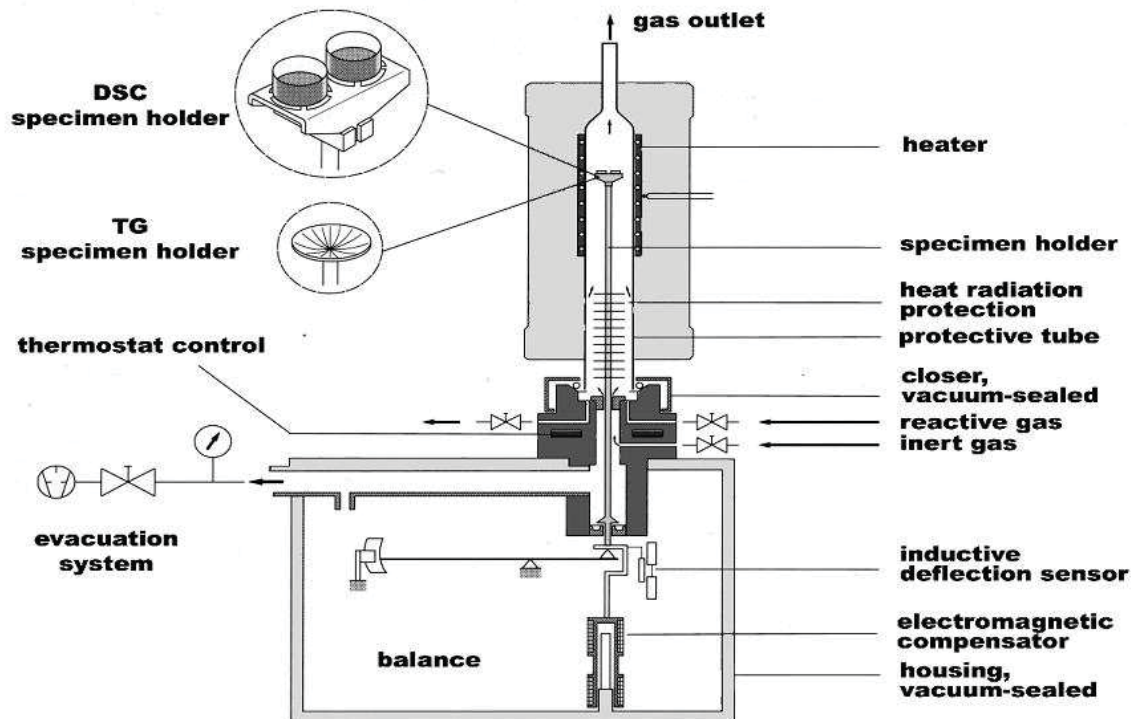
Figure 5.5: Schematic of the Netzsch-STA 409 C simultaneous thermal analyzer (STA) [60].

All analyses were done on powder samples. The powder of the films was gained from coated low-alloy steel foils, where the steel was dissolved in a 10 mole-%-nitric-acid. This procedure gives the possibility to measure the film, without substrate influence. After drying and grinding, the pure thin film powder was weighed to a mass of about 30 mg, and filled into a Pt-Rh crucible with an Al_2O_3-inlay. An empty crucible was used as reference.

The measurements were carried out in Ar-atmosphere, with 100 sccm flow on the sample outlet and 30 sccm on the balance.

The temperature-time program, which controlled the heating and cooling conditions, is presented in Figure 5.6. After an initial isothermal treatment at 150 °C for residual humidity removal as well as balance equilibration, the sample was heated up to 1400 °C at 20 K/min. After the first annealing run the sample was cooled to 150 °C at 20 K/min, and a subsequent isothermal equilibration step at 150 °C was hold for 30 min. Finally a second heating and cooling step of 20 K/min to and from 1400 °C was performed.
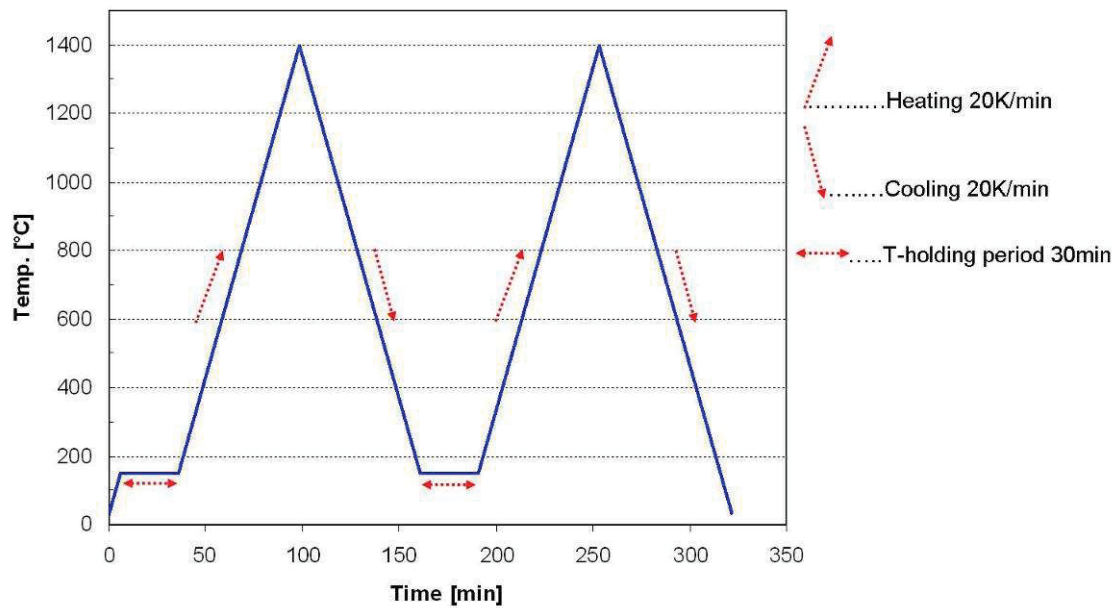
Figure 5.6: Temperature-time program used for the STA measurements.

With the first heating step reversible and irreversible processes can be determined, whereas the second heating allows the measurement of only reversible reactions. To ensure a correct measurement, a baseline for calibration was measured before with two empty crucibles. The attached gravimeter has an accuracy of $1.25*10^{-6}$ g and is positioned below the sample holder. The TGA was started simultaneously with the DSC and the MS.

Hence, with STA exact data of mass-, enthalpy- and composition-development, dependent on time and temperature were obtained. Therefore, this method allows to distinguish reversible e.g. melting and crystallisation, phase transition from irreversible processes e.g. recovery, recrystallisation, decomposition or precipitation. [61].

5.2.4   Transmission electron microscopy (TEM)

Transmission electron microscopy is an excellent method for microstructural investigations on nanometer-size level. In contrast to an optical microscope, TEM employs electrons for imaging a sample. The rough principle of a TEM can be described as thermally emitted and accelerated electrons, which pass several electromagnetic lenses before they transmit the sufficiently thin sample. According to the de Broglie relationship [12], the small effective wavelength is:

$$\lambda = \frac{h}{\sqrt{2*m*q*V}} \tag{5.2}$$

Where m and q are the electron mass and charge, h is Planck´s number and V marks the potential difference. An acceleration voltage for a TEM of 200 keV leads to a wavelength of $\sim 10^{-12}$ m, compared to visible light with $\sim 10^{-7}$ m [36]. Therefore TEM provides a resolution of at least one magnitude higher compared to SEM [22].

For this thesis a FEI Tecnai G^2 TF20 UT microscope, shown in Figure 5.7(a), attached with an EDX, electron energy loss spectroscope (EELS) and a scanning transmission electron microscope (STEM) was used for the microstructural investigations. The electron beam path in a TEM is shown in a schematic drawing in Figure 5.7(b). The illuminating part, consisting of the field emission gun (FEG) and mainly two condenser lenses, is responsible for the impacting electron beam which can be assumed parallel. The electron waves are forward-scattered and diffracted from the sample atoms of the investigated area and combined in the imaging part. The optical resolution is mainly limited by the resolution of the objective lens [62, 63].
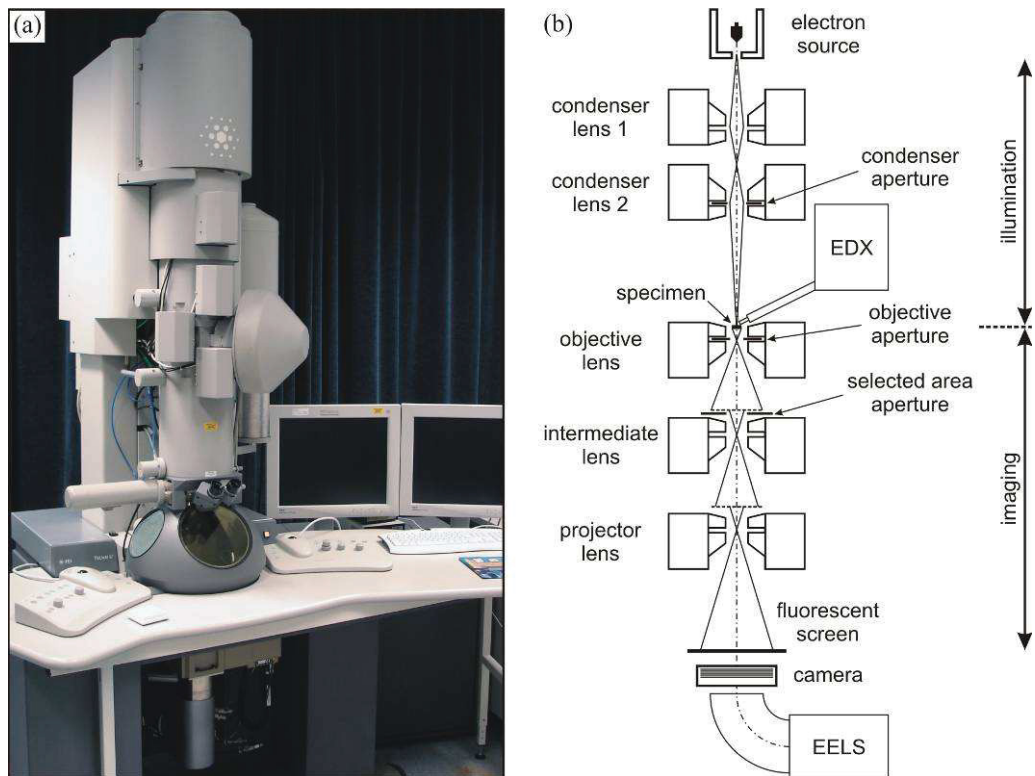
Figure 5.7: (a) FEI Tecnai G2 TF20 UT STEM transmission electron microscope at the Linköping University [36], (b) schematic drawing of an analytical TEM (modified [64]).

Depending on the used apertures and configuration of the lenses, different imaging or analytical modes can be employed. The used TEM provides the main operational modes, *bright* and *dark field imaging*, *lattice imaging*, as well as *diffraction*. The beam path within the imaging part of the column marks the different modes, shown in Figure 5.8.

Recombining the primary transmitted and one or more of the diffracted beams leads to the method of *lattice imaging* of periodic structures on atomic level, shown in Figure 5.8(b). The obtained image in *bright field*, Figure 5.8(c), uses only the primary transmitted beam. The diffracted beams are excluded by the objective aperture in the back focal plane of the objective lens. Using intermediate and projection lenses, the central beam can be magnified and thus provides the basic TEM mode. In *dark field* mode, Figure 5.8(d), only one diffracted beam is utilized to create an image. The central beam has to be blocked in this mode, what can be reached by shifting the aperture. By altering the intermediate lens the object plane is shifted and it is possible to convey the information of the whole specimen in diffraction patterns. This is called diffraction

mode and presented in Figure 5.8(a). Inserting an aperture in the image plane of the objective lens limits the investigated sample region to a selected area. Therefore, this enhanced diffraction method is called selected area electron diffraction (SAED) and enables the determination of crystallographic and orientation effects of neighboring crystallites [65-68].
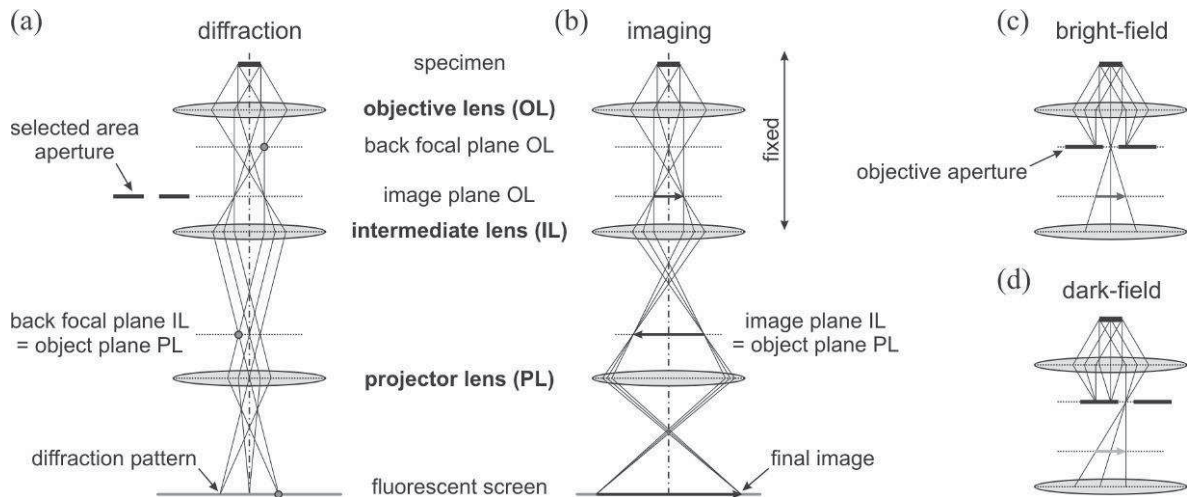
Figure 5.8: Beam path in the imaging part of the TEM for the main applications [36]: (a) diffraction-, (b) imaging-, (c) bright-field- and (d) dark-field mode.

A TEM provides a large range of possibilities to avoid aberrations and improve the quality of the resulting image. However the resulting image strongly depends on the quality of the specimen itself. To create a sufficiently thin area from the interface to the surface of the film the cross-sectional samples were produced as follows:

- ✓ Cutting the coated substrates to a size of 1.8*1 mm, using a rotating diamond coated blade.
- ✓ Insertion of two platelets in a Ti-disc, facing each other with the coated side.
- ✓ Fixing of the platelets in the disc with a conductive glue.
- ✓ Grinding and polishing of the specimen disc down to a thickness of ~ 50 μm.
- ✓ Ar-ion polishing of the sample center in a Gatan precise ion polishing system (PIPS), with an energy of ~5 kV and at 5° angle from top and below, till a small hole emerged. Reducing the energy to ~2.2 kV for the last step gave a polished thin sample surface in the investigation regions.

For this thesis, TEM was used mainly in bright field mode to obtain the microstructural images. To distinguish the apparent phases and the crystallographic orientation in the

as-deposited and post-annealed state, the diffraction mode was utilized as a good complementary method to the XRD-measurements.

5.2.5 Nanoindentation

For the evaluation of hardness, popular methods e.g. Vickers, Knoop, Brinell or Rockwell, can be employed, using differently indenter shapes. Altogether the projected area (A) of the remaining imprint after the indentation procedure is optically determined and related to the applied load (P_{max}). Consequently the hardness (H) of the material [69] is generally described as:

$$H = \frac{P_{max}}{A}$$
(5.3)

To avoid substrate influence in the measurement, the indentation depth should not exceed 10 % of the coating thickness. At very low indentation depths, however, only the elastical response of the material is determined, resulting in largely overestimated H and E-values [70, 71]. Therefore, hardness measurements of thin films have to be performed within a tight depth margin, utilizing the Oliver and Pharr method [72].

Using a load-depth sensing indentation unit, in case of this thesis the UMIS nanoindenter, the constraints in hardness and elastic modulus determination can be overcome. A three-sided Berkovich indenter, with a face angle of 65.27° was used [73]. This indentation method is not dependent on the residual imprint, but measures a load-displacement curve, shown in Figure 5.9, where the parameters h_e and h_r are the elastic and the residual displacement of the tip, respectively. For the calculation of hardness and elastic modulus, the indentation area is substituted by the penetration depth, which can be related to an indenter geometry depending factor and the contact stiffness dP/dh at h_c, which means the maximum depth. Fitting the upper 80 % of the unloading curve, performs the evaluation of the stiffness [74-76].
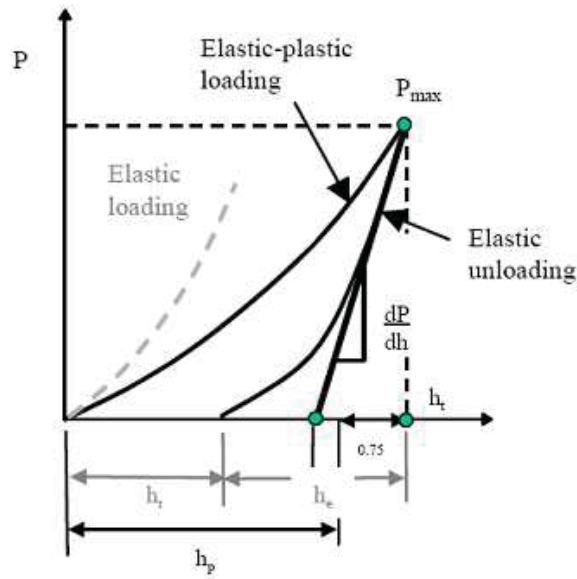
Figure 5.9: Load-displacement curve during nano-indentation [73].

For this thesis increasing loads, starting with 5 mN, were used to determine the proper measurement load- and depth-level and a load of 25 mN was found to be optimum for proper measuring the coating properties. At minimum 20 indents per coating were done to achieve a good statistic of the measured data.

6 Results and discussion

6.1 Chemical composition

$Ti_{1-x}Al_xN$ were alloyed with yttrium or niobium by using powder-metallurgically produced targets with a constant Ti/Al ratio of 1 and the addition of 2, 4, and 8 at.% of the alloying element. With the chosen low-temperature PVD-process ($\sim$ 0.2-0.3 T/T_m) and extremely high cooling rates (10^{-13} Kmin^{-1}), limited ad-atom mobility was achieved. This results in the formation of a supersaturated solid-solution $(Ti_{1-x}Al_x)_{1-z}M_zN$, where M is the alloying element yttrium or niobium.

With the above given parameters the coating was supposed to obtain directly the chemical composition of the target, and a nitrogen content of $\sim$51 %. However, slightly over-stoichiometric coatings, with compositions as given in Table 3, were achieved within this unbalanced magnetron sputtering process.

Table 3: Chemical compositions of the produced coatings with respect to the target.

Target system at.%	Coating composition at.% (metal sublattice)				Coating nomenclature	Al/(Ti+Al) at.%- ratio
	Ti	Al	Y	Nb		
$Ti_{0.50}Al_{0.50}$	42	58	-	-	$Ti_{0.42}Al_{0.58}N$	0,58
$Ti_{0.49}Al_{0.49}Y_{0.02}$	40	57	3	-	$Ti_{0.40}Al_{0.57}Y_{0.03}N$	0,58
$Ti_{0.48}Al_{0.48}Y_{0.04}$	37	58	5	-	$Ti_{0.37}Al_{0.58}Y_{0.05}N$	0,61
$Ti_{0.46}Al_{0.46}Y_{0.08}$	36	55	9	-	$Ti_{0.36}Al_{0.55}Y_{0.09}N$	0,60
$Ti_{0.49}Al_{0.49}Nb_{0.02}$	44	54	-	2	$Ti_{0.44}Al_{0.54}Nb_{0.02}N$	0,55
$Ti_{0.48}Al_{0.48}Nb_{0.04}$	41	55	-	4	$Ti_{0.41}Al_{0.55}Nb_{0.0.4}N$	0,58
$Ti_{0.46}Al_{0.46}Nb_{0.08}$	35	57	-	8	$Ti_{0.35}Al_{0.57}Nb_{0.08}N$	0,61

6.2 Structure

For the further discussion the films are termed as 3 at.%, 5 at.%, and 9 at.% containing Y, and 2 at.%, 4 at.%, and 8 at.% Nb in the metal sublattice.

The Al/(Ti+Al) ratio is in a range between 0.55 and 0.61, which corresponds to already reported investigations on magnetron sputtered films, if prepared from Ti-Al compound targets with an Al/Ti ratio of 1 [77-79].
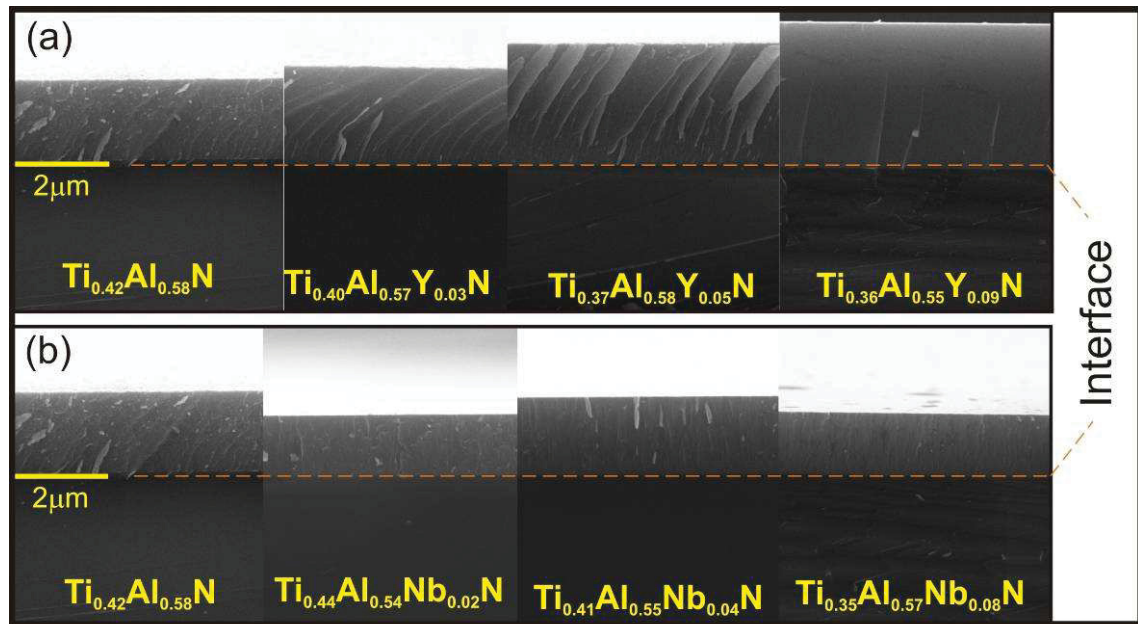
Figure 6.1: SEM fracture cross-sections of (a) $(Ti_{1-x}Al_x)_{1-z}Y_zN$ and (b) $(Ti_{1-x}Al_x)_{1-z}Nb_zN$-thin films, as a function of the chemical composition.

Moreover, the variation of the target composition leads also to changing film thicknesses which are shown in Figure 6.1(a,b). The observed film thicknesses, for constant deposition time in the case of Y, refer to different deposition rates and different unit cell parameters of the cubic and hexagonal phase. The unit cell volume of the hexagonal phase V_h is about 1/3 larger compared to the cubic unit cell volume V_c. The incorporation of Y results in larger unit cell volumes and enlarged lattice parameters of the fcc-$Ti_{1-x}Al_xN$ fraction. The film thickening can be explained by the increasing amount of hexagonal phase fraction with increasing Y-amount, resulting in an increasing deposition rate, from 0.033 μm/min for $Ti_{1-x}Al_xN$ to about 0.055 μm/min for the coating containing 9 at.% Y in the metal sublattice. The according investigations for Y on the lattice parameters are further explained in [78]. The Nb-containing films

exhibit an increasing deposition rate from 0.033 to ~0.045 μm/min with increasing the Nb-content from 0 at.% to 8 at.% Nb in the metal sublattice. The alternating coating thickness evolves because of the different deposition times.
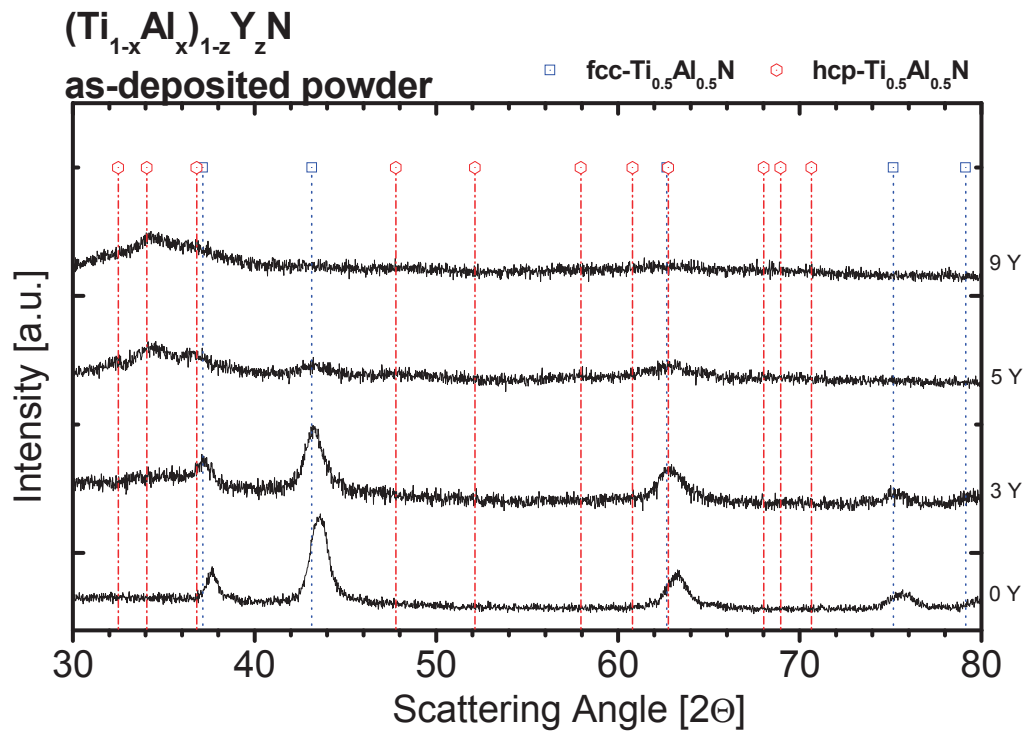
XRD-patterns of the as-deposited $(Ti_{1-x}Al_x)_{1-z}Y_zN$ and $(Ti_{1-x}Al_x)_{1-z}Nb_zN$ coatings are shown in Figure 6.2 and Figure 6.3, respectively. These measurements were done on powder, gained as explained in chapter 5.2.3, to investigate a macro-stress-free coating material, which is not influenced by substrate interaction.

The basic composition of $Ti_{0.42}Al_{0.58}N$ depicts a single phase cubic structure with a lattice parameter a_c of 4.177 Å, according to the Cohen-Wagner method [80]. Due to the Al/(Ti+Al) ratio of the film, the peak maximum of the fcc-$Ti_{0.5}Al_{0.5}N$ peaks is slightly shifted towards the fcc-AlN peaks, as shown in Figure 6.2.

6.2.1 $(Ti_{1-x}Al_x)_{1-z}Y_zN$-thin films

Addition of 3 at.% Y in the metal sublattice leads to a peak shift of the fcc-$Ti_{1-x}Al_xN$ peaks to lower angles, which can be explained by substitution of Ti- or Al-lattice sites by larger Y-atoms and therefore an enlargement of the fcc-parent-lattice. Furthermore, small fractions of the hexagonal phase can be detected at lower diffraction angles. For 5 at.% Y in the metal sublattice the hcp-$Ti_{1-x}Al_xN$ fractions appear more clearly, growing at the expense of fcc-$Ti_{1-x}Al_xN$. Finally at 9 at.% Y only traces of fcc-$Ti_{1-x}Al_xN$ can be detected, while the main structure is built up by hcp-$Ti_{1-x}Al_xN$. This development from cubic to hexagonal structure with increasing Y-amount is a direct result of a decreasing solubility limit of fcc-AlN in fcc-$Ti_{1-x}Al_xN$ and therefore an earlier transition regime from cubic to hexagonal structure.

Figure 6.2: XRD-patterns of as-deposited powdered $(Ti_{1-x}Al_x)_{1-z}Y_zN$-samples, the positions for the fcc- and hcp-$Ti_{0.5}Al_{0.5}N$ are taken from Ref. [78].

6.2.2 $(Ti_{1-x}Al_x)_{1-z}Nb_zN$-thin films

In comparison to the Y-containing films, XRD-patterns of Ti-Al-N alloyed with Nb are presented in Figure 6.3. Here, also a peak shift towards the fcc-TiN can be observed with increasing Nb-amounts, starting from the $Ti_{0.42}Al_{0.58}N$ composition. The incorporation of the Nb-atoms takes also preferably place on Ti- and Al-lattice sites of the fcc-$Ti_{1-x}Al_xN$. After deposition, only a single-phase cubic structure can be detected for all Nb-contents investigated.
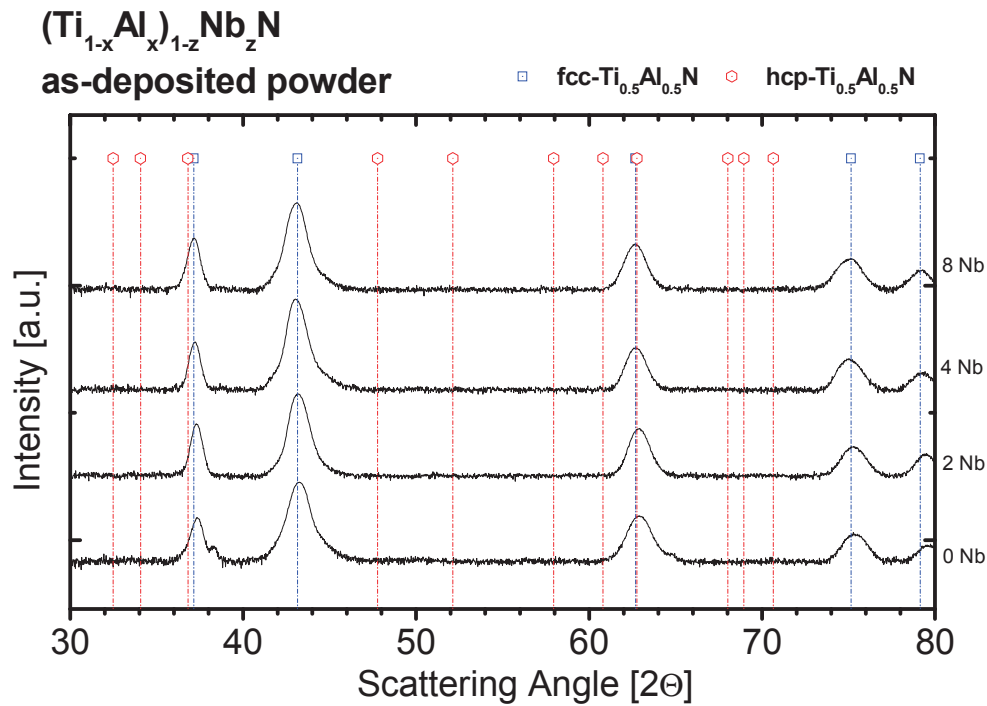
Figure 6.3: XRD-patterns of as-deposited powdered $(Ti_{1-x}Al_x)_{1-z}Nb_zN$-samples, the positions for the fcc- and hcp-$Ti_{0.5}Al_{0.5}N$ are taken from Ref. [78].

In reference [78], Moser et al. report that for the Y-induced hexagonal phase, the lattice parameter a_h= 3.075 Å for 3 at.% Y increases to a_h= 3.205 Å at 9 at.% Y in the metal sublattice, whereas the c-axis shrinks from c_h= 5.295 Å down to c_h= 5.220 Å, respectively.

The determination of the lattice parameters for the Nb-containing films was, also achieved by using the Cohen-Wagner method. Beginning with a_c = 4.177 Å for $Ti_{42}Al_{58}N$, the cubic lattice parameter increases to a_c= 4.181 Å at 2 at.% Nb, to 4.184 at 4 at.% Nb, and finally to 4.190 Å for 8 at.% Nb in the metal sublattice. It is noteworthy, that the 8 at.% Nb-coating, at a Al/(Ti+Al) ratio of 0.61, still maintains a cubic structure, where the 9 at.% Y-coating depicts a nearly single phase hexagonal structure.

6.3 Morphology

Observations of cross-sectional samples in SEM show remarkable differences with increasing Y- or Nb-content. At already low resolution, as shown in Figure 6.1, a refinement of the microstructure can be seen for the $(Ti_{1-x}Al_x)_{1-z}Y_zN$-coatings, whereas

no structural change occurs for the $(Ti_{1-x}Al_x)_{1-z}Nb_zN$-films. Therefore cross-sectional TEM and high-resolution TEM (HR-TEM) observations are preferred to give more information of the structure and morphology of the as-deposited films.

6.3.1 $(Ti_{1-x}Al_x)_{1-z}Y_zN$-thin films

An yttrium induced grain refinement for TiAlN-based coatings is already reported in [78, 81, 82], and is confirmed as shown in Figure 6.4. The $Ti_{0.42}Al_{0.58}N$ coating has a typical columnar structure with a column width of 20-25 nm, grown according to a zone-T of Thornton´s SZM.
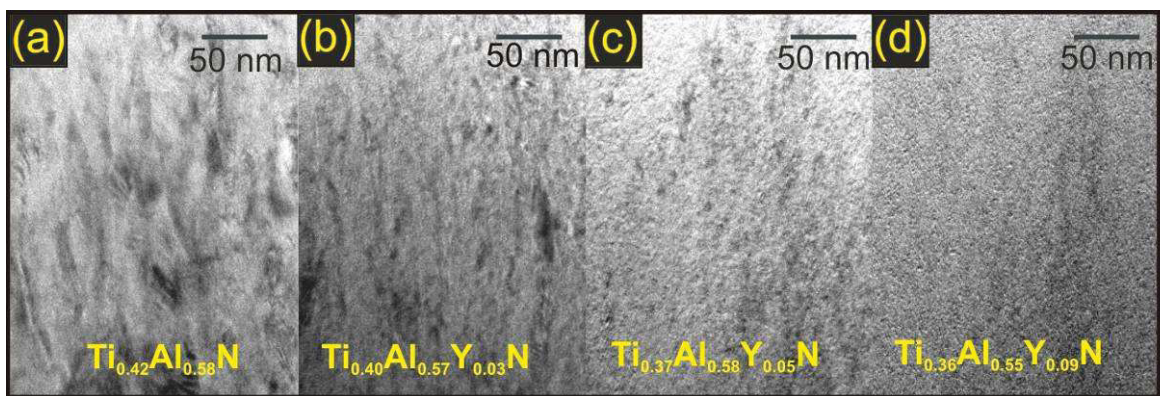
Figure 6.4: Cross-sectional TEM-images of as-deposited $(Ti_{1-x}Al_x)_{1-z}Y_zN$ with 0 at.% (a), 3 at% (b), 5 at.% (c) and 9 at.% Y (d), in the metal sublattice.

The cross-section TEM-images of the Y-coatings, shown in Figure 6.4, propose a decreasing feature size from 15-20 nm for 3 at.% Y, ~10 nm for 5 at.% Y to finally ~5 nm at 9 at.% Y in the metal sublattice. This drastic shrinkage of the column- and grain size is responsible for the broadening of the XRD peaks in Figure 6.2. The grain size distribution is roughly constant over the thickness of the film. At this magnification the decreasing particle size arises obviously, however no distinction between the two phases, which appear in the XRD-patterns, was possible. The grain boundaries appear less developed respectively.

All substrates used in this work, were RF-plasma etched before deposition. Therefore an amorphous layer with a few 10 nm width develops before the film starts to grow continuously and consequently no preferential crystal orientation is given by the substrate. The amorphous interlayer is visible in Figure 6.5, where the substrate is at the bottom of each image. The single-phase cubic $Ti_{0.42}Al_{0.58}N$ exhibits featherlike

columnar growth, as indicated by the slashed lines in Figure 6.5(a). These columns are narrower at the interface near region and become larger towards the surface. Hence, preferential crystal orientations grow with minimized energy from competitive growth. As shown in Figure 6.5(b), already 2 at.% Y in the target, creates thinner columns in the interfacial region, which is maintained over the whole coating thickness. With the addition of Y to $Ti_{0.42}Al_{0.58}N$ the formation of hexagonal phase leads to renucleation. With 5 at.% of Y, the development of continuous columns is interrupted and equiaxed crystallites of hexagonal and cubic structure develop as presented in Figure 6.5(c). The grain size further decreases to ~5 nm with an increasing Y-amount of 9 at% in the metal sublattice of the coating, see Figure 6.5(d).
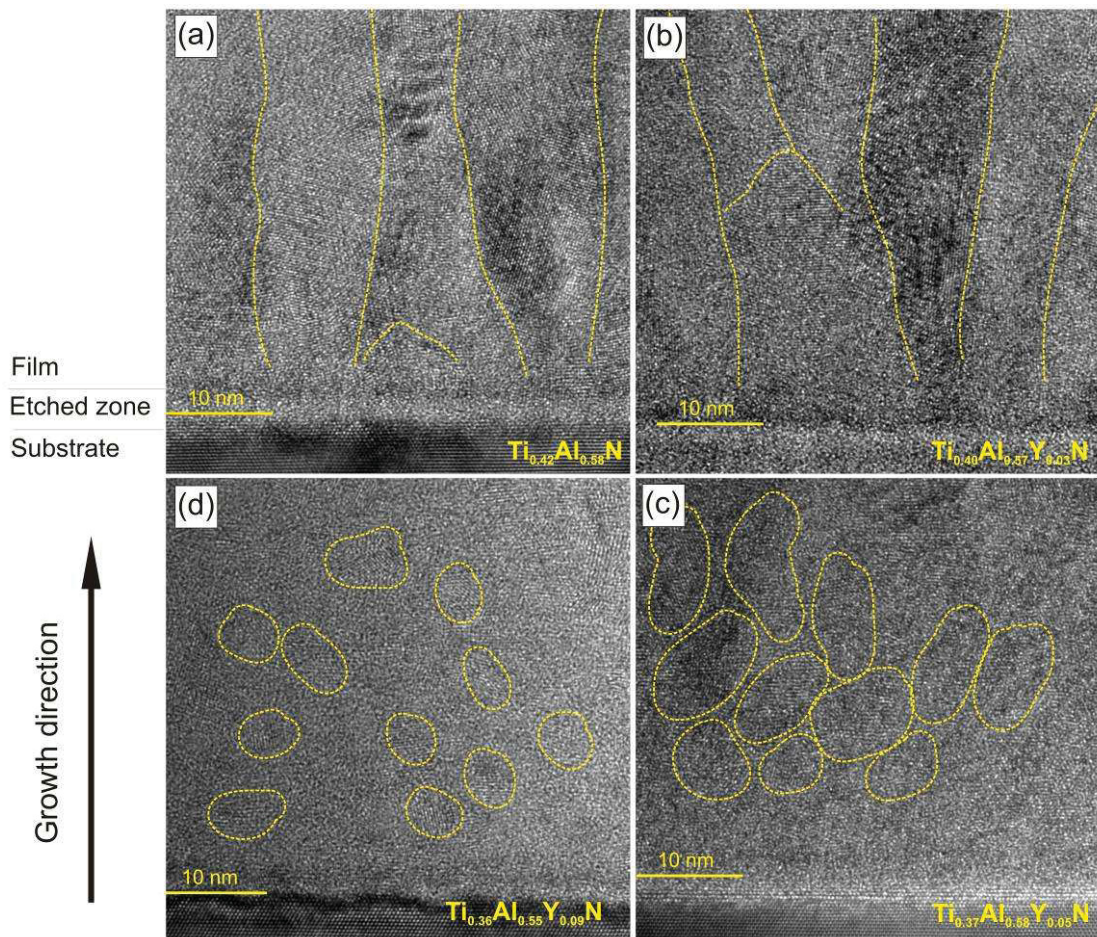
Figure 6.5: Cross-sectional HR-TEM images of the interface region of as-deposited $(Ti_{1-x}Al_x)_{1-z}Y_zN$ with 0 at.% (a), 3 at.% (b), 5 at.% (c) and 9 at.% Y (d) in the metal sublattice.

Selected area diffraction from the middle of the film, confirms the microstructural change from a cubic to a mainly hexagonal lattice with increasing Y-amount, as

presented in Figure 6.6. The diffraction patterns indicate hexagonal crystals with a preferred orientation, and only traces of cubic structure for $Ti_{0.37}Al_{0.58}Y_{0.05}N$. The dashed lines refer to a cubic $Ti_{0.5}Al_{0.5}N$ solid solution crystal, whereas the dash-dotted lines to a hexagonal $Ti_{0.5}Al_{0.5}N$ crystal, respectively. The observations correspond very well to the observed XRD-peaks detected in Bragg-Brentano geometry.
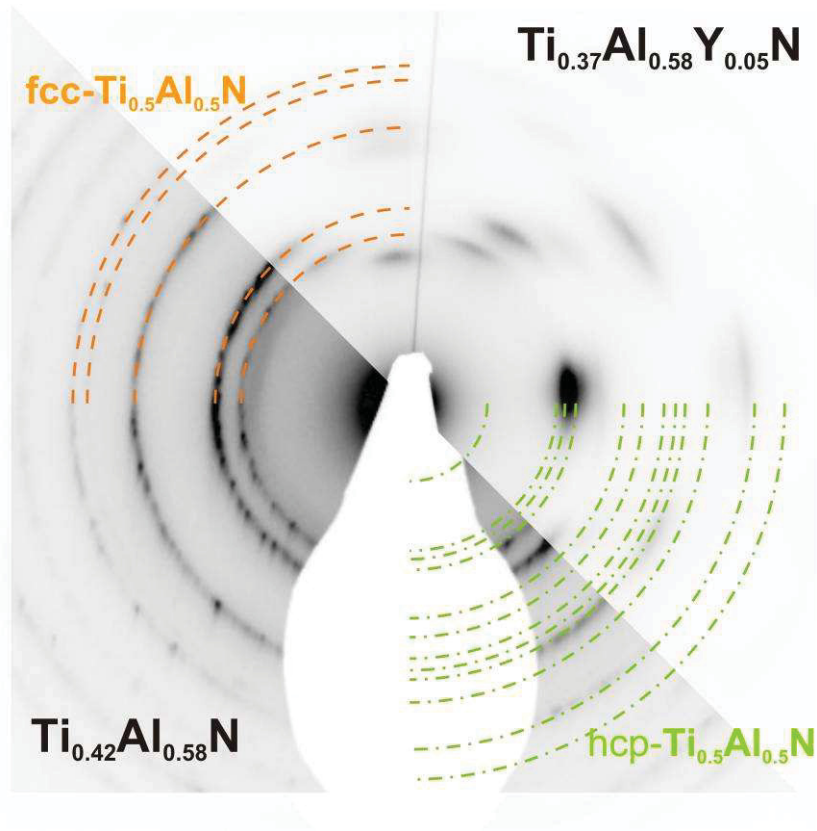
Figure 6.6: SAED patterns of as-deposited $(Ti_{1-x}Al_x)_{1-z}Y_zN$ with z = 0 at.% and 5 at.% Y.

The mentioned structural development can be observed by cross-sectional HR-TEM images and the dedicated SAED pattern taken from the middle of the film, given in Figure 6.7. While for the coating without Y, the cubic lattice is predominant and the orientation of the growing columns is random, the occurring grain refinement, as well as the strong orientation towards the surface increases with increasing Y-amount in the target. Thus, the diffraction rings, in Figure 6.7 (a,b) shrink to dots with a six or two fold geometry, shown in Figure 6.7 (c,d).
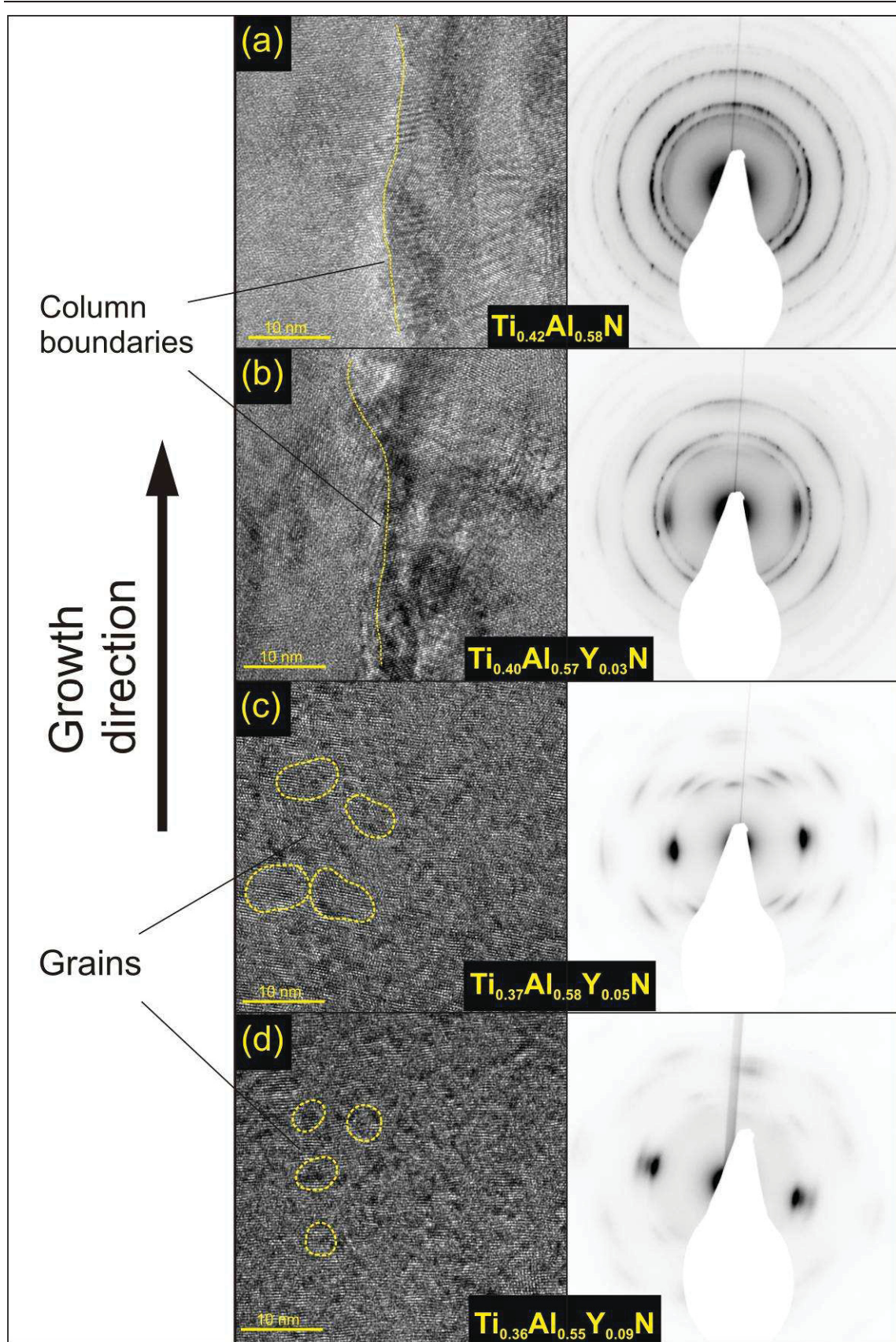
Figure 6.7: Cross-sectional HR-TEM images and corresponding SAED patterns of as-deposited (Ti$_{1-x}$Al$_x$)$_{1-z}$Y$_z$N-thin films with 0 at.% (a), 3 at.% (b), 5 at.% (c) and 9 at.% Y (d), in the metal sublattice.

6.3.2 $(Ti_{1-x}Al_x)_{1-z}Nb_zN$-thin films

Employing the Pseudo-Voight method, the domain size for the Nb-containing coatings was determined from the XRD patterns. The calculated mean feature size was ~65 nm for 2 at.% Nb, ~60 nm for 4 at.% Nb and ~40 nm for 8 at.% Nb in the metal sublattice, respectively. TEM investigations in bright field mode, shown in Figure 6.8, correspond very well to the calculated values, and show domain sizes of 45-55 nm for 2 at.% Nb, 50-65 nm for 4 at.% Nb and finally 40-60 nm for 8 at.% Nb in the metal sublattice. The columnar structure is maintained for all Nb-contents, investigated.
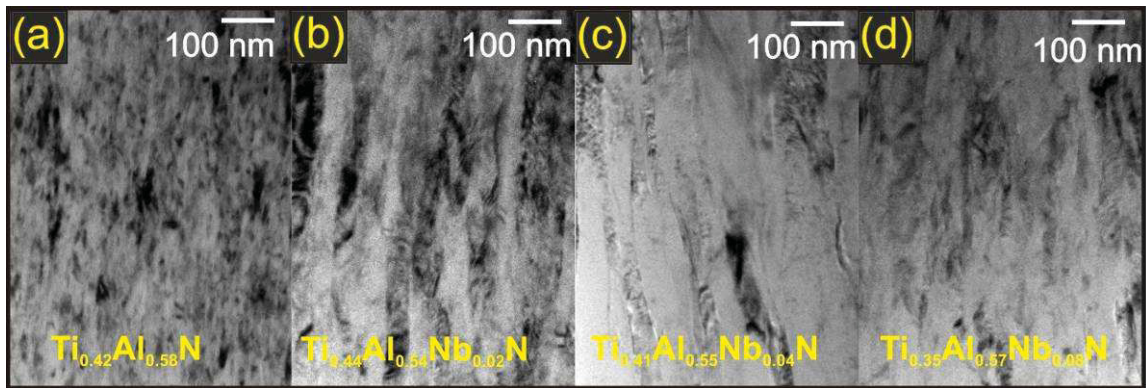
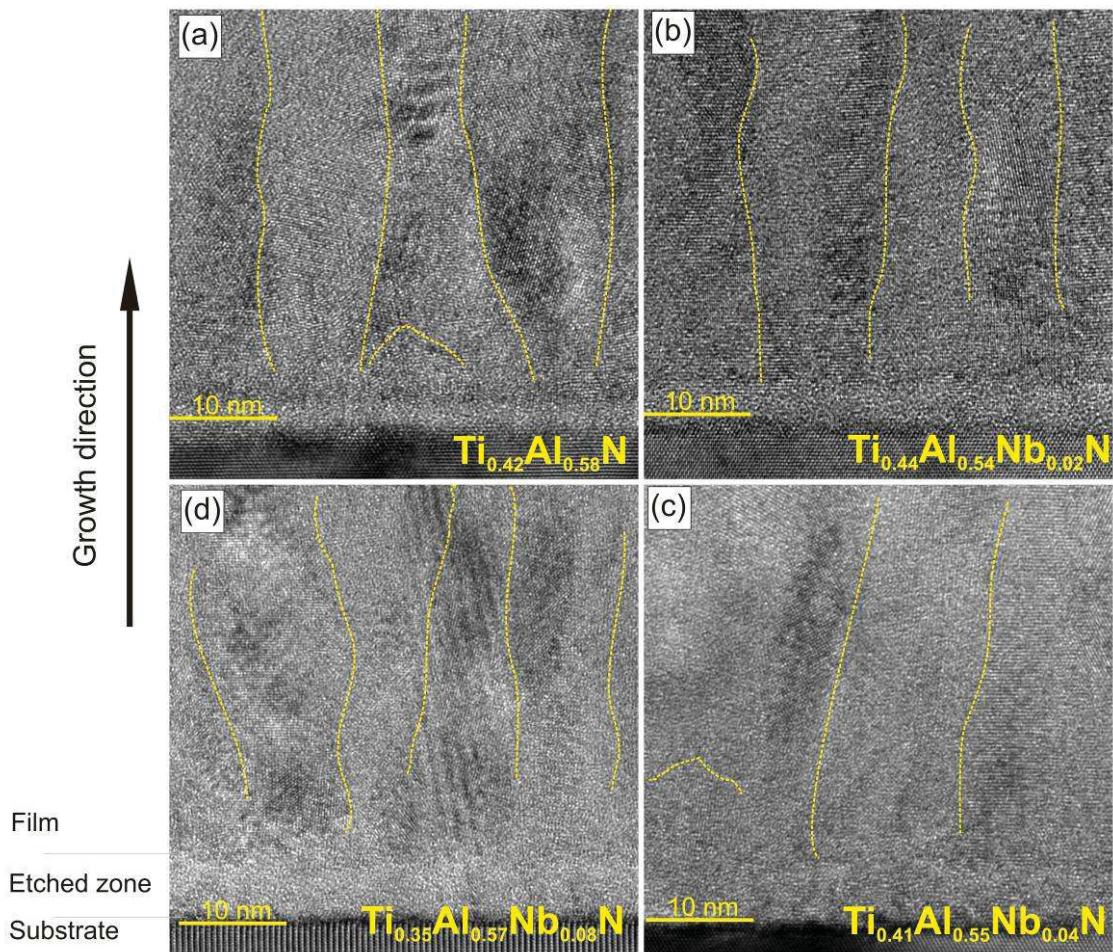**Figure 6.8:** Cross-sectional TEM images of as-deposited $(Ti_{1-x}Al_x)_{1-z}Nb_zN$ with 0 at.% (a), 2 at.% (b), 4 at.% (c) and 8 at.% Nb (d), in the metal sublattice.

As described for the Y-coatings, the amorphous interlayer due to RF-plasma etching prevents the growing film from adopting the orientation and structure of the substrate. Figure 6.9 shows the interfacial region from the coating to the substrate by HR-TEM images.

The $Ti_{0.42}Al_{0.58}N$-coating exhibits a continuously re-nucleated columnar morphology with predominant nuclei at the interface. In principal, this zone-T morphology is maintained for the investigated Nb-containing films. However, already 2 at.% Nb in the target seem to impede the competitive growth and lead to less interruptions of the epitaxial growth of the individual crystallites. Therefore, less re-nucleation occurs during the deposition and a dense columnar structure with much wider columns, as compared to the $Ti_{0.42}Al_{0.58}N$-thin film (20-25 nm), is built up, as presented in Figure 6.9(b-d).

Figure 6.9: Cross-sectional HR-TEM images of the interface region of as-deposited $(Ti_{1-x}Al_x)_{1-z}Nb_zN$ with 0 at.% (a), 2 at.% (b), 4 at.% (c) and 8 at.% Nb (d) in the metal sublattice.

The mean column width increases towards the surface to ~100 nm size compared to the interface of each sample for 2 at.% and 4 at.% Nb-content in the metal sublattice, respectively. This behaviour was not observed for the 8 at.% Nb sample, where the thinner columns keep their average diameter over the entire coating thickness. The cubic structure remains for all of the investigated Nb-contents, as presented in Figure 6.10. The apparent rings in the SAED patterns of the 8 at.% Nb-containing film are slightly narrowed compared to the $Ti_{0.42}Al_{0.58}N$-film. Obviously, the incorporation of the Nb-atoms expands the cubic lattice which leads to smaller diffraction angles and diffraction rings, respectively. This is in good agreement with the XRD results, which propose an enlargement of the cubic lattice parameter with increasing Nb-amount.
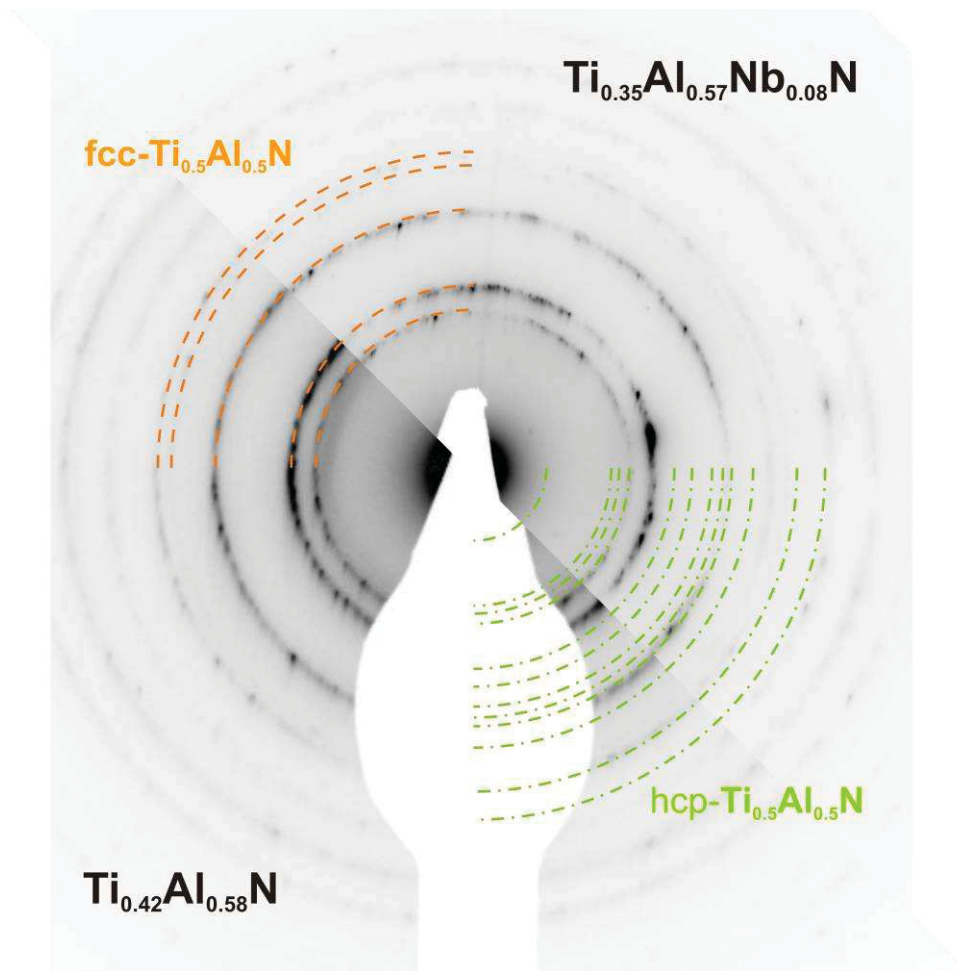
Figure 6.10: SAED patterns of as-deposited $(Ti_{1-x}Al_x)_{1-z}Nb_zN$-thin films with $z = 0$ at.% and 8 at.% Nb.

The $Ti_{0.42}Al_{0.58}N$ film exhibits rings in selected area electron diffraction because of the randomly oriented domains. Investigations of areas with the same size in the $(Ti_{1-x}Al_x)_{1-z}Nb_zN$ coatings, containing 2 at.% and 4 at.% Nb, exhibit spots. This is due to the extensive broadening of the columns in the respective two coatings, only a few columns are enlightened by the electron beam during SAED, thus leading to formation of diffraction spots rather than rings. However, the introduction of 8 at.% Nb exhibits again diffraction rings as a consequence of the before mentioned small column size in that film.

Figure 6.11: Cross-sectional HR-TEM images and corresponding SAED patterns of as-deposited $(Ti_{1-x}Al_x)_{1-z}Nb_zN$-thin films with 0 at.% (a), 2 at.% (b), 4 at.% (c) and 8 at.% Nb (d), in the metal sublattice.

6.4 Mechanical properties
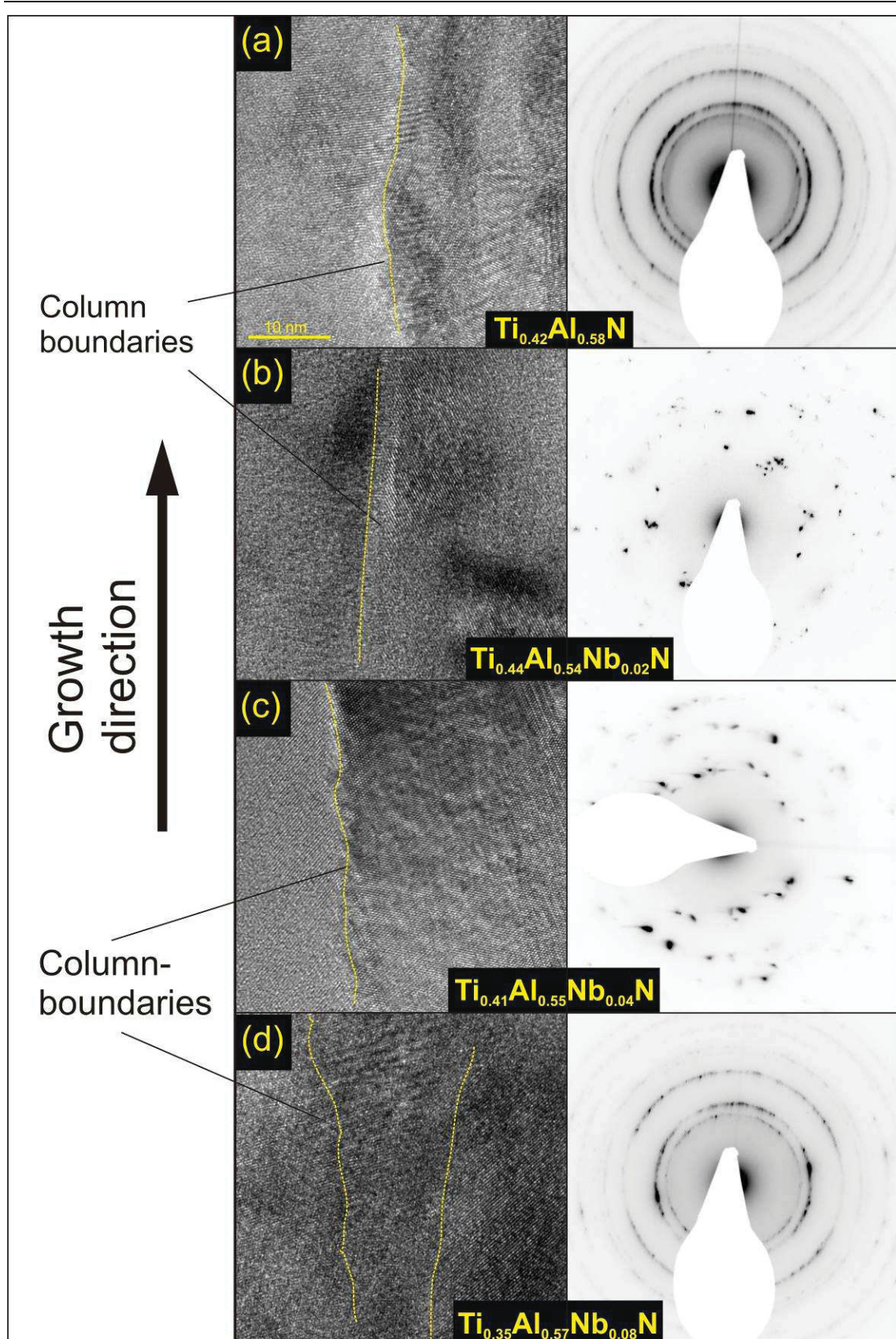
For both coatings a clear tendency in hardness and elastic modulus distribution was found, as presented in Figure 6.12. The Y-containing films exhibit a strong decrease in hardness with increasing Y-amount, whereas the increasing Nb-content results in a strong hardness increase, see Figure 6.12(a) and (b), respectively.

The obtained hardness values for the $(Ti_{1-x}Al_x)_{1-z}Y_zN$-coatings are slightly higher as reported by Moser [78], for similar coatings. The addition of Y to $Ti_{0.42}Al_{0.58}N$, which leads to a structural modification from single-phase cubic, to mixed cubic-hexagonal and finally to almost single-phase hexagonal (with $z = 0.09$), results in a decrease in hardness and elastic modulus. The hardness decreases from 33 GPa to 23 GPa for the $Ti_{0.42}Al_{0.58}N$- and the $Ti_{0.36}Al_{0.55}Y_{0.09}N$-films, respectively. This can be explained by the lower mechanical properties and elastic constants of the hexagonal phase as compared to the cubic phase [83].

The addition of niobium induces a strengthening of the as-deposited coatings. Due to the maintained cubic structure, the incorporation of Nb-atoms in the fcc-Ti-Al-N lattice changes the bonding state and therefore also the elastic constant increases. With the incorporation of Nb to $Ti_{0.42}Al_{0.58}N$ an increase in hardness from 33 GPa to 40 GPa for 8 at.% in the metal sublattice can be measured.
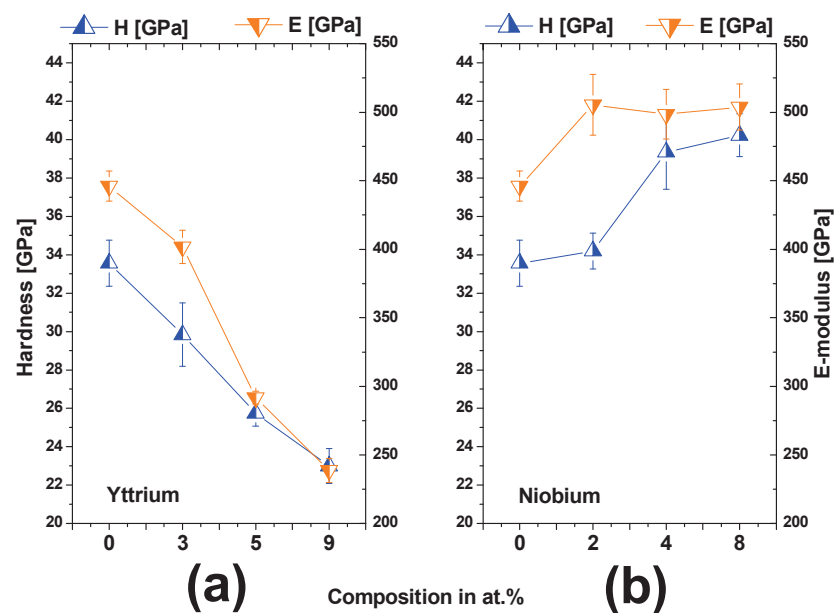
**Figure 6.12:** Hardness and elastic modulus of as-deposited $(Ti_{1-x}Al_x)_{1-z}Y_zN$ (a), and $(Ti_{1-x}Al_x)_{1-z}Nb_zN$ (b), as a function of the respective alloying element content in the metal sublattice.

6.5 Thermal stability

The annealing experiments on the Y- or Nb-alloyed $Ti_{1-x}Al_xN$-systems included in situ high-temperature X-ray diffraction (HT-XRD) and simultaneous thermal analysis (STA). The annealing curve for the HT-XRD measurements is presented in Figure 6.13.

The HT-XRD samples were annealed for ~20 hours, as shown below in Figure 6.13. Each XRD-run is marked as red line and was obtained in an angular range from 30° to 90°. Each sample was measured in the as-deposited state at room temperature, before the first heating step to 500 °C was applied. Then, the temperature was raised after each XRD-run with 20 K/min up to 1100 °C (blue dashed line), where two measurements were obtained. For the adjacent cooling step (green solid line), 30 K/min were chosen.
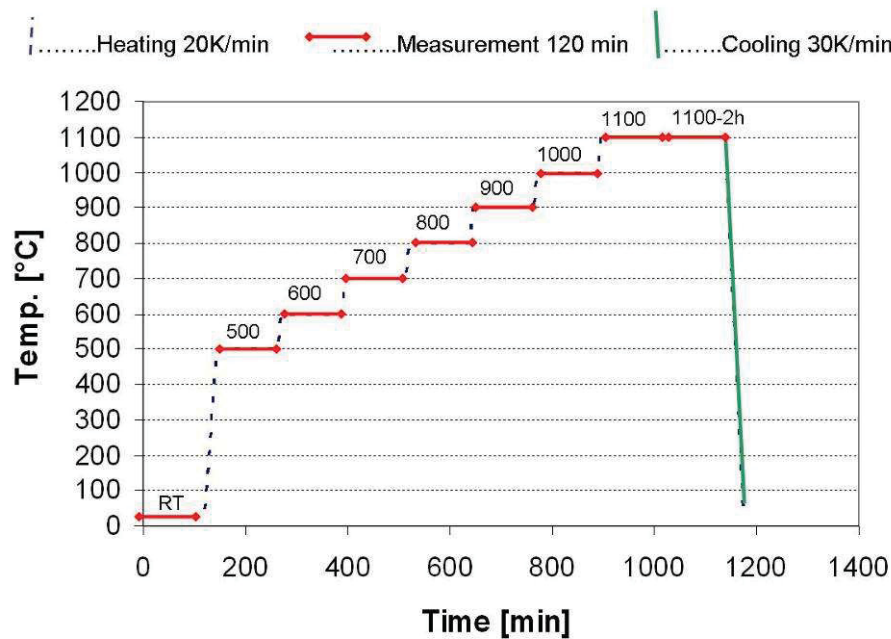
Figure 6.13: Annealing procedure of the in-situ HT-XRD measurements.

The full range of obtained HT-XRD patterns for $Ti_{0.42}Al_{0.58}N$ is presented in Figure 6.14. Generally, for the discussion of the HT-XRD analysis of the Y- and Nb-containing films, the pattern of 600 °C and 700 °C are not shown, as no visible reactions take place. Significant peaks for the interpretation are labeled on top of the respective peak, where fcc-TiN and hcp-AlN are abbreviated with c-TiN and h-AlN, respectively. For the evaluation of the HT-XRD, starting with 500 °C, it is important to determine the

temperature induced peak shift, which could result in misleading interpretation if the occurring peaks would be directly compared to room temperature.

Therefore, the orange, solid line from the triangle marks the Al_2O_3-$K_{\alpha1}$-peak at room-temperature. The mismatch of the (110)- and the (220)-Al_3O_2-reflexes at 1100 °C, are ~0.3° and ~1°, respectively.
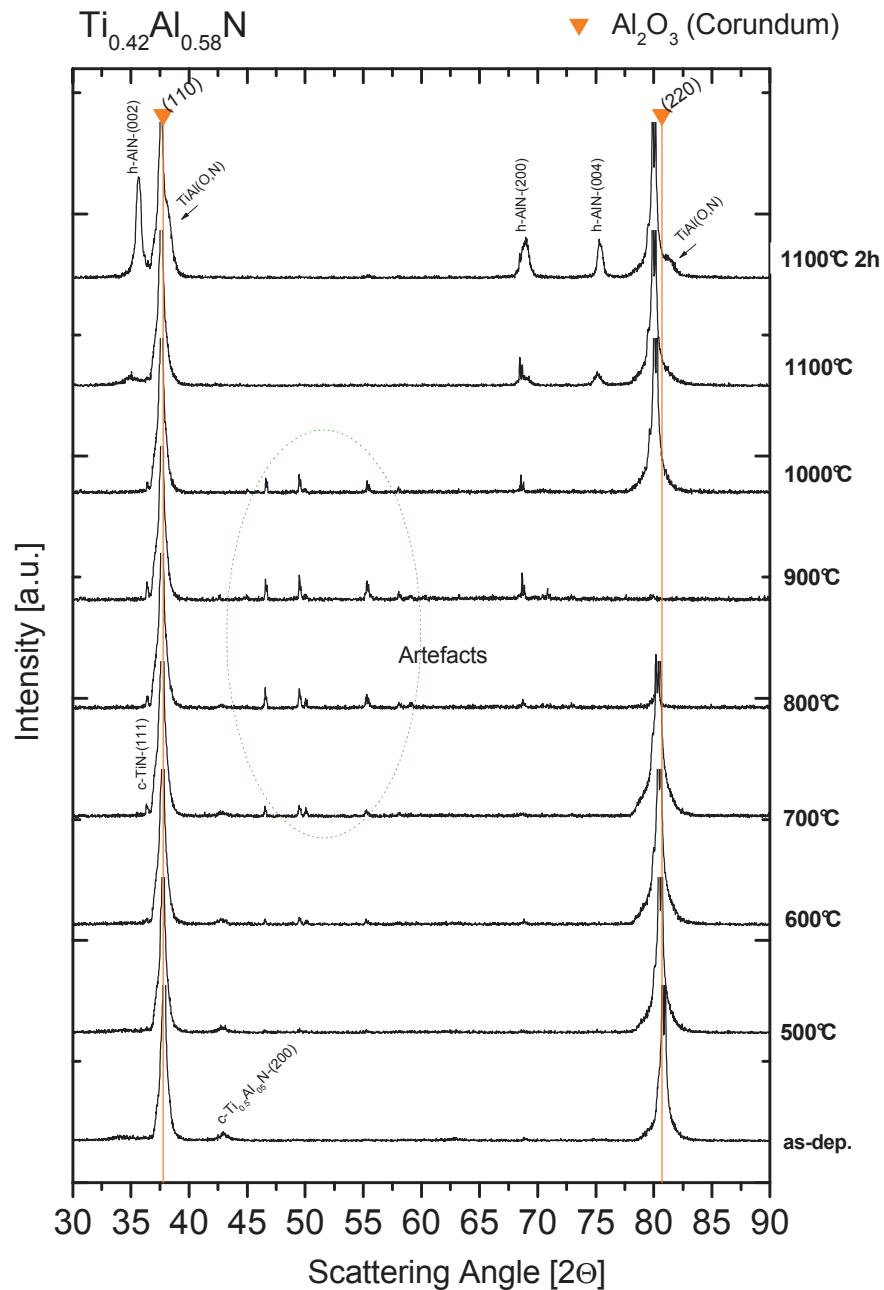
Figure 6.14: In-situ HT-XRD patterns of the $Ti_{0.42}Al_{0.58}N$-thin film.

As discussed in chapter 6.2, the $Ti_{0.42}Al_{0.58}N$ film has a single phase cubic structure in the as-deposited state. Up to approximately 900 °C, the intensity of the (200)-reflex of the fcc-$Ti_{0.5}Al_{0.5}N$ decreases continuously, while the fcc-TiN-(111)-reflex emerges slightly. Already before 800 °C, spinodal decomposition occurs, where fcc-AlN can be detected next to the cubic Ti-Al-N matrix. The appearance of hexagonal AlN marks the transformation of fcc-AlN into hcp-AlN, which is growing at the expense of the former cubic matrix. However at about 1100 °C, a shoulder arises at the right side of the substrate peaks. This development is caused by an interfacial reaction, which involves the Al_2O_3-substrate, and will be explained later. The second XRD-pattern at 1100 °C presents a clear increase in intensity of this shoulder and a coarsened microstructure, as indicated by the more intense and sharper peaks.

### 6.5.1 $(Ti_{1-x}Al_x)_{1-z}Y_zN$-thin films

The Y-containing films were annealed and investigated in the same way as explained above. However, no structural changes are observeable in the HT-XRD patterns, therefore up to ~800 °C, only scans of the higher temperature region are shown. For the films containing 3 at.% and the 9 at.% Y in the metal sublattice, the annealed samples were additionally investigated by TEM and HR-TEM.

✓   **$Ti_{0.40}Al_{0.57}Y_{0.03}N$:**

For the $Ti_{0.40}Al_{0.57}Y_{0.03}N$-thin film, as presented in Figure 6.15, the determined amount of hcp-TiAlN phase in the as-deposited state by the HT-XRD, is in good agreement with the results from the XRD-measurements of the powdered sample. As already shown for the $Ti_{0.42}Al_{0.58}N$-film, decreasing intensities of the fcc-$Ti_{0.5}Al_{0.5}N$-reflexes coincide with increasing hcp-AlN reflexes, as apparent for higher temperatures. Increased temperature leads to a decomposition of the cubic TiAlN solid solution. At 800 °C reflexes appear of ~39.8 deg. and ~85.5 deg. These reflexes are assumed to be a hexagonal solid-solution AlTiN-phase, which is built as intermediate step in the formation process to hexagonal AlN. The detected reflexes increase in intensity at 900 °C and are no longer observed at 1000 °C.

Thus, for the $Ti_{0.40}Al_{0.57}Y_{0.03}N$ film, a retarded decomposition over an intermediate step and phase transformation from fcc-AlN to hcp-AlN can be observed. A small amount of fcc-TiN stabilizes at ~1100 °C, while the main structure is hexagonal. Further,

decomposition and grain coarsening will still go on at this temperature. At 1100°C, moreover the formerly mentioned reflexes next to the substrate-peaks emerge clearly at longer annealing times.
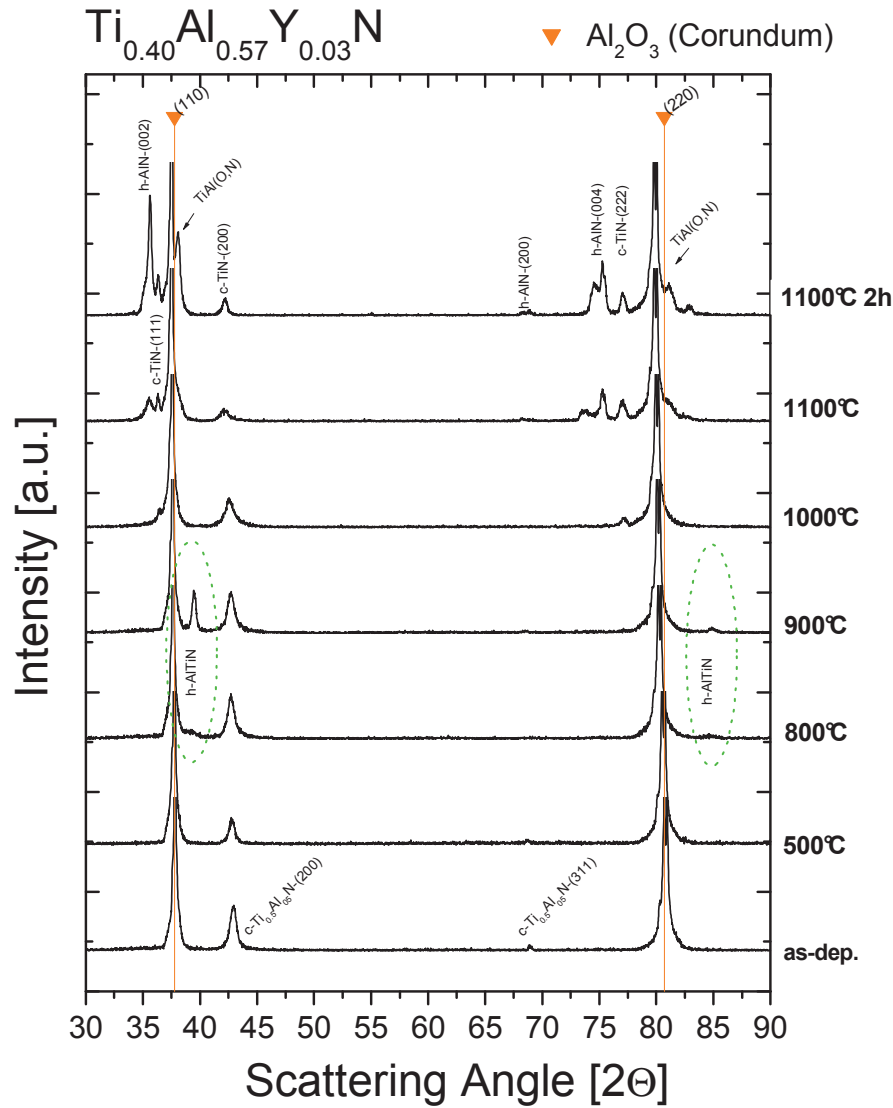
Figure 6.15: In-situ HT-XRD patterns of the $Ti_{0.40}Al_{0.57}Y_{0.03}N$-thin film.

A bright field cross-section TEM-image, taken from the middle of the sample after the HT-XRD measurement, presented in Figure 6.16(a), expresses grains with an average diameter of 20-50 nm. Hence, it can be assumed that annealing up to 1100 °C induced decomposition and recrystallization. The corresponding SAED-patterns present a clear separation into fcc-TiN and hcp-AlN.
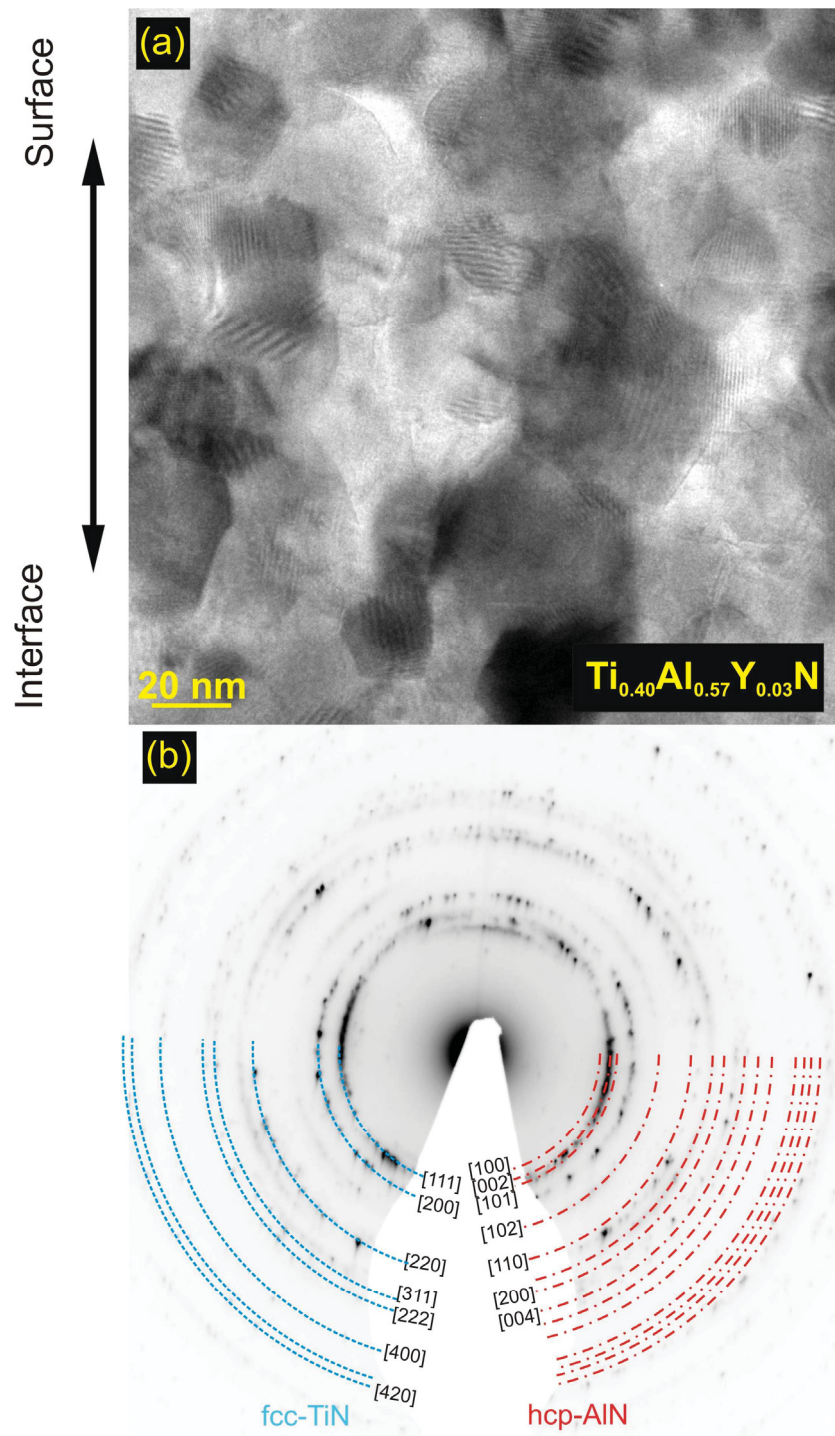
Figure 6.16: (a) Cross-sectional HR-TEM-image and (b) corresponding SAED-pattern taken from the middle of the $Ti_{0.40}Al_{0.57}Y_{0.03}N$-thin film after the in-situ HT-XRD-measurements.

✓ **$Ti_{0.37}Al_{0.58}Y_{0.05}N$:**

The incorporation of 5 at.% Y in the $Ti_{1-x}Al_xN$ metal sublattice, results in a hexagonal microstructure in the as-deposited state, as shown in Figure 6.17. At room temperature, fcc-$Ti_{0.5}Al_{0.5}N$-reflexes are detected in addition to the broad hcp-$Ti_{0.5}Al_{0.5}N$-(002) peak. This hexagonal dominated solid solution structure remains stable up to ~800 °C. At 900 °C, the hcp-$Ti_{0.5}Al_{0.5}N$-(002) reflex vanishes, while the hcp-AlN-(200) peak appears. Therefore, the decomposition can be assumed to occur between the two temperatures. Above 1000 °C, (002)- and (004)-reflexes of hcp-AlN appear and increase in intensity, suggesting that recrystallization and grain growth continues.
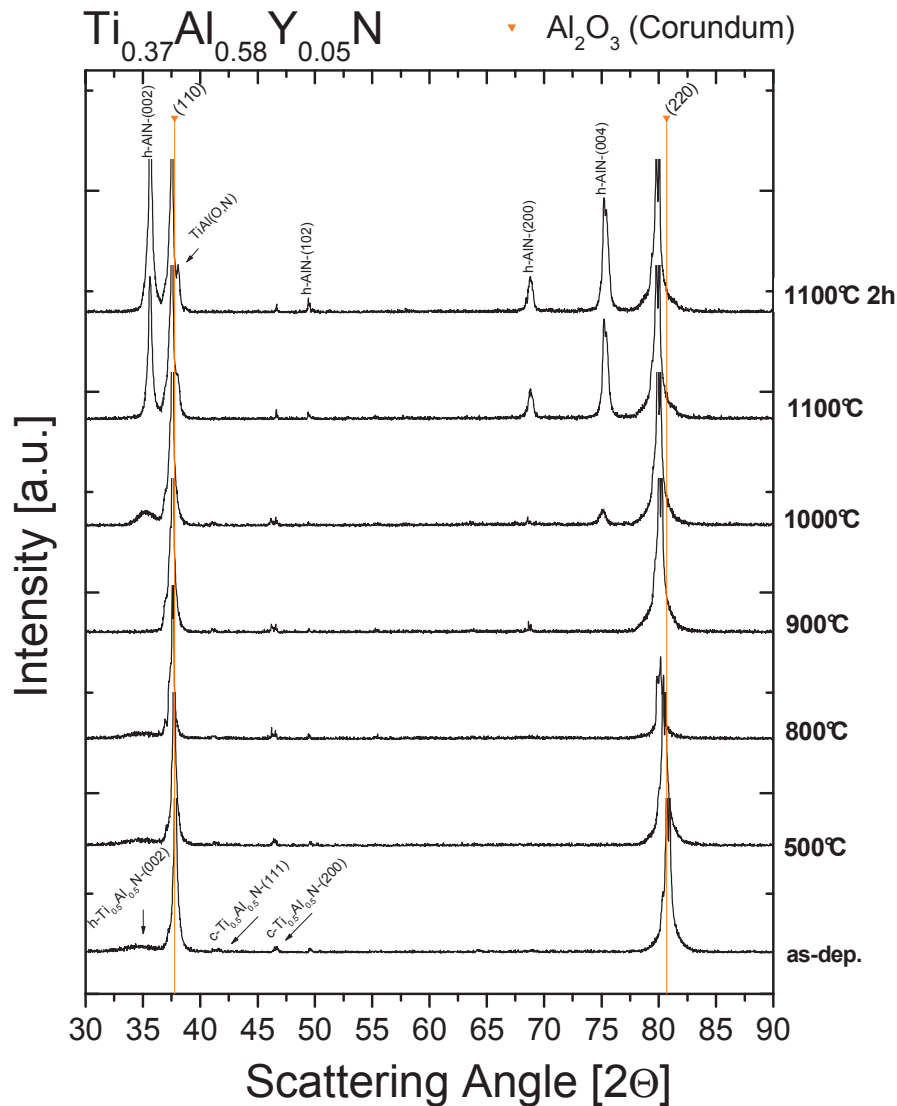
Figure 6.17: In-situ HT-XRD patterns of the $Ti_{0.37}Al_{0.58}Y_{0.05}N$-thin film.

✓ **$Ti_{0.36}Al_{0.55}Y_{0.09}N$:**

During the HT-XRD measurements of the $Ti_{0.36}Al_{0.55}Y_{0.09}N$, as shown in Figure 6.18, the single phase hexagonal structure from the as-deposited state decomposes as follows:

The hcp-$Ti_{0.5}Al_{0.5}N$-(100)-reflex decreases steadily in intensity with increasing temperatures, while already at 500 °C hcp-AlN and fcc-TiN reflexes can be detected. Thus, the supersatured solid solution in as-deposited state starts at comparably low temperatures to decompose. This decomposition is observable through the appearance of hcp-AlN reflexes at 800 °C and fcc-TiN-(111) phases from temperatures of 500 °C and higher. Unfortunately, the angles above ~70 degrees were not counted for the temperatures from 800 °C up to 1100 °C because of unknown reasons.

At 1100 °C, the fcc-TiN-(002) reflex appears, resulting in a hexagonally dominated structure. Additionally, at an annealing time of 2 hours at 1100 °C, a cubic YN-reflex arises. The formation of this phase was not observed for the coatings, containing 3 at.% Y and 5 at.% Y in the metal sublattice, respectively.
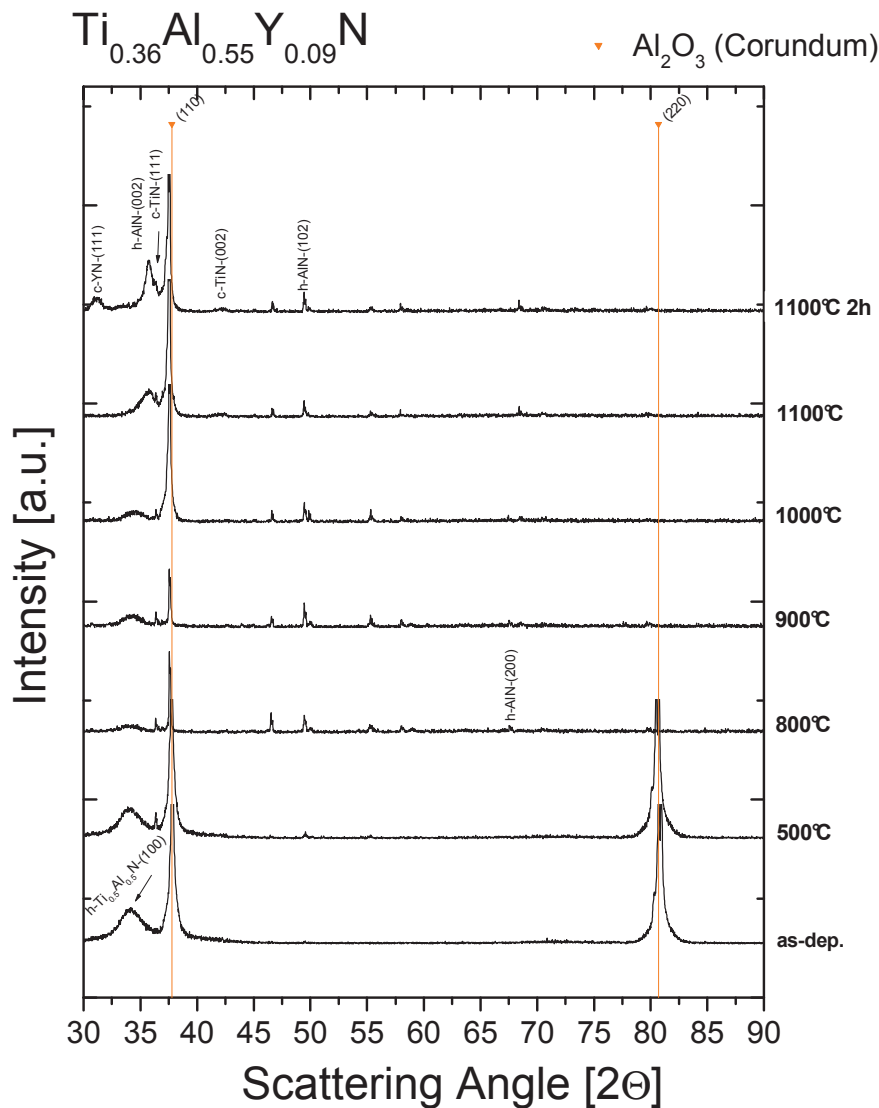
Figure 6.18: In-situ HT-XRD patterns of the $Ti_{0.36}Al_{0.55}Y_{0.09}N$-thin film.

After the in-situ HT-XRD measurements, TEM-investigations were done on the annealed samples and cross-sectional images and SAED-pattern taken, as shown in Figure 6.19(a). The polycrystalline structure incorporates grains, with an average size of ~20 nm, but also larger grains are visible, proposing that recrystallization already started. The SAED-patterns taken from the middle of the film, Figure 6.19(b), yield strong cubic and hexagonal reflexes, which correspond to the findings of the HT-XRD investigations. Due to the appearing dots instead of rings as in the coating, containing 3

at.% Y in the metal sublattice, a preferential grain orientation is visible. Moreover, fcc-YN can be detected by SAED.
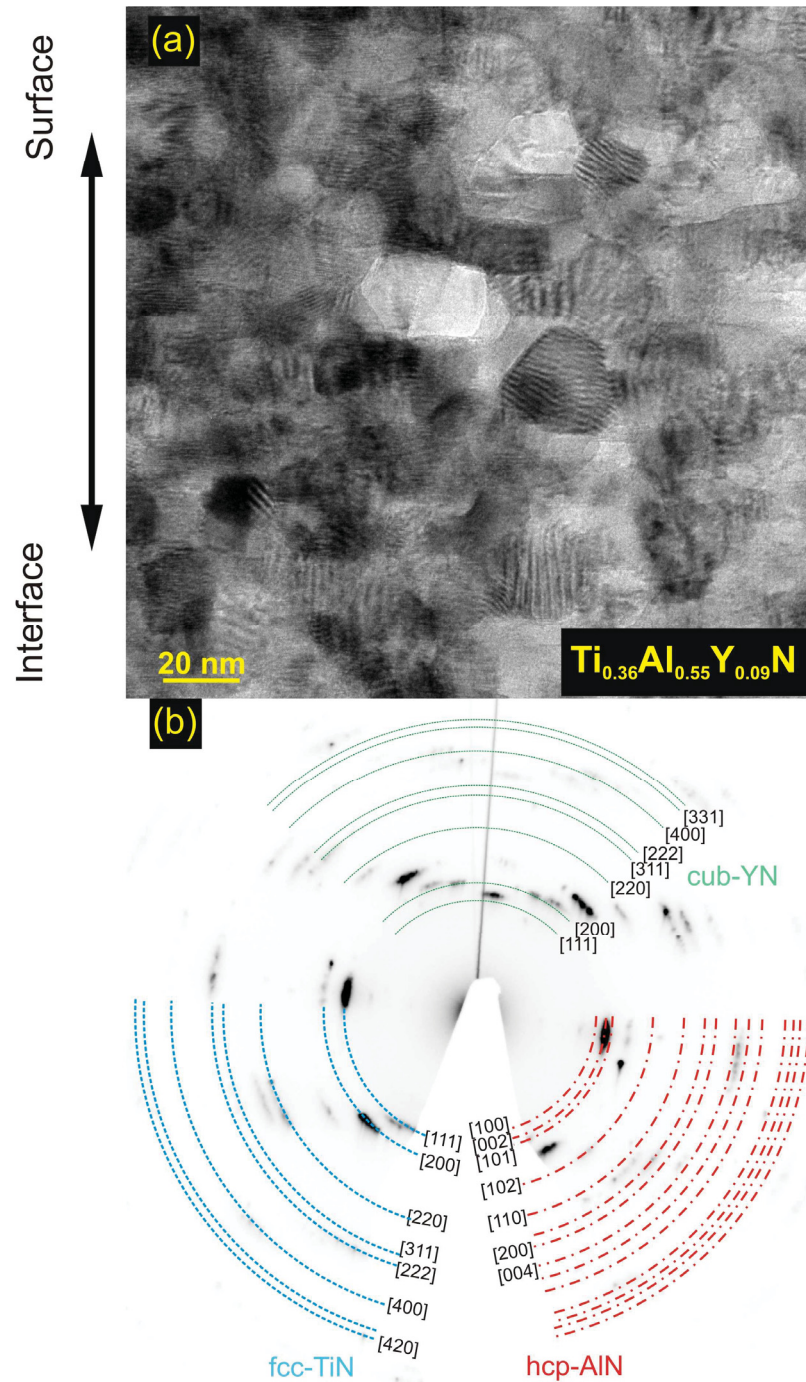
Figure 6.19: (a) Cross-sectional HR-TEM-image and (b) corresponding SAED-pattern taken from the middle of the $Ti_{0.36}Al_{0.55}Y_{0.09}N$-thin film after the in-situ HT-XRD-measurements.

For comparison between the $(Ti_{1-x}Al_x)_{1-z}Y_zN$-coatings, the HT-XRD samples were investigated with XRD at room temperature as well. Thus the temperature induced

peak-shift, for the samples on sapphire was excluded. Furthermore, it provides detailed information at different annealing conditions and its influence.

After HT-XRD annealing, all samples exhibit a hexagonal dominated structure, as presented in Figure 6.20. In the as-deposited state, increasing Y-content leads to a shift from a single phase cubic structure, over a binary phase regime, to an almost single phase hexagonal structure, as presented in Figure 6.2. Independent of the Y-amounts, all films exhibit a two phase regime, consisting of fcc-TiN and hcp-AlN after annealing. Additionally, fcc-YN can be detected for the $Ti_{0.36}Al_{0.55}Y_{0.09}N$ coating. The hcp-AlN-peaks are slightly shifted towards lower angles, which can be explained by residual Ti- or Y-atoms in solid-solution. The appearance of residual reflexes near the hcp-$Ti_{0.5}Al_{0.5}N$-reflex at ~34°, suggest that the decomposition into fcc-TiN, hcp-AlN and fcc-YN is not fully completed after the HT-XRD measurements to 1100 °C.
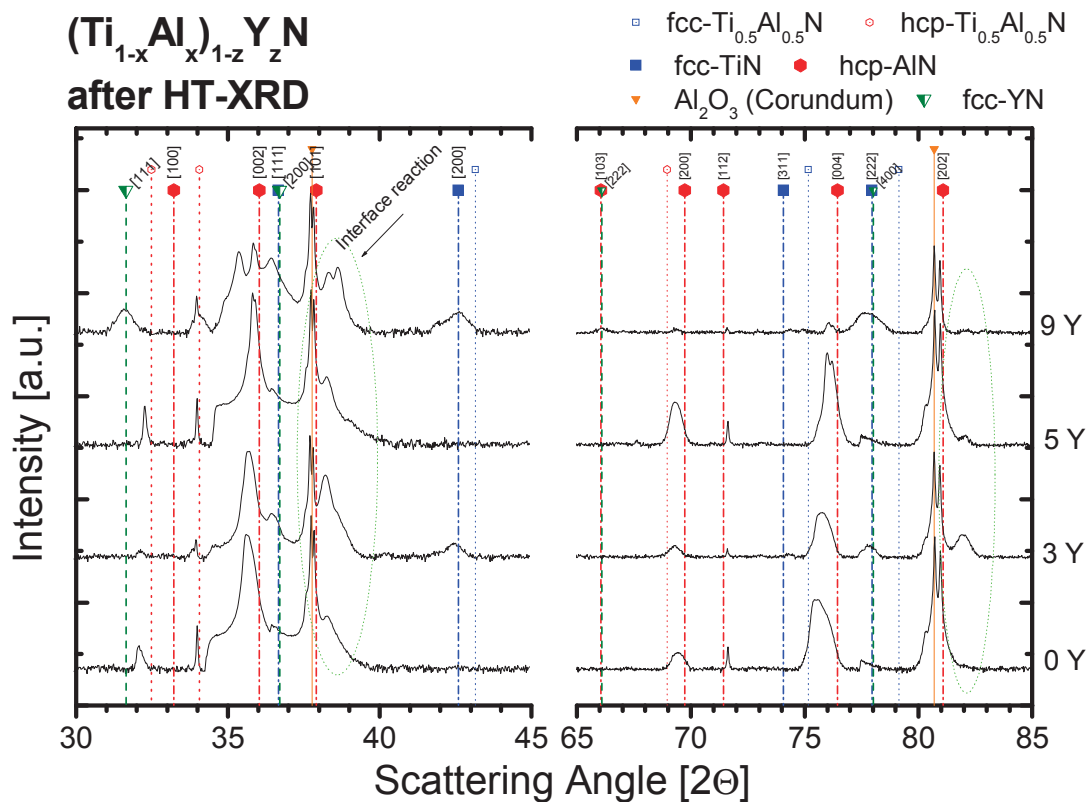
Figure 6.20: XRD-patterns of the $(Ti_{1-x}Al_x)_{1-z}Y_zN$-films after in-situ HT-XRD measurements.

For all compositions investigated, additional reflexes at ~38.4 and ~82.0 degree appear, which are indicated within the dotted lines in Figure 6.20. As presented in Figure 6.21(a), the interface between the $Ti_{0.40}Al_{0.57}Y_{0.03}N$-film and the substrate is perturbed by larger grains. These grains, which were not observed in the as-deposited state, are built through an interfacial reaction between substrate and film during the HT-XRD annealing. Therefore, the development of grains, reaching an average depth of ~100 nm, results in additional reflexes in the XRD pattern, as mentioned above. The corresponding reflexes are indicated as TiAl(O,N) because no distinct phase determination was possible. Because of their small atom size, it can be assumed, that mainly N- and O-atoms are responsible for the formation of the new crystals at the interface, but also Al- and Ti-atoms diffuse effectively at the given temperatures and times of the annealing process. The area within the dashed rectangle in Figure 6.21(a) is presented in Figure 6.21(b) with higher magnification and exhibits the small grains of fcc-TiN and hcp-AlN on top, as well as the substrate-film compound crystals at the bottom.
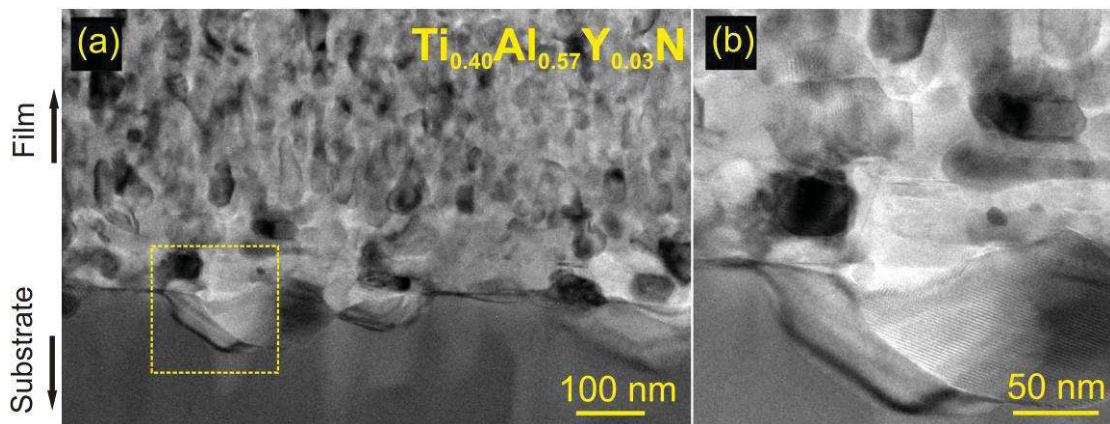
Figure 6.21: (a) Cross-sectional HR-TEM images of the $Ti_{0.40}Al_{0.57}Y_{0.03}N$ thin film-substrate interface, and (b) a higher magnification detail, after the HT-XRD-annealing procedure to 1100 °C.

The structural development in the middle part of the HT-XRD-annealed $(Ti_{1-x}Al_x)_{1-z}Y_zN$-coatings is presented in Figure 6.22. As it was suggested by the HT-XRD measurements, large fcc-TiN crystals remain in a commonly hexagonal matrix after annealing, as shown in Figure 6.22(a). The Y-induced grain refinement, which occurred already during deposition, is responsible for numerous re-nucleation sites during the annealing process. Thus, an average grain size of 40-60 nm and ~20 nm was observed for $Ti_{0.40}Al_{0.57}Y_{0.03}N$ and $Ti_{0.36}Al_{0.55}Y_{0.09}N$, presented in 6.20(b) and (c), respectively.
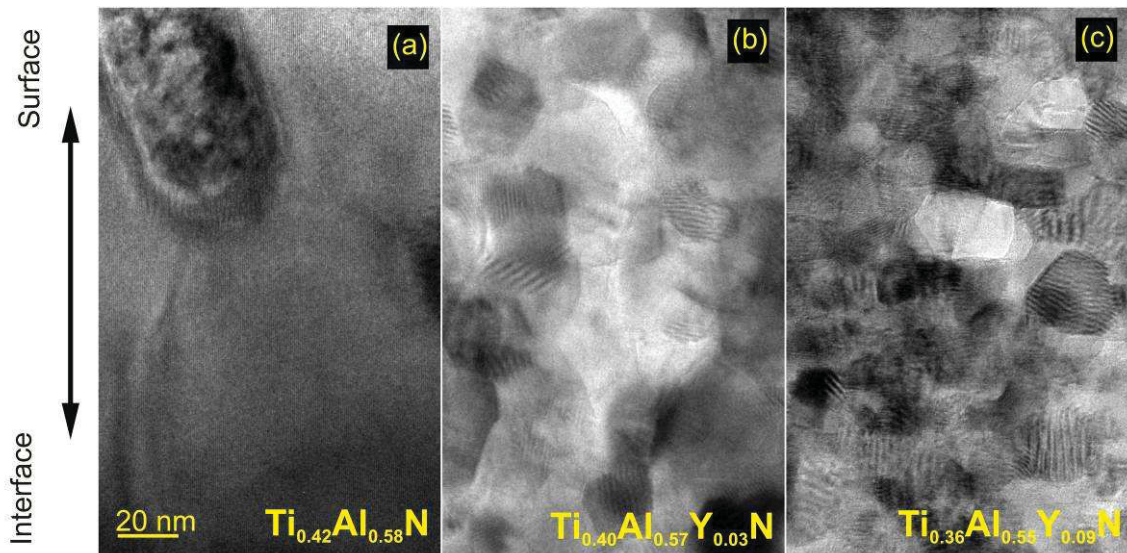
Figure 6.22: Cross-sectional HR-TEM-images of the $(Ti_{1-x}Al_x)_{1-z}Y_zN$-thin films, containing 0 at.% (a), 3 at.% (b) and 9 at.% Y (c) in the metal sublattice, taken from the middle of the films after the HT-XRD annealing procedure.

The STA-results of the $(Ti_{1-x}Al_x)_{1-z}Y_zN$-coatings, are given in Figure 6.23. As already proposed by the in-situ XRD-measurements, the $(Ti_{1-x}Al_x)_{1-z}Y_zN$-films start to restructure by recovery at ~500 °C. The first exothermic increase of heat flow can therefore be limited to this process. The baseline $Ti_{1-x}Al_xN$-coating exhibits exothermic heat flow peaks, which indicate the spinodal decomposition to fcc-AlN and fcc-TiN phases at ~870 °C. Recrystallization and growth of the thermodynamically stable phases fcc-TiN and hcp-AlN is assumed to occur at temperatures higher than 1000 °C.

Moreover, for the $(Ti_{1-x}Al_x)_{1-z}Y_zN$ with 3 at.% and 9 at.% yttrium, the retarded peak maxima between 1100 °C and 1200 °C are in good correlation with the in-situ XRD-patterns, proposing that the decomposition and recrystallization reaction is not finished at 1100 °C. The weight loss, with an onset-temperature of approximately 1200 °C, can be related to the nitrogen-loss of the slightly over-stoichiometric coatings.
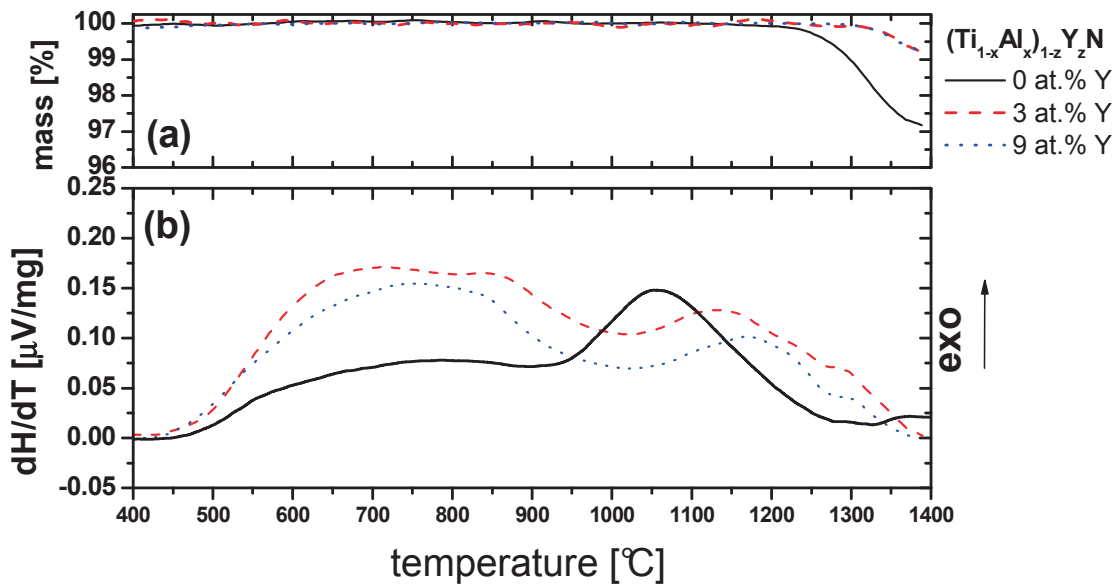
Figure 6.23: (a) TGA- and (b) DSC-curves of the $(Ti_{1-x}Al_x)_{1-z}Y_zN$-thin films, during annealing to 1400 °C.

In contrast to the XRD patterns, taken after in-situ HT-XRD samples, the XRD-measurements on powder after the STA-investigations, given in Figure 6.24, exhibit completely decomposed phases, where the individual reflexes correctly match the fcc-TiN, hcp-AlN and fcc-YN positions. After the two annealing steps up to 1400 °C, only hcp-AlN and fcc-TiN are observed in the $Ti_{0.42}Al_{0.58}N$-powder. The addition of yttrium results in no structural changes for the $Ti_{0.40}Al_{0.57}Y_{0.03}N$-film, compared to the $Ti_{0.42}Al_{0.58}N$-thin film, but results in the additional formation of fcc-YN precipitates in the $Ti_{0.37}Al_{0.58}Y_{0.05}N$ and $Ti_{0.36}Al_{0.55}Y_{0.09}N$ coatings, respectively.
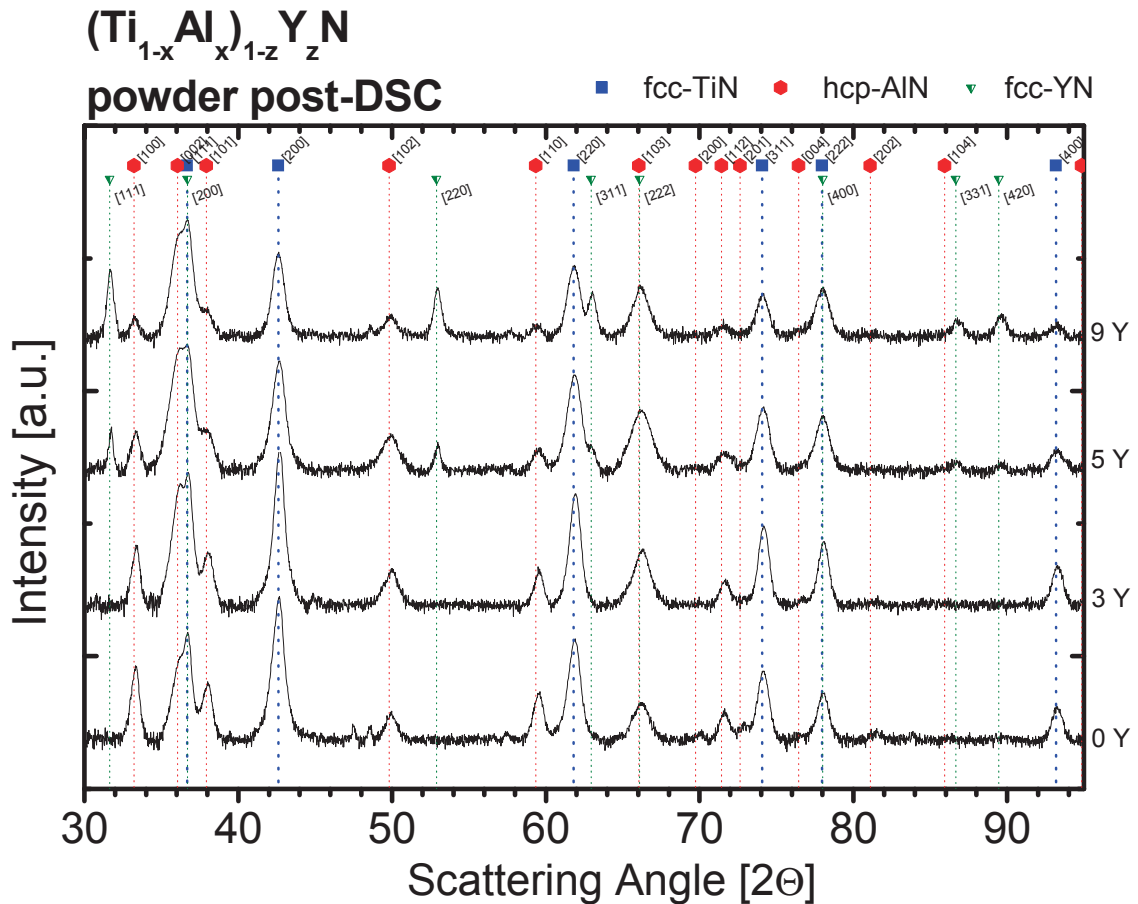
Figure 6.24: XRD-patterns of $(Ti_{1-x}Al_x)_{1-z}Y_zN$-powder samples, with 0 at.%, 3 at.%, 5 at.% and 9 at.% Y in the metal sublattice, after STA to 1400 °C.

6.5.2 $(Ti_{1-x}Al_x)_{1-z}Nb_zN$-thin films

The same experiments and processing routines as for the Y-containing films were applied for the Nb-alloyed $Ti_{1-x}Al_xN$ films. As already mentioned, with increasing Nb-content no structural change from cubic to hexagonal can be detected. Further, no structural changes are observable in the temperature range between 500 °C and 800 °C. These HT-XRD-patterns are therefore not shown in the following discussion.

✓ **$Ti_{0.44}Al_{0.54}Nb_{0.02}N$:**

As already presented in Figure 6.3, the as-deposited $Ti_{0.44}Al_{0.54}Nb_{0.02}N$ film has a single-phase cubic microstructure. Upon annealing to ~800 °C, as shown in Figure 6.25, the reflex intensities of the solid solution cubic domains decrease. While hcp-AlN is already formed at 900 °C, the fcc-TiN-(111) reflex can only be detected at 1000 °C.

Due to the measurement procedure this structural development seems to be only temperature dependent, however it can be assumed, that both reactions start simultaneously. Further annealing leads to hexagonal domination of the structure. The incorporation of the Nb-atoms is still undertaken by the cubic phase, namely fcc-TiN, which is slightly shifted towards lower angles. At 1100 °C, additional reflexes appear next to the substrate reflexes, which are related to a substrate-film reaction as explained in section 6.5.1.
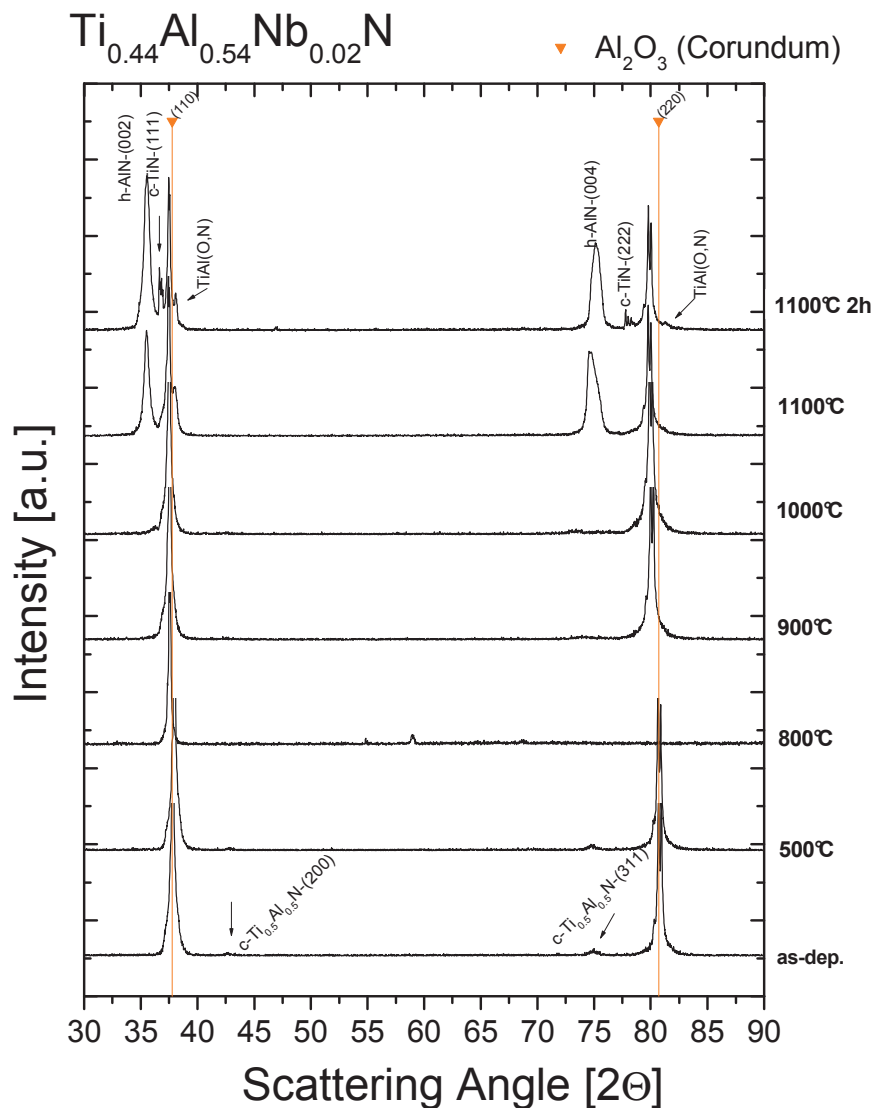
Figure 6.25: In-situ HT-XRD patterns of the $Ti_{0.44}Al_{0.54}Nb_{0.02}N$-thin film.

High-resolution TEM-investigations of the interface-region of the coating, after the HT-XRD measurement to 1100 °C, exhibit almost completely coherent hexagonal structure for the substrate and the residual film. The amorphous interlayer, which was observed in the as-deposited state, is not visible after HT-XRD annealing and has fully evolved into the hexagonal structure of the substrate, as shown in Figure 6.26(a). Additionally, similar grains at the interface, as observed for the $(Ti_{1-x}Al_x)_{1-z}Y_zN$ films were also found in the Nb-containing coatings. The corresponding SAED-pattern, as presented in Figure 6.26(b), reveals the small difference in lattice parameters of the Al_2O_3-substrate and the hcp-AlN, resulting in double diffraction spots. Therefore misfit dislocations, marked in the HR-TEM-image, are generated to reduce the occurring strains.
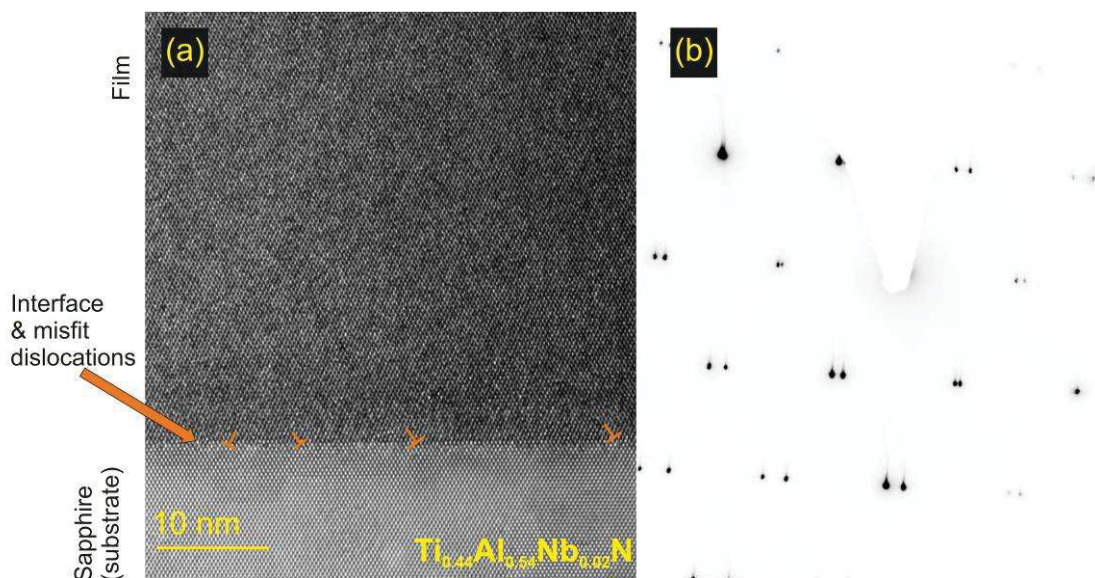
Figure 6.26: (a) Cross-sectional HR-TEM image of the $Ti_{0.44}Al_{0.54}Nb_{0.02}N$-thin film-substrate interface and (b) corresponding SAED-pattern after the HT-XRD annealing procedure to 1100 °C.

✓ **$Ti_{0.41}Al_{0.55}Nb_{0.04}N$:**

Addition of 4 at.% niobium in the target leads to eminent changes during the in-situ HT-XRD measurements of the $Ti_{0.41}Al_{0.55}Nb_{0.04}N$-film, as given in Figure 6.27. The as-deposited state exhibits a single-phase cubic solid solution, which is in agreement with the XRD-measurements on powdered coatings, Figure 6.3. The fcc-TiN-(111) reflex appears already at 500 °C, while the fcc-$Ti_{0.5}Al_{0.5}N$ solid solution reflexes decrease, indicating decomposition of the fcc-TiAlN with increased temperatures. Moreover, additional reflexes were observed in the range between 45-60 degree and for

temperatures from 500 °C up to 1100 °C, which can be regarded as artefacts. At 1100 °C, strong hcp-AlN-(002) and -(004)-reflexes can be detected. Recrystallization and grain growth can be observed from the increasing reflex intensities with increasing annealing time. The fcc-TiN-(111) reflex almost disappears, while the formation of the interfacial grains through the above mentioned substrate-coating reaction sets on at 1100 °C. The intensities for the TiAl(O,N)-phase at the interface are much stronger than for the $Ti_{0.41}Al_{0.55}Nb_{0.02}N$-film.
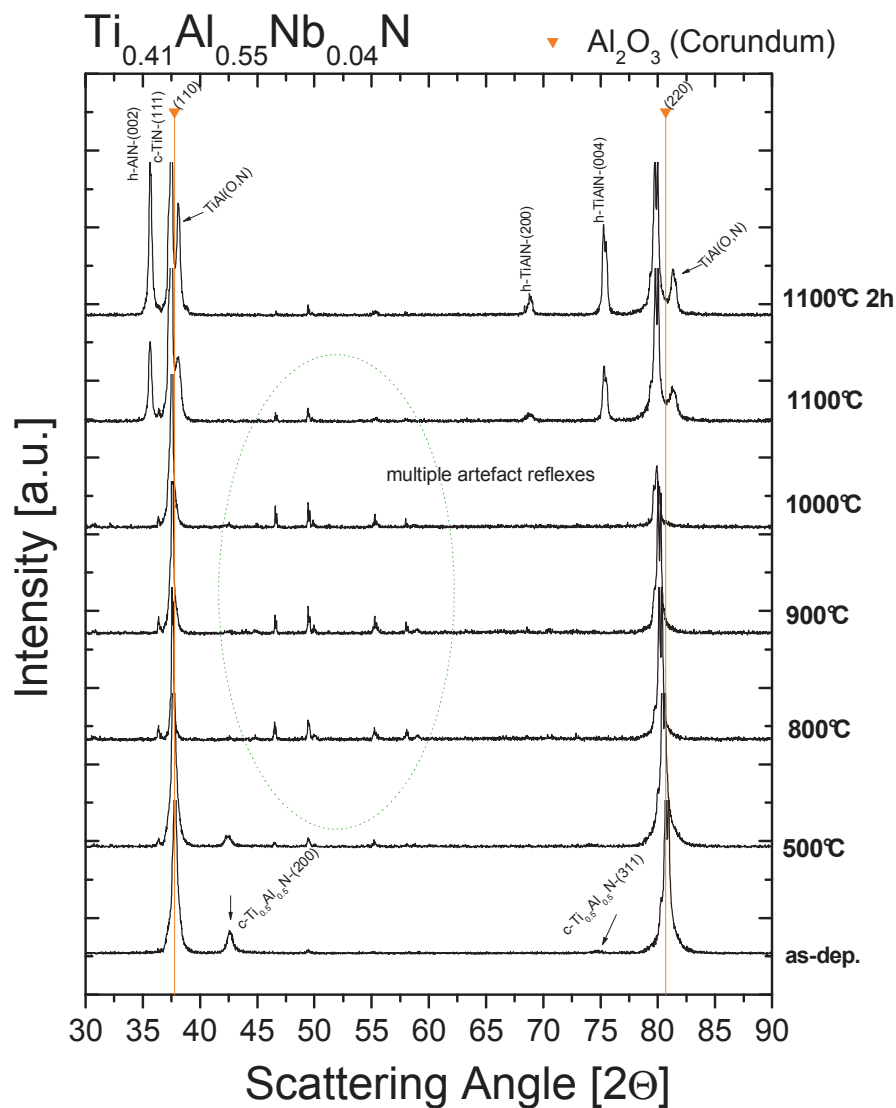
Figure 6.27: In-situ HT-XRD patterns of the $Ti_{0.41}Al_{0.55}Nb_{0.04}N$-thin film.

✓ **Ti$_{0.35}$Al$_{0.57}$Nb$_{0.08}$N:**

The XRD pattern of the Ti$_{0.35}$Al$_{0.57}$Nb$_{0.08}$N-coating, as-deposited on sapphire (Figure 6.28) corresponds to the XRD pattern taken from the powder, as presented in Figure 6.3. The single phase solid solution fcc-(Ti$_{1-x}$Al$_x$)$_{1-z}$Nb$_z$N structure is stable up to ~900 °C. At 1000 °C the fcc-Ti$_{0.5}$Al$_{0.5}$N-(200)-reflex has vanished, whereas hcp-AlN-reflexes evolve. Althoug the fcc-TiN-(111) and -(222) reflexes appear at 1000 °C, the hcp-AlN-reflexes are dominating. Furthermore, the strong intensities of the reflexes at ~38.4 and ~82.0 degree, refer to the interfacial grains as explained for the (Ti$_{1-x}$Al$_x$)$_{1-z}$Y$_z$N-films, see chapter 6.5.1.
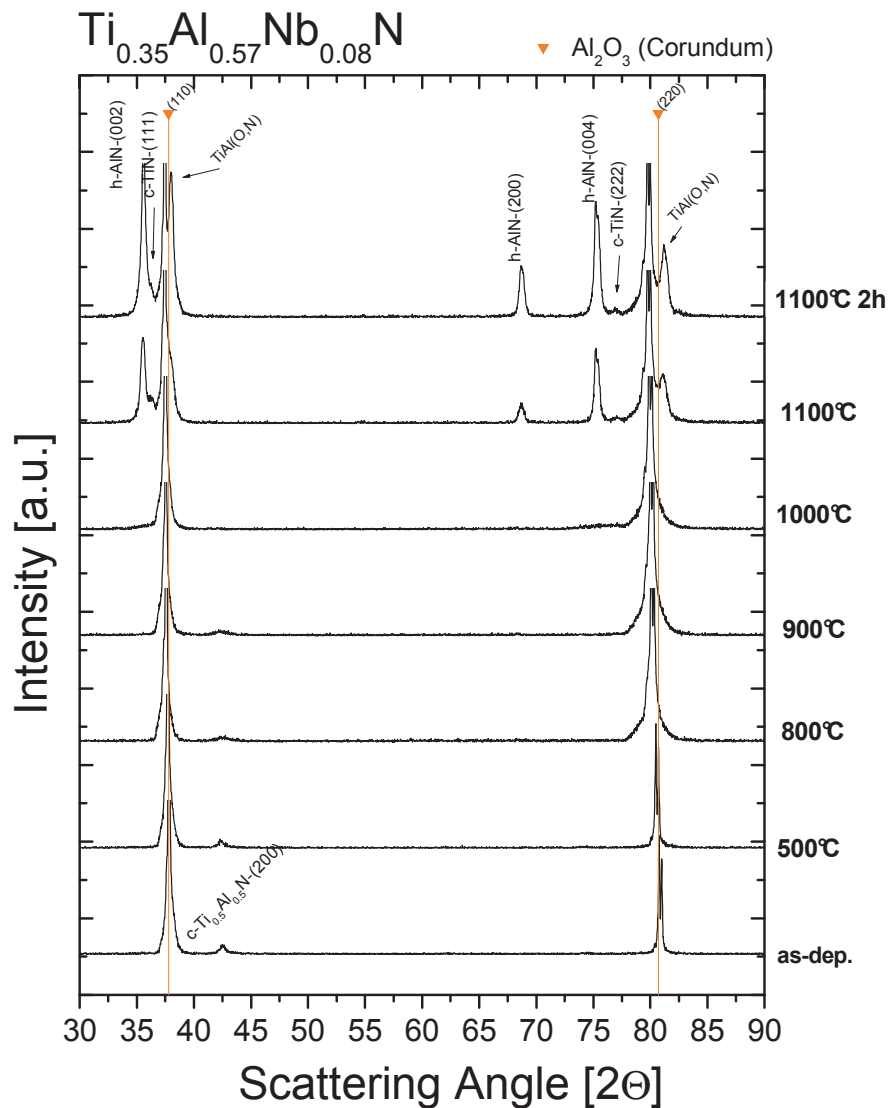
Figure 6.28: In-situ HT-XRD patterns of the Ti$_{0.35}$Al$_{0.57}$Nb$_{0.08}$N-thin film.

Even for the $Ti_{0.35}Al_{0.57}Nb_{0.08}N$-coating, no precipitated Nb-nitrides were found. However, the cross-sectional HR-TEM image of the interface, given in Figure 6.29(a), exhibits a recrystallized structure in the film and grains reaching into the substrate. Further, much more misfit dislocations were observed at the interface of the $Ti_{0.35}Al_{0.57}Nb_{0.08}N$-thin film, presented in Figure 6.29(c), than for the $Ti_{0.44}Al_{0.54}Nb_{0.02}N$-thin film. The SAED-pattern in Figure 6.29(b), taken from the area of Figure 6.29(c), indicates the different lattice constants of the substrate and the hexagonal coating in this area with the respective double dots.
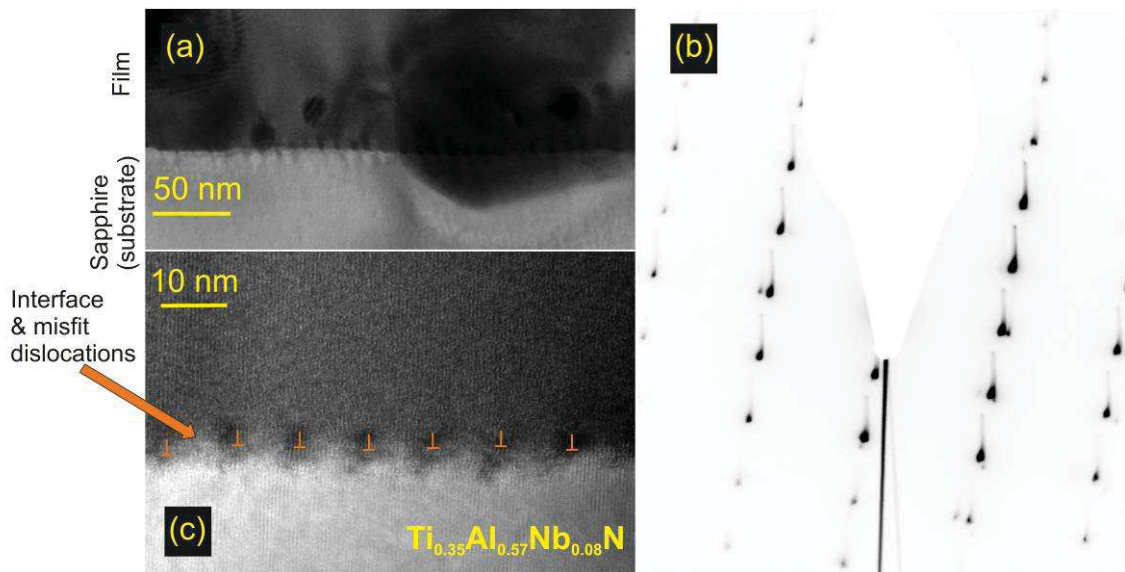
Figure 6.29: (a) Cross-sectional HR-TEM images of the $Ti_{0.35}Al_{0.57}Nb_{0.08}N$-thin film-substrate interface, and (c) a higher magnification detail, after the HT-XRD-annealing procedure to 1100 °C. (b) SAED-pattern corresponding to the magnified interface region (c).

The XRD-patterns after the in-situ HT-XRD measurements to 1100 °C are given in Figure 6.30. Shifted peak positions, as compared to the thermodynamically stable constituents, indicate that the decomposition process of the solid-solution was not completed in this annealing stage. All cubic and hexagonal peaks are shifted towards lower angles, which proposes that the Nb-atoms are incorporated in fcc-TiN, as well as in hcp-AlN at 1100 °C. Further, with increasing Nb-amount, the discussed interface reaction at ~1100 °C results in increasing intensities marked within the dotted ellipse.
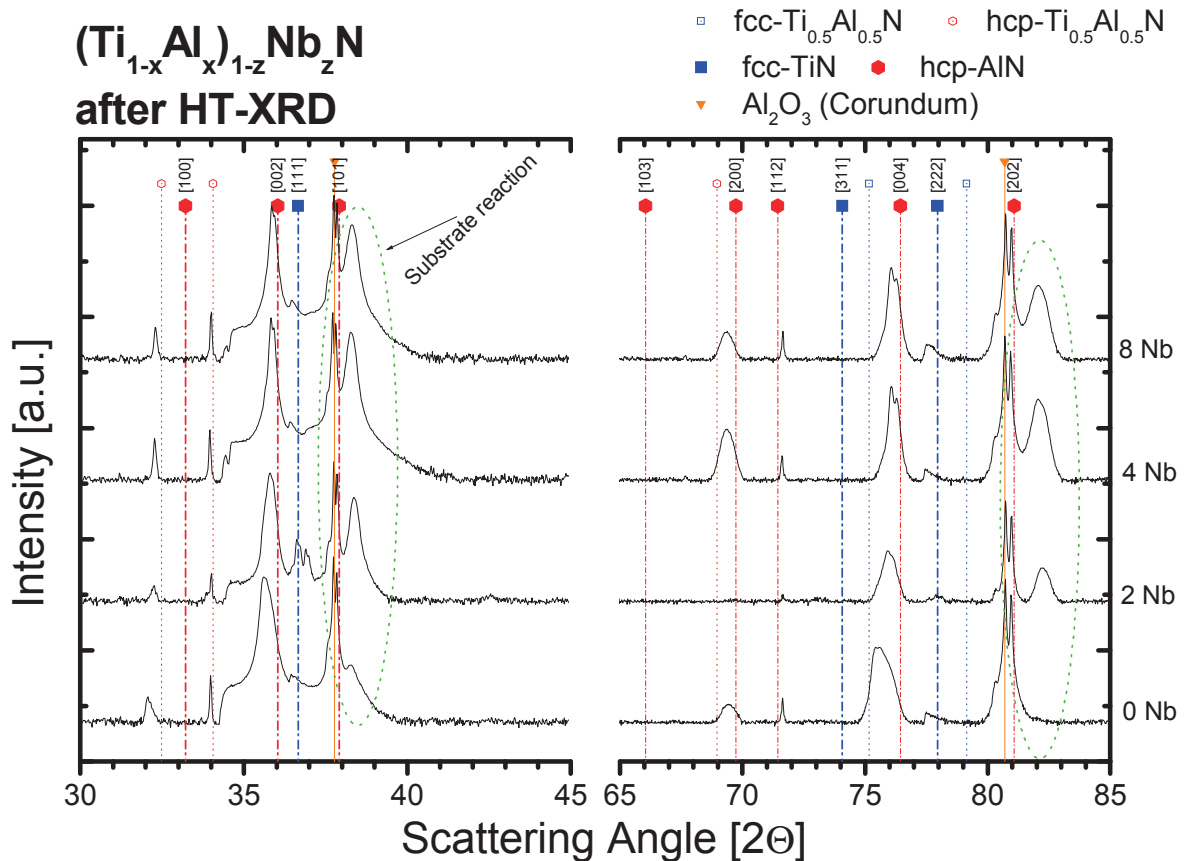
Figure 6.30: XRD-patterns of the $(Ti_{1-x}Al_x)_{1-z}Nb_zN$-films after in-situ HT-XRD measurements.

In addition to the XRD analysis, STA-investigations were performed, given in Figure 6.31(b). The DSC-curve proposes the onset of recovery processes of all investigated coatings at ~500 °C, which corresponds to the findings of the Y-containing films. The introduction of Nb-atoms into single-phase fcc-$Ti_{1-x}Al_xN$ results in higher stresses and more defects which are reversed by more intense recovery. In accordance to the in-situ HT-XRD measurements, overlapping peaks of recovery and the formation energies of fcc-AlN and fcc-TiN through spinodal decomposition, result in the broad exothermic feature between 500 °C and 900 °C. The onset temperature for recrystallization and grain growth is retarded by niobium-addition, when compared to the $Ti_{1-x}Al_xN$-baseline, as the second exotherm feature is shifted to above 1100 °C. This peak is generally described in literature to origin from recrystallization and grain growth processes [84]. The DSC-plot in Figure 6.31(b), confirms that neither the baseline $Ti_{1-x}Al_xN$ nor the Nb-alloyed coatings are completely restructured at 1100 °C, the maximum temperature of the HT-XRD investigations. However the long annealing times in the HT-XRD, as

compared to the dynamic STA-measurements, explain the recrystallized structure found in HR-TEM analyses at the interface, as shown in Figure 6.26(a) and Figure 6.29(a). Mass loss at temperatures higher than 1200 °C is observed for all coatings and is related to the evaporation of overstoichiometric nitrogen, as explained in chapter 6.5.1. In comparison to the $(Ti_{1-x}Al_x)_{1-z}Y_zN$-coatings, a higher weight loss occurs for the $(Ti_{1-x}Al_x)_{1-z}Nb_zN$-films, Figure 6.31(a).
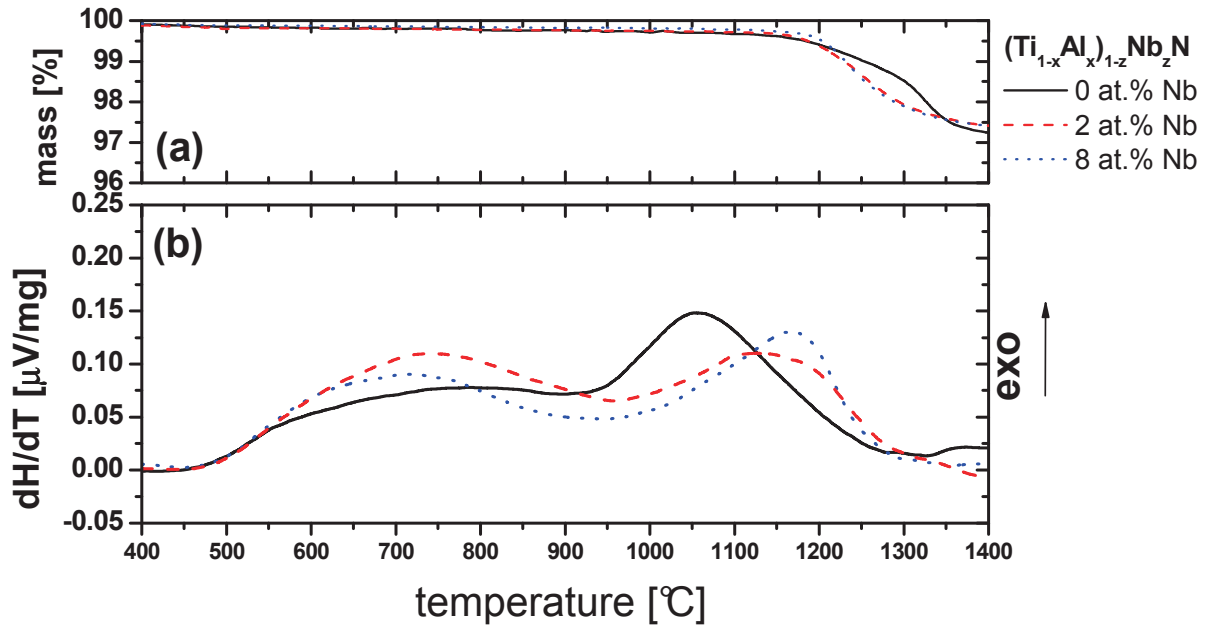
Figure 6.31: (a) TGA- and (b) DSC-curves of the $(Ti_{1-x}Al_x)_{1-z}Nb_zN$-thin films, during annealing to 1400 °C.

The XRD-measurements on powder samples after the STA exhibit complete decomposition of the former fcc-$(Ti_{1-x}Al_x)_{1-z}Nb_zN$ into fcc-TiN and hcp-AlN, as presented in Figure 6.32. The mentioned peak shift for the fcc-$Ti_{0.5}Al_{0.5}N$ peaks in as-deposited state cannot be observed for the powder samples after two times annealing to 1400 °C. Only the fcc-TiN-peaks were shifted to slightly lower angles, which can be explained through Nb-incorporation into the cubic phase rather than into the hexagonal phase. Thus, the hcp-AlN-phase remains visibly unaffected by the increasing Nb-content. In comparison to the $(Ti_{1-x}Al_x)_{1-z}Y_zN$ -films, no precipitated Nb-nitrides were found, however with increasing Nb-amount, a shoulder emerges on the left side of the fcc-TiN-(200)-reflex. Although, the position of the fcc-NbN-(200)-reflex is ~2 degree lower than the observed peak, it can be assumed, that the apparent shoulder in the

$Ti_{0.35}Al_{0.57}Nb_{0.08}N$-film corresponds to a solid-solution cubic-Nb(Ti)N, indicated as a green triangle in Figure 6.32, consisting of ~45% fcc-NbN and 55% fcc-TiN.

Furthermore, we can observe that the annealing up to 1100 °C, during the in-situ XRD measurements, resembles an intermediate state in decomposition, recrystallization and growth. The thermally stable phases are only reached after the STA to 1400 °C, as presented in Figure 6.32.
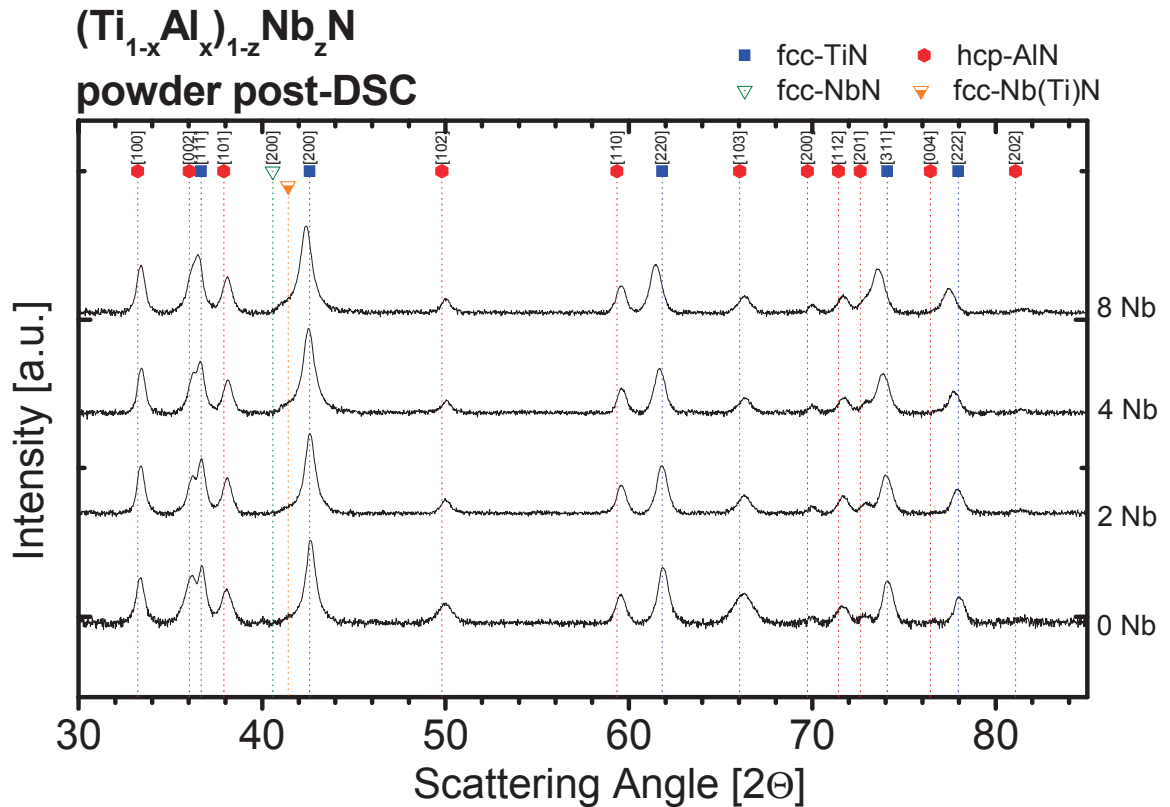
Figure 6.32: XRD-patterns of $(Ti_{1-x}Al_x)_{1-z}Nb_zN$-powder samples, with 0 at.%, 2 at.%, 4 at.% and 8 at.% Nb in the metal sublattice, after STA to 1400 °C.

7 Summary & conclusion

This thesis reports on the influence of yttrium or niobium on the microstructure, mechanical properties and thermal stability of the already industrially successful $Ti_{1-x}Al_xN$-coatings. Consequently, powder metallurgically prepared targets (Plansee AG), of $(Ti_{0.5}Al_{0.5})_{1-z}Y_z$ and $(Ti_{0.5}Al_{0.5})_{1-z}Nb_z$ with z = 0, 0.02, 0.04 and 0.08, were used for the reactive deposition of $(Ti_{1-x}Al_x)_{1-z}Y_zN$- and $(Ti_{1-x}Al_x)_{1-z}Nb_zN$-thin films, employing a plasma-assisted PVD-process.

The prepared $(Ti_{1-x}Al_x)_{1-z}Y_zN$-thin films contain 0, 3, 5 and 9 at.% yttrium and the $(Ti_{1-x}Al_x)_{1-z}Nb_zN$-films contain 2, 4 and 8 at.% niobium in the metal sublattice, respectively. By means of X-ray-diffraction (XRD), transmission electron microscopy (TEM) and nanoindentation the individual influence of Y and Nb was investigated in the as-deposited state of the thin films. In-situ high temperature X-ray-diffraction (HT-XRD) up to 1100 °C and simultaneous thermal analysis (STA) up to 1400 °C were performed to investigate the thermal stability. Additionally, TEM-analysis combined with XRD-measurements after the in-situ HT-XRD-annealing were conducted for detailed structural investigations.

It is presented, that yttrium addition shifts the solubility limit of the cubic $Ti_{1-x}Al_xN$ for AlN to lower mole fractions. Already the addition of 3 at.% Y to the metal sublattice results in a mixed cubic-hexagonal structure of the $(Ti_{1-x}Al_x)_{1-z}Y_zN$-thin films. The thin film prepared from the $(Ti_{0.5}Al_{0.5})_{0.92}Y_{0.08}$ target crystallizes almost completely in the hexagonal structure. Contrary to that, the Nb-addition to $Ti_{1-x}Al_xN$ leads to no changes of the single-phase cubic structure up to the highest Nb-content investigated, of 8 at.% in the metal sublattice, respectively.

Further, the columnar structure of the cubic $Ti_{1-x}Al_xN$-coating is maintained by the Nb-containing films, whereas the yttrium induced grain-refinement, through continuous re-nucleation, results in nanocrystalline coatings. For the $(Ti_{1-x}Al_x)_{1-z}Y_zN$-films, the decreasing hardness, from 33 GPa to 23 GPa for the 0 and 9 at.% Y in the metal sublattice, respectively, refers to the increasing hexagonal phase amount, which prevails the hardening effect through grain-refinement and solid-solution. In contrast, the $(Ti_{1-x}Al_x)_{1-z}Nb_zN$-films exhibit increasing hardness, from 33 GPa to 40 GPa, for z = 0 and 8 at.% Nb in the metal sublattice, respectively, due to solid-solution hardening.

Annealing experiments on both $(Ti_{1-x}Al_x)_{1-z}M_zN$-systems exhibit an up to 130 °C higher onset-temperature for recrystallization and grain growth as compared to the ~950 °C for $Ti_{0.42}Al_{0.58}N$. Thus, an enhanced thermal stability was found in vacuum during in-situ HT-XRD and inert atmosphere during STA, respectively. Combined results from in-situ HT-XRD-measurements and TEM-investigations show that the decomposition of $Ti_{1-x}Al_xN$, resulting in a dual-phase structure consisting of fcc-TiN and hcp-AlN, is retarded by both alloying elements. While the $(Ti_{1-x}Al_x)_{1-z}Nb_zN$-coatings decompose to hcp-AlN and fcc-TiN, incorporated Nb is in a cubic solid-solution Ti(Nb)N, the $(Ti_{1-x}Al_x)_{1-z}Y_zN$-films decompose to fcc-TiN and hcp-AlN, as well as fcc-YN, the latter can clearly be detected by XRD for the coatings containing 5 and 9 at.% Y in the metal sublattice. Further it was shown, that a strong interfacial reaction between the Al_2O_3-substrate and the coating material occurs for all films during long-time annealing for ~20 hours during the in-situ HT-XRD.

Based on microstructural investigations of the as-deposited and annealed structures, employing state-of-the-art investigation methods, it can be concluded that the addition of Y and Nb yield excellent results with respect to high-temperature applications.

8 References

[1] Peters M. Leyens C., Titanium and Titanium alloys, Wiley-VCH Verlag, Weinheim, 2003.

[2] H. Holleck, Surface and Coatings Technology 36/1-2 (1988) 151.

[3] H. Nickel, et al., Mikrochimica Acta 119/1-2 (1995) 23.

[4] C. Mitterer, Leoben, 2007.

[5] Mattox D.M. Bunshah R.F., Deposition Technologies for Films and Coatings,, 1982.

[6] K. Röll Kienel G., Vakuumbeschichtung 2 , Verfahren und Anlagen, VDI-Verlag, Düsseldorf, 1995.

[7] Wierzchon T., Burakowski T., Surface Engineering of Metals, CRC Press LLC, 1999.

[8] Rossnagel S.M., Bunshah R.F., G.E. McGuire (ed.), Handbook of Hard Coatings, Deposition Technologies, Properties and Applications, Noyes Publications, New Jersey, 2001.

[9] R.A. Häfer, Oberflächen- und Dünnschicht- Technologie, Teil I: Beschichtungen von Oberflächen, Springer-Verlag, Berlin, Heidelberg, 1987.

[10] H. Frey, Vakuumbeschichtung 1, VDI-Verlag GmbH, Düsseldorf, 1995.

[11] G. Franz, Oberflächentechnologie mit Niederdruckplasmen, Beschichten und Strukturieren in der Mikrotechnik, Springer-Verlag, Berlin, Heidelberg, 1994.

[12] M. Ohring, Materials Science of Thin Films, Elsevier, Singapore, 2006.

[13] Lichtenberg A.J., Lieberman M.A., Principles of Plasma Discharges and Materials Processing, John Wiley & Sons Inc., New York, 1994.

[14] D.L. Smith, Thin-Film Deposition: Principles and Practice, McGraw-Hill Publishing Co., 1995.

[15] A. Grill, Cold Plasma in Materials Fabrication, IEEE Press, New Jersey, 1994.

[16] F. Adibi, et al., Journal of Applied Physics 73/12 (1993) 8580.

[17] I. Petrov, et al., Journal of Vacuum Science and Technology A: Vacuum, Surfaces and Films 21/5 (2003).

[18] P. H. Mayrhofer, PhD Thesis, Institute of Physical Metallurgy and Materials Testing, University of Leoben, Leoben, 2001.

[19]   M. Moser, PhD Thesis, Department of Physical Metallurgy and Materials Testing, University of Leoben, Leoben, 2008.

[20]   J. Greene, Handbook of Crystal Growth, Elsevier Science Publishers, 1993.

[21]   B. A. Movchan, A. V. Demchish, Physics of Metals and Metallography 28/4 (1969) 83.

[22]   J. A. Thornton, Annu. Rev. Mater. Sci. 7 (1977) 239.

[23]   R. Messier, et al., J. Vac. Sci. Technol. A-Vac. Surf. Films 2/2 (1984) 500.

[24]   P. B. Barna, M. Adamik, in: Yves Pauleau, P. B. Barna (Eds.), NATO Advanced Research workshop on Protective Coatings and Thin Films: Synthesis, Characterization and Applications, Kluwer Academic Publishers, Alvor, Portugal, 1996.

[25]   W.D. Münz, J. Vac. Sci. Technol. A 4(6) (1986) 2717.

[26]   L. Chaleix-Combadiere, J. Machet, Vide: Science, Technique et Applications, 1996, p. 116.

[27]   H. Hasegawa, et al., Surface and Coatings Technology 132/1 (2000) 76.

[28]   H. A. Jehn, et al., J.Vac.Sci.Tech.A. 4/6 , Nov.-Dec. 1986 (1986) 2701.

[29]   Y. Miura, S. Fujieda, Journal of Applied Physics 81/9 (1997) 6476.

[30]   S. PalDey, S. C. Deevi, Materials Science and Engineering A 342/1-2 (2003) 58.

[31]   O. Knotek, et al., J.Vac.Sci.Tech.A. 4/6 , Nov.-Dec. 1986 (1986) 2695.

[32]   J. Musil, H. Hruby, Thin Solid Films 365/1 (2000) 104.

[33]   A. Kimura, et al., Surface and Coatings Technology 120-121 (1999) 438.

[34]   M. Zhou, et al., Thin Solid Films 339/1-2 (1999) 203.

[35]   R. Cremer, et al., Fresenius' Journal of Analytical Chemistry 361/6-7 (1998) 642.

[36]   H. Willmann, PhD Thesis, Institute of Physical Metallurgy and Materials Testing, University of Leoben, Leoben, 2007.

[37]   G. Gottstein, Physikalische Grundlagen der Materialkunde, Springer Verlag, Berlin, 2007.

[38]   P. H. Mayrhofer, et al., Applied Physics Letters 83/10 (2003) 2049.

[39]   H. W. Hugosson, et al., Journal of Applied Physics 93/8 (2003) 4505.

[40]   P. H. Mayrhofer, et al., Applied Physics Letters 88/7 (2006).

[41]   R. F. Zhang, S. Veprek, Materials Science and Engineering A 448/1-2 (2007) 111.

[42] A. Hörling, et al., Journal of Vacuum Science and Technology A: Vacuum, Surfaces and Films 20/5 (2002) 1815.

[43] A. D. Korotaev, et al., Surface and Coatings Technology 185/1 (2004) 38.

[44] W. Reimers, et al., Application of Neutrons and Synchrotron Radiation in Engineering Materials Science, Wiley-VCH, 2007.

[45] C. Kittel, Introduction to Solid State Physics, John Wiley & Sons, Inc., 2005.

[46] P. Haasen, Physical Metallurgy, Cambridge University Press, Cambridge, 1996.

[47] Easterling K. E., Porter A.D., Phase Transformations in Metals and Alloys, Van Nostrand Reinhold (UK), 1981.

[48] H. Clemens, lecture notes of 'Metallkunde I' -, Leoben, 2006.

[49] A.G. Guy Metallkunde für Ingenieure, Akademische Verlagsgesellschaft, Wiesbaden, 1983.

[50] W. Schatt, H. Worch, Werkstoffwissenschaft, Wiley-VCH Verlag GmbH, 2003.

[51] L. Hultman, Vacuum 57/1 (2000) 1.

[52] User Manual A400 VL, Leybold AG.

[53] Operational Manual ACG-6B, ENI Company Ltd.

[54] User Guide Leybold Vacuum, Leybold AG.

[55] User Guide Tylan General R 7030/7031, Tylan General GmbH.

[56] User Manual Duo 20, Pfeiffer Vacuum GmbH, 2002.

[57] P. H. Mayrhofer, et al., Thin Solid Films 415/1-2 (2002) 151.

[58] William Henry Bragg, William Lawrence Bragg, Proceedings of the Royal Society of London. Series A, Containing Papers of a Mathematical and Physical Character 88/605 (1913) 428.

[59] W.F. Hemminger, H.K. Cammenga, Methoden der Thermischen Analyse, Springer-Verlag, Berlin, Heidelberg, 1989.

[60] Netzsch, 2000.

[61] C. Michaelsen, et al., J. Phys. D-Appl. Phys. 30/23 (1997) 3167.

[62] J.M. Howe, Transmission Electron Microscopy and Diffractometry of Materials, Springer Verlag, Berlin, Heidelberg, 2001.

[63] M. Lechthaler, Diploma Thesis, Department of Physical Metallurgy and Materials Testing, Leoben, 2005.

[64] P. O. Å. Persson, lecture notes of the course 'Transmission Electron Microscopy', Linköping, Sweden, 2006.

[65]   David B. Williams, C. Barry Carter, Transmission Electron Microscopy (1 Basics), Springer Science+Business Media Inc., New York, 1996.

[66]   David B. Williams, C. Barry Carter, Transmission Electron Microscopy (2 Diffraction), Springer Science+Business Media Inc., New York, 1996.

[67]   David B. Williams, C. Barry Carter, Transmission Electron Microscopy (3 Imaging), Springer Science+Business Media Inc., New York, 1996.

[68]   David B. Williams, C. Barry Carter, Transmission Electron Microscopy (4 Spectrometry), Springer Science+Business Media Inc., New York, 1996.

[69]   T. Chudoba, in: Albano Cavaleiro, Jeff Th. M. De Hosson (Eds.), Nanostructured Coatings, Springer Science+Business Media, LLC, New York, 2006.

[70]   A. C. Fischer-Cripps, Nanoindentation, Springer Science+Business Media LLC, New York, 2004.

[71]   A. C. Fischer-Cripps, et al., Surf. Coat. Technol. 200/18-19 (2006) 5645.

[72]   W. C. Oliver, G. M. Pharr, J. Mater. Res. 7/6 (1992) 1564.

[73]   IBIS, Fischer-Cripps Laboratory.

[74]   Instrumentierte Eindringprüfung zur Bestimmung der Härte und anderer Werkstoffparameter - Teil 1: Prüfverfahren, DIN EN ISO 14577-1, 2003.

[75]   Instrumentierte Eindringprüfung zur Bestimmung der Härte und anderer Werkstoffparameter - Teil 2: Prüfung und Kalibrierung der Prüfmaschine, DIN EN ISO 14577-2, 2003.

[76]   Instrumentierte Eindringprüfung zur Bestimmung der Härte und anderer Werkstoffparameter - Teil 3: Kalibrierung von Referenzproben, DIN EN ISO 14577-3, 2003.

[77]   K. Kutschej, et al., Surf. Coat. Technol. 200/7 (2005) 2358.

[78]   M. Moser, P. H. Mayrhofer, Scripta Materialia 57/4 (2007) 357.

[79]   J. Y. Rauch, et al., Surface and Coatings Technology 157/2-3 (2002) 138.

[80]   C.N.J. Wagner, Local Atomic Arrangments Studied by X-ray Diffraction, Gordon and Breach, New York, 1966.

[81]   W. S. Choi, et al., Journal of Vacuum Science and Technology A: Vacuum, Surfaces and Films 18/6 (2000) 2914.

[82]   D. B. Lewis, et al., Surface and Coatings Technology 114/2-3 (1999) 187.

[83]   P. H. Mayrhofer, et al., Journal of Applied Physics 100/9 (2006).

[84]   P. H. Mayrhofer, et al., Progress in Materials Science 51/8 (2006) 1032.